The Thesis Committee for Fernando Saint-Martin de Abreu Soares
Certifies that this is the approved version of the following thesis:

A Pore Scale Study of Ferrofluid-Driven Mobilization of Oil

APPROVED BY
SUPERVISING COMMITTEE:

Supervisor: _____
Maša Prodanović

Co-Supervisor _____
Chun Huh

A Pore Scale Study of Ferrofluid-Driven Mobilization of Oil

by

Fernando Saint-Martin de Abreu Soares, B.S.

Thesis

Presented to the Faculty of the Graduate School of

The University of Texas at Austin

in Partial Fulfillment

of the Requirements

for the Degree of

Master of Science in Engineering

The University of Texas at Austin

August 2015

Dedication

In memory of my father, Fernando Jose, whose presence in spirit still inspires me to seek knowledge.

Acknowledgements

This work certainly would not be possible without the help from others. I was indeed very fortunate to have received many fundamental contributions by different people. In this limited space, I hope to acknowledge at least some of these contributions.

First, I was lucky for having advisors who supported me in ways beyond their advising duties. I thank Dr. Maša Prodanović for her inspiring leadership and genuine concern about the students' well-being. I thank Dr. Chun Huh for his admirable knowledge and kindness, aside from his patience with my excessive experimentalism with numerical methods.

I express my gratitude to the companies that sponsored my project as part of the Nanoparticles for Subsurface Engineering consortium for their financial support and for the feedback of their representatives who attended our industrial affiliates meetings. My acknowledgement also to Dr. Steven L. Bryant, who helped me preparing my presentations for the sponsors and made valuable comments on my research.

I would like acknowledge the contributions of Dr. Ali Qajar, who helped me interpreting simulation results and provided useful comments on the content of the thesis. I am also very grateful for the head start on ferrohydrodynamics given by Dr. Amir Rahmani in the early stages of my research.

Writing this thesis was made easier by the staff of the Petroleum and Geosystems Engineering Department, who are responsible for cultivating an amazingly productive work environment. In special, I thank Frankie Hart, Leilani Swafford, Sophia Ortiz and Jin Lee for being always so prompt in sorting out administrative issues.

Shashvat Doorwar and Christopher Hapchuk, who conducted the ferrofluid experiments in trapping micromodel geometries, contributed with insightful experimental data that guided the development of my physical model.

The members of the research group to which I belonged, for their companionship and constructive criticism of my work, were also very important. I feel truly honored for being part of a group with such talented students. A special thanks to Rahul Verna and Soheil Ghanbarzadeh, for sharing their experiences with the level set method, Weiwei Wang, for helping me with the thesis formatting and Rodolfo Victor, for being helpful in so many different ways.

I thank all the friends who did not contribute to my thesis directly, but made my time in Austin very enjoyable. I also thank the friend in Brazil, whose strong friendship survived the time and distance, for the warm welcome whenever I was able to visit home.

Last, but certainly not least, I thank my mother for the unconditional love and care. My greatest blessing is counting with her life-long support.

Abstract

A Pore Scale Study of Ferrofluid-Driven Mobilization of Oil

Fernando Saint-Martin de Abreu Soares, M.S.E.

The University of Texas at Austin, 2015

Supervisor: Maša Prodanović

Co-Supervisor: Chun Huh

Ferrofluids are stable dispersions of magnetic nanoparticles in a liquid carrier. The easily controllable magnetization of ferrofluids has motivated their use in a broad range of applications, from the non-intrusive imaging of organic tissues to the sealing and stability improvement of bearings. More recently, experiments verified the feasibility of injecting nanoparticles with specifically-designed coatings into permeable rocks without significant retentions or permeability loss. The possibility of controlling fluid displacements in a porous medium by manipulating magnetic stresses with an applied magnetic field suggests ferrofluids have a potential for subsurface applications, particularly in the field of enhanced oil recovery.

Although extensive research has been devoted to the mechanics of ferrofluids, this topic is never analyzed under the conditions that are likely to occur in the subsurface environments. In particular, research on the behavior of two-phase systems in which the ferrofluid is wetting is still lacking.

This work has the goal of simulating immiscible displacements influenced by the magnetic stresses acting on a wetting ferrofluid at pore scale. The simulations are based on a model for the quasi-static displacement of the liquid interface that couples the effects of the fluid flow with the magnetic stresses.

An approach for the numerical simulation is developed based on a level set method for tracking the interface displacement, which is suitable for the complex shapes appearing in the pore space. The explicit-jump immersed interface method, which handles irregular domains with non-conforming grids, is employed in specific versions for the fluid flow and the magnetic field.

The results indicate that the magnetic stress distribution is strongly affected by the configuration of the magnetic field in the regions of proximity between liquid interface and the solid surface. By applying a field parallel to the flow path, the magnetic stresses push the non-wetting phase away from the solid surfaces resulting in an interface configuration that reduces the flow viscous stresses and thus favors applications related to the transport of non-wetting liquids. A field perpendicular to the flow path generates magnetic stresses that contribute to the mobilization of ganglia trapped in snap-off geometries, suggesting ferrofluids can be used to reduce residual oil saturations in reservoirs in synergy with other methods.

Table of Contents

List of Figures

CHAPTER 1: Introduction

1.1 FERROFLUIDS OVERVIEW

Ferrofluids are dispersions of ferri- or ferromagnetic nanoparticles which are employed in a variety of engineering applications. The particles in a ferrofluid must fulfill certain stability requirements: resist settling and remain in Brownian motion even under the influence of strong magnetic fields. Stability is commonly achieved by creating single-domain particles smaller than 20 nm and coating them with a molecular layer of polymer or surfactant, which is designed to prevent agglomeration with other particles due to Van der Waals forces.

In the absence of a magnetic field, the dispersed nanoparticles present random orientations. When an external field is applied, the field direction becomes a preferential direction of alignment for the magnetic moments associated to each of the particles. As the field increases, the magnetization of the liquid carrier due to the particles net alignment becomes stronger. Once the field is removed, the particles revert to random orientations and the fluid bulk magnetization disappears, characterizing a magnetic behavior analogous to paramagnetism. Ferrofluids are distinct, however, for displaying much stronger magnetizations than natural paramagnetic materials. Despite their outstanding magnetization, ferrofluids preserve the mechanical behavior of liquids. Hence, they can flow under the influence of magnetic stresses and be controlled by an applied magnetic field.

Early research on ferrofluids took advantage of these magnetic stresses for mechanical applications, such as the lubrication and sealing of bearings. Employing ferrofluids as lubricant seems to reduce friction fluctuations and noise generation in bearings functioning under high rotation-speeds as well as preventing leakages through a self-sealing mechanism (Ochonski and Lawrence 2005). The magnetic stresses also enable the controlled levitation of non-magnetic bodies immersed in ferrofluids, which can be used as the operating principle for actuators in microelectromechanical system (MEMS) devices (Torrez-Diaz and Rinaldi 2014).

The ferrofluid magnetization response is also useful for the biomedical field, especially in applications related to detection and imaging. For instance, magnetic nanoparticles designed to attach to specific body tissues are used as contrast agents for enhancing magnetic resonance imaging (MRI), (Oh et al. 2006), or as tracers in magnetic particle imaging (MPI), (Pankhurst et al 2009). Aside from imaging, ferrofluids contribute to biomedicine by providing a mean for hyperthermia treatments: the oscillation of the nanoparticles' magnetic moments under an alternating field produces localized heat for burning off cancer cell without affecting surrounding tissue (Pollert and Zaveta 2012).

Promising applications of ferrofluids in subsurface environments were first identified by (Moridis et al. 1998). Following this work, using Hele-Shaw cell and sand pack experiments, (Borglin et al. 1998) verified the possibility of controlling the ferrofluid flow in porous media with a magnet. More recently, research effort focused on characterizing transport properties of nanoparticles in real sedimentary rocks. The work

of (Rodriguez et al. 2009) verified that the propagation of surface-treated silica (non-magnetic) nanoparticles through micron-sized pores occurs mostly without blocking or plugging the pore throats. In an experiment with the injection of magnetic nanoparticles with a coating designed to reduce adsorption to rocks surfaces, (Yu et al. 2010) obtained very little retention of particles and insignificant permeability reduction in reservoir cores, even for particles concentrations as high as 10% by weight.

The evidence indicating the feasibility of ferrofluid transport to target locations in reservoirs prompted research interest in petroleum engineering. In the field of enhanced oil recovery (EOR), (Davidson et al. 2012) explored a process of ferrofluid heating analogous to the one used for hyperthermia treatments in biomedicine as a method of thermal recovery for heavy oil. The petroleum industry can also benefit from magnetic nanoparticles in non-reservoir applications, such as the removal of dispersed oil from produced water by a process of magnetic separation (Ko et al. 2014). (Ryoo et al. 2012) investigated the possibility of determining oil saturations non-invasively with the acoustic response, under an oscillating field, produced by nanoparticles dispersed in the wetting phase. The numerical results obtained by (Rahmani et al. 2012) with the simulation of ferrofluid blobs trapped in pore geometries with special attention to the nonlinear magnetic field effects are particularly relevant to the research presented here. However, the vast majority of the literature on ferrofluid/fluid interactions in either MEMS devices or porous media, including (Rahmani et al. 2012), deal with the ferrofluid as a non-wetting phase.

1.2 SIMULATION OF FERROFLUIDS AT MICRO-SCALE

The numerical study of the porous media flow of a ferrofluid phase at a macro-scale was pioneered by (Oldenburg et al. 2000), in which a modified Darcy formulation incorporated the magnetic body force and the magnetic field was assumed to be undisturbed by the ferrofluid presence. Whereas this formulation is suitable for a spatially-averaged continuum modeling of porous media flows, it is insufficient for analyzing phenomena that take place at smaller size-scales.

Simulating ferrofluid dynamics at a micro-scale poses both theoretical and numerical challenges. Aside from capillary and thermodynamic pressures, the shape of the interface between the magnetic and the non-magnetic fluids is influenced by the spatial distribution of magnetic stresses. The magnitude of these stresses is a function of the local strength and orientation of the magnetic field which in turn is affected by the interface shape and orientation. In a broader sense, obtaining the equilibrium configuration of a ferrofluid/fluid interface involves solving a hydrodynamic problem coupled with an electromagnetic one. In the particular case of a wetting ferrofluid phase inside a permeable rock, the irregular pore geometry presents an additional difficulty.

Quite a bit of the research done in simulating a ferrofluid interface under the combined influence of capillary, viscous and magnetic stresses has dealt with non-wetting ferrofluids in unconstrained domains. In (Lavrova et al. 2006), a hybrid BEM-FEM approach was employed to obtain the equilibrium shape of a ferrofluid droplet under various magnetization strengths. (Zhu et al. 2011) used a level set method for

obtaining the equilibrium shape of a magnetized ferrofluid droplet on a flat surface. As far as constrained domains are concerned, the behavior of ferrofluid droplets exposed to a magnetic field in microfluidic devices is a well-studied problem; microfluidic systems can generate, handle and manipulate many individual droplets which elongate when exposed to a uniform magnetic field. Since the pioneer study by (Tarapov 1974), a great number of theoretical (Rosensweig 1997; Lavrova et al. 2004), experimental (Berkovsky et al. 1987) and numerical (Afkhami et al. 2008) studies have been performed. Mathematical formulation for ferrofluid droplets is based on the coupled Maxwell's and Young-Laplace equations (Rosensweig 1997).

In contrast with the previous works, (Rahmani et al. 2012) considered a ferrofluid droplet inside the pore space of a permeable rock and thus subjected to much stronger capillary pressures. The numerical approach was, however, limited for not being able to take into account spatial variations of the magnetic field and the presence of viscous stresses. Moreover, by taking the ferrofluid as the non-wetting fluid, the pore surface does not interact with the magnetic field and serves only as an obstacle for the interface displacement, which results in a simpler problem.

However, no peer-reviewed studies have been reported that simulates the pore-scale behavior of a non-wetting fluid surrounded by *wetting ferrofluid* phase in a magnetic field, neither in a simple (microfluidic) geometry nor in more complicated pore structures resembling those in a natural porous materials.

1.3 RESEARCH GOALS

The work here presented aims to develop a numerical method for simulating quasi-static immiscible displacements involving a wetting ferrofluid confined by a converging-diverging geometry resembling those in porous media. This kind of situation is of particular relevance to subsurface engineering.

Most of the multiphase ferrofluid research and applications focus on the manipulation, detection and actuation of ferrofluid droplets by magnetic fields. However, the non-wetting phase in subsurface structures typically consists of pre-existing fluids which we are trying to reach, such as soil contaminants or residual oil. Therefore, ferrofluids are more adequate for the role of chasing fluid, i.e. the injected wetting phase.

Once the numerical method is available, it can be used for the quasi-static simulations of oil ganglia surrounded by magnetized ferrofluids in geometries mimicking the pores of reservoir rocks. These simulations combined with appropriate models for residual oil mobilization provide a framework for evaluating the potential of developing a new EOR technique based on injecting magnetic nanoparticles into the reservoir and imposing a magnetic field from the wellbore. Although the EOR application is the most obvious, the same numerical approach can be adapted to other relevant situations, for instance, the steady-state motion of a non-magnetic droplet inside a ferrofluid-filled microchannel. The potentially practical applications can then be investigated.

Dealing with the problems described above requires accounting for the effects of irregular solid surfaces to the viscous and magnetic stresses distribution within the

ferrofluid. The numerical method employed is adapted from the level set method for quasi-static fluid-fluid displacement developed by (Prodanović and Bryant 2006), which is capable of handling the complex geometries of the pore space in a simple and reliable manner. The method capabilities go beyond (Rahmani et al. 2012) and (Ryoo et al. 2012), in which a similar level-set-based approach treated the magnetic field in a simplistic manner and the effects of viscous stresses were ignored.

The magnetic field distribution is solved by an explicit-jump immersed interface method (EJIMM) (Wiegmann and Bube 2000) so that the sharp field variations in the vicinity of the interfaces between the ferrofluid and the non-magnetic media are accurately calculated. An extension of the EJIMM introduced by (Tan et al. 2009) is used for obtaining the pressure and velocity fields of the incompressible Stokes flow in an irregular flow domain. Thus far we have implemented the method in two dimensions.

CHAPTER 2: Immiscible Displacements in Porous Media

Among the features that distinguish this work from others on the subject of ferrohydrodynamics, is its focus on the influence of the flow geometry. The capacity of predicting how the ferrofluid flow is affected by the enclosing geometry is extremely relevant to the study of ferrofluids in the highly-irregular flow paths formed within porous media. Nonetheless, a framework for investigating the effects of magnetization-induced stresses to ferrofluids in porous media must be consistent with the traditional approaches to modeling porous media flow. These approaches, which are concerned mostly with the interplay between viscous and capillary forces, are the theme of this chapter.

Although some of the concepts presented here apply to porous media flow in general, most of the discussion that follows is based on a specific kind of process: the two-phase immiscible displacement. The emphasis on this process is justified by its enormous importance to Reservoir Engineering. In particular, the dynamics of immiscible displacements is responsible for the formation of residual oil after primary and secondary recoveries. Trapping and releasing of residual oil will be discussed in detail as part of the chapter.

2.1 INTERFACIAL EFFECTS

In the context of immiscible displacements, the boundary between two phases is represented as an interface of infinitesimal thickness. The effects caused by the free energy associated to this kind of interface tend to be significant when dealing with problems in the micro-scale. Hence, these effects are pertinent to the study of multiphase flows in porous media.

A certain amount of work is necessary for altering the surface area of a material. This work reflects a change in the surface free energy. More generally, any variation in the surface geometry is associated with a change in surface free energy that must be compensated by the work done by the net pressure acting on the surface. This intuitive reasoning is translated mathematically into the Young-Laplace equation:

$$\Delta P = \sigma(\kappa_1 + \kappa_2) \tag{2.1}$$

where σ is the interfacial tension (surface free energy per unit of area) and the terms κ_1 and κ_2 correspond to the two principal curvature components of the surface. For a liquid interface free of external forces, the pressure difference is uniform and the principal curvatures are equal, which is consistent with the notion that unperturbed droplets tend to have a spherical shape to minimize the surface free energy.

Wettability is another important property of micro-scale immiscible systems that is quantified in terms of variations of surface free energy. It refers to the interaction between a liquid interface and an adjacent solid surface. As shown by the schematic in

Fig. 2.1, the contact between the two fluids and the solid surface generates interfacial tensions σ_{s1} and σ_{s2} associated to fluids 1 and 2, respectively.

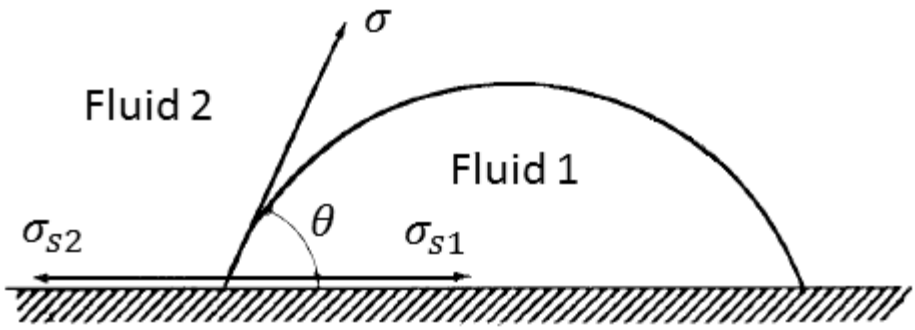

Figure 2.1 – Schematic of the balance formed by the interfacial tension between the fluids and between each of the fluids and the solid surface. The fluid interface must intercept the solid surface at a contact angle $\boldsymbol{\theta}$ to satisfy the balance.

There is also an interfacial tension σ associated to the interface between the fluids. When equilibrium is achieved, the interface intercepts the solid surface at an angle θ called contact angle, which is determined according to a force balance at the three-phase contact line:

$$\sigma_{s2} = \sigma_{s1} + \sigma \cos\theta \tag{2.2}$$

Provided that the interfacial tensions are known, the balance above, called Young-Dupre equation, can be solved for θ.

The value of θ defines different wettability behaviors. This can be exemplified

by considering the case of an oil reservoir in which fluid 1 is oil, fluid 2 is water and the solid surface corresponds to the surface of the rock matrix. For $\theta < 65^o$, the reservoir is said to be oil-wet; for $105^o < \theta < 180^o$, it is water-wet. The remaining interval $65^o < \theta < 105^o$ defines the condition of intermediate-wettability. In the limiting case of $\theta = 180^o$, the oleic phase is said to be perfectly non-wetting.

It is worth noticing that actual reservoirs commonly present chemical heterogeneities. Consequently, wettability may vary from pore to pore, defining a condition known as mixed-wettability.

2.2 PORE-SCALE MODELS

Before embracing the complexity of interconnected pores of various sizes and shapes that characterize the morphology of the porous media, the physics of an isolated pore is considered. Pore-scale models are rarely based on realistic pore geometries, such as the geometries formed by the cemented sediments in permeable rocks. Alternatively, the models usually take advantage of simple geometries that are able to capture the physics of the problem. For instance, the toroidal pore space in Figure 2.2 can be used to demonstrate the main features of immiscible displacements at a pore-scale level.

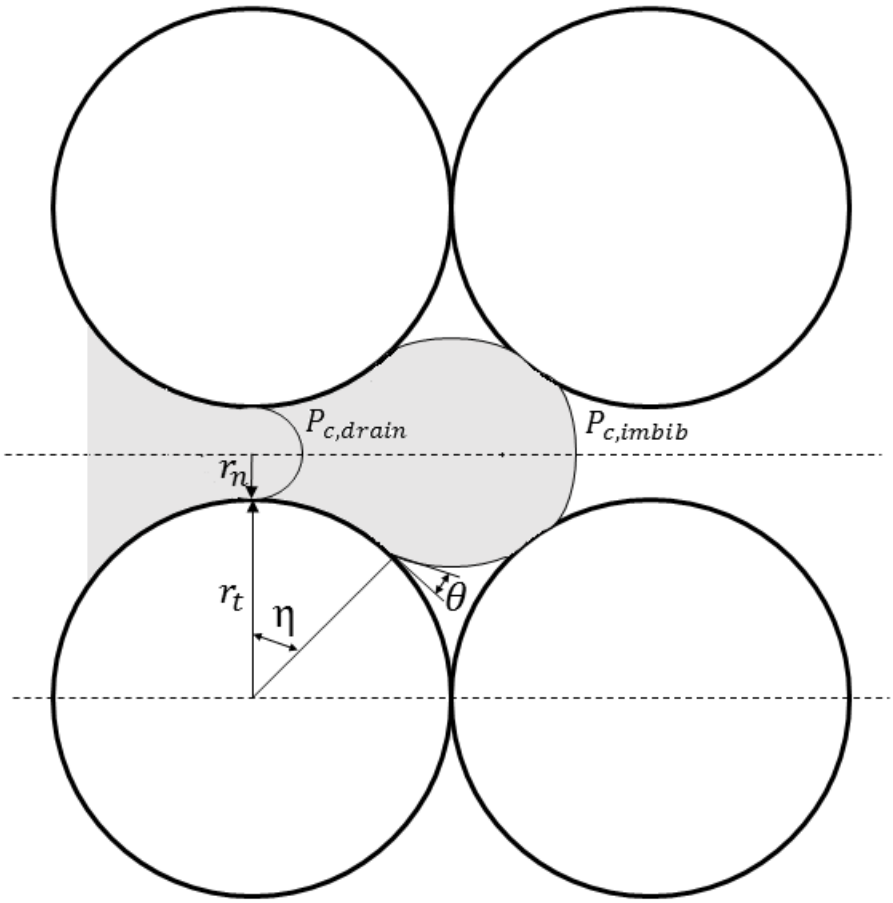

Figure 2.2 – Schematic of an immiscible displacement taking place in a toroidal geometry. The two capillary pressures highlighted $\boldsymbol{P_{c,drain}}$ and $\boldsymbol{P_{c,imbib}}$ are associated to the critical drainage and imbibition interface configurations, respectively.

The flow path formed by the two tori has a circular cross-section with varying radii. In pore-scale models, the region with the minimum cross-section area is referred to

as the pore neck (or pore throat), whereas the relatively large voids connected by the pore necks are called pore bodies.

Upon the displacement of two immiscible phases inside the pore, it is assumed that the motion of the liquid interface is sufficiently slow such that the effects of viscous stresses can be neglected and the pressure on each phase can be taken as uniform. Under this assumption, the displacement is completely controlled by the pressure difference between the phases, defined as the capillary pressure:

$$P_c = P_{nw} - P_w \tag{2.3}$$

According to this definition, the capillary pressure is a positive quantity, as the pressure is greater in the non-wetting phase than in the wetting. Some authors prefer defining the capillary pressure in terms of phase densities rather than wettabilities. This alternative definition is useful for handling cases with mixed-wettability, but it can be confusing for leading to negative values. Given the common assumption that reservoirs are water-wet and that most oils are less dense than water, the two definitions are rendered as equivalent.

As discussed in the previous subsection, the pressure difference across an interface is given by Eq. (2.1). It is usual to represent the capillary pressure through Eq. (2.1) by incorporating some function of the pore geometry and the wettability:

$$P_c = \frac{2\sigma}{r_n} F(\theta) \tag{2.4}$$

In particular, for the toroidal geometry considered:

$$F_{torous}(\theta) = \frac{\cos(\theta - \eta)}{1 + (r_t/r_n)(1 - \cos\eta)} \tag{2.5}$$

The geometric parameters appearing in Eqs. (2.4) and (2.5) are defined graphically in Figure 2.2. It should be noted that the angle θ to which the equations refer is not necessarily the contact angle of Eq. (2.2) obtained under equilibrium for a smooth surface. If the liquid interface is moving, the static contact angle should be replaced with a dynamic contact angle that depends on the direction of the motion. The advancing contact angle θ_A formed when the three-phase contact line moves towards the wetting phase is generally greater than the static angle, whereas the receding contact angle θ_R formed by motion in the opposite direction tends to be smaller.

Dynamic contact angles is a difficult subject because of the several factors that affect them. Viscous stresses can act on the contact line creating a velocity-dependent angles (Stokes et al 1990). Moreover, surface roughness, which is very prominent in natural porous media, affects the motion of the contact line in a way that can be interpreted as forming a wide range of apparent dynamic angles (Morrow 1976).

Whenever an applied pressure pushes the non-wetting phase against the wetting, the displacement is called drainage. Alternatively, decreasing the applied pressure so that the non-wetting phase retreats is called imbibition. In the absence of an applied pressure, the capillary pressure pushes the wetting phase against the non-wetting causing what is called as spontaneous imbibition.

Both the drainage and imbibition processes are not continuous and stable, but rather occur in abrupt discrete steps called rheons (also known as Haines jumps). For drainage, once the applied pressure is sufficient to overcome the critical capillary

pressure $P_{c,drain}$ at the pore neck, the interface will expand rapidly while being counteracted by capillary pressures below $P_{c,drain}$ until it reaches some narrower pore neck. Analogously, imbibition becomes unstable when the applied pressure is decreased below a threshold $P_{c,imbib}$ with stability being only regained when the interface arrives at larger pore body.

In general, instability occurs when the interface motion leads to decreasing interface curvatures for drainage, or to increasing curvatures for imbibition. This intuitive argument can be sustained by thermodynamics (Melrose and Brander 1974) and is expressed mathematically by the stability condition:

$$\frac{d\kappa}{dV_{nw}} > 0 \tag{2.6}$$

where $\kappa = \kappa_1 + \kappa_2$ and V_{nw} is the volume of the non-wetting phase inside the pore space.

The critical interface configurations associated to the critical pressures $P_{c,drain}$ and $P_{c,imbib}$ are represented in Figure 2.2 for the toroidal pore space. Assuming the contact angle is zero, a simple calculation shows

$$P_{c,drain} = \frac{2\sigma}{r_n} \tag{2.7}$$

$$P_{c,imbib} = \frac{2\sigma}{r_n} \frac{1}{\sqrt{2\left(\frac{r_t}{r_n}\right)^2 + 2\frac{r_t}{r_n} + 1} - \frac{r_t}{r_n}} \tag{2.8}$$

2.2.1 Trapping Mechanisms

Pore-scale models are particularly useful to the study of trapping in porous media. While trapped phases in most cases of interest might occupy up to 20 pore bodies (Payatakes 1982), the underlying mechanisms that cause trapping also exist at smaller size-scales and can be demonstrated through simple pore geometries.

On the aftermath of either drainage or imbibition, the displaced phase is typically not completely ejected out of the porous medium. The fraction of pore volume that remains filled by the displaced phase after the displacing process takes place is referred to as the residual saturation.

In a permeable rock subjected to drainage, the residual wetting phase retreats as to form pendular rings around the grain contacts and in crevices, as shown by the rock cross-section in Figure 2.3. If the pressure applied to the rock sample is increased, the wetting rings will further retreat being compressed by the flowing non-wetting phase. The residual saturation could be reduced to a theoretical zero for an infinite applied pressure as the wetting film would shrink to a nearly monolayer coverage (Lake 1988).

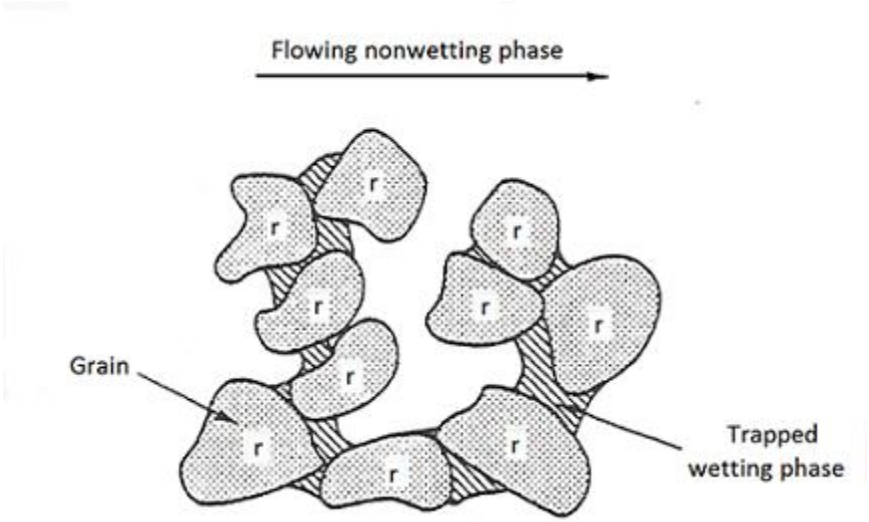

Figure 2.3 – Schematic of rock cross-section showing the residual wetting phase occupying crevices and the gaps between grain contacts (Lake 1988).

However, the focus of this text is the residual non-wetting phase resulting from imbibition, which has greater relevance to Reservoir Engineering. Unlike the ring structures displayed by the wetting phase, the residual non-wetting phase exists in the form of trapped ganglia that are found predominantly in the larger pores, where the ratio between volume and surface area is higher. The trapping of ganglia can be explained in terms of local heterogeneities of porous media. There are two pore-scale models for this purpose, each of which represents a different kind of heterogeneity: the pore doublet model and the snap-off model.

A schematic of the pore doublet model is visualized in Figure 2.4(a). The model consists of two parallel channels with different diameters that converge at both ends. The

channels are both long enough so that well-developed Poiseuille flow can be assumed and the influence of the interface presence to the flow can neglected. The heterogeneity associated with the difference in diameters translates as a competition between capillary force and viscous force; the first being stronger in the smaller channel and the latter in the larger one.

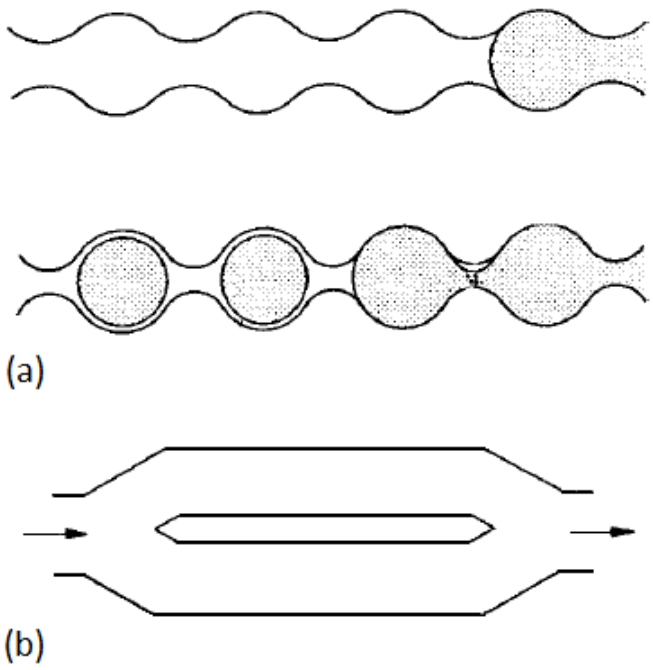

Figure 2.4 – Pore-scale models for representing trapping mechanisms: (a) shows a variable cross-section geometry, in which trapping occurs by snap-off; (b) shows a geometry with two flowing paths of unequal diameter, in which trapping occurs by bypassing (Sahimi 2011).

The relative importance between these two forces can be represented by a dimensionless quantity known as capillary number Ca, which appears often in the study of trapping and mobilization of ganglia. Its exact definition varies according to the context, but always meaning capillary force over viscous force. An adequate definition for the current problem is given by

$$Ca_{doublet} = \frac{\eta U L_d}{\sigma R_s} \tag{2.9}$$

where η is the viscosity, U is the average flow velocity of both channels, L_d is the channel length and R_s is the smaller channel radius.

Some calculations (Lake 1988) show that the flow in the pore doublets can be entirely determined by the capillary number and the ratio between the channels' diameters. The limiting cases obtained with $Ca = 0$ and $Ca \gg 1$ present very little resemblance to actual porous media flow. Nevertheless, the model is useful for a range of small capillary numbers. In these cases of dominant capillary force, the liquid interface in the smaller channel reaches the end more quickly and thus bypassing the larger channel. This result accurately represents how the mechanism of bypassing contributes to trapping of non-wetting phase. It also prompts two observations: bypassing tends to trap non-wetting phase in the larger pores and increasing Ca can reduce the volume of non-wetting phase bypassed.

The snap-off model is characterized by a single flow path with variable cross-section, such as the sinusoidal pore geometry of Figure 2.4(b). Its heterogeneity reflects the variations of width between the pore neck and the pore body in the pores of

permeable rocks. As imbibition takes place in this kind of geometry, the wetting phase entering the pore forms a film on the pore surface and surrounds the non-wetting phase. Trapping by snap-off occurs when the wetting phase, instead of displacing the non-wetting to the downstream pore, causes its rupture at the pore neck. Experiments by (Roof 1970) demonstrate that the rupture is expected to happen whenever the capillary pressure at the upstream front of the non-wetting phase is exceeded by the capillary pressure at the neck. Snap-off is therefore common in pores with large neck-to-body aspect ratios.

In practice, the trapping of ganglia in natural porous media commonly involves a combination of both bypassing and snap-off mechanisms. A thorough study on the different trapped phase configurations and their associated trapping geometries was conducted by (Chatzis et at 1983). The study shows that both variable flow cross-sections and alternate flow paths contribute to the formation of ganglia in large pores surrounded by small ones. Their experiments also verified that the snap-off mechanism can act alone leading to isolated blobs filling single pore bodies. In Berea sandstone, this kind of configuration accounts for about 80% of all the residual volume, suggesting the existence of many pores with large aspect ratios.

2.2.2 Mobilization of Residual Oil

The most significant application of the trapping pore-scale models presented in the previous subsection is the study of residual oil ganglia in water-wet reservoirs. The enormous research effort devoted to residual oil and to the techniques for its mobilization is easily justifiable; offshore production data in the U.S. show that in the early 1970's, before Enhanced Oil Recovery (EOR) practices become widespread, only about 25% of the original oil in place was recovered (Geffen 1973).

Once production starts in a reservoir, three phases of recovery might be implemented (Lake 1988). Primary recovery refers to oil being displaced solely by the drive mechanisms that naturally exist in the reservoir, which obviously leads to relatively small productions. Secondary recovery involves the injection of gas or water to offset pressure depletion due to the primary recovery. Lastly, tertiary recovery comprehends all different techniques used after the potential for secondary recovery is exhausted. Whenever some material not normally present in the reservoir is injected as part of one of these recovery phases (typically the tertiary), the process is called EOR.

In spite of the differences highlighted by the classification scheme above, the methods designed to mobilize additional oil generally fall into two categories in regards of the effect they aim to achieve (Stegemeier 1977). The first category is comprised of methods for altering the balance between viscous and capillary forces, such as surfactant flooding for reducing the liquid interfacial tension. In the other category are methods that change fluid phase volume through interphase mass transfer, such as in the case of

alcohol flooding. This text will focus on the first category because of its pertinence to the context of ferrofluid applications.

As previously discussed, the size of the trapped ganglia tends to be smaller for larger capillary numbers. It is therefore natural to assume that some critical applied pressure can lead to reduced residual saturations. The dynamics of a ganglion being mobilized is nevertheless not trivial. There are two distinct displacement patterns that a ganglion may display once viscous stresses overcome the capillary force preventing its motion: quasi-static and dynamic (Payatakes 1982).

Dynamic mobilization occurs when the applied pressure yields Ca far greater than the critical mobilization value Ca_c. It is characterized by multiple interfaces of the ganglion advancing simultaneously in different fronts, frequently causing fissions that generate other ganglia. Alternatively, when Ca exceeds Ca_c by a small amount, the ganglion creeps along the flow direction and advances on interface at a time, which defines the quasi-static mobilization. For being a limiting case of successful mobilization, the quasi-static pattern deserves attention. Once again, a pore-scale analysis is useful for underlining the physics of the process.

The sequence in Figure 2.5 illustrates different stages of the quasi-static mobilization of a ganglion occupying several pores. In the case of complete absence of pressure gradients in the wetting phase, the pressure in both phases should be uniform at this size-scale and all the ganglion's interfaces have the same uniform curvature as shown

in Figure 2.5(a). When some pressure is applied causing the wetting phase to flow around the ganglion, the interfaces downstream increase their curvatures by advancing into the pore necks while the ones upstream reduce their curvatures by retreating towards the pore bodies. The reshaping of the interfaces is accompanied by contact angles switching from their static values to their dynamic limiting values at zero velocity. This results in the new ganglion configuration of Figure 2.5(b). Finally, when the applied pressure becomes sufficiently large so that $Ca > Ca_c$, a drainage rheon causes one of the downstream interfaces to advance abruptly while an imbibition rheon takes place upstream. The displaced ganglion is shown in Figure 2.5(c).

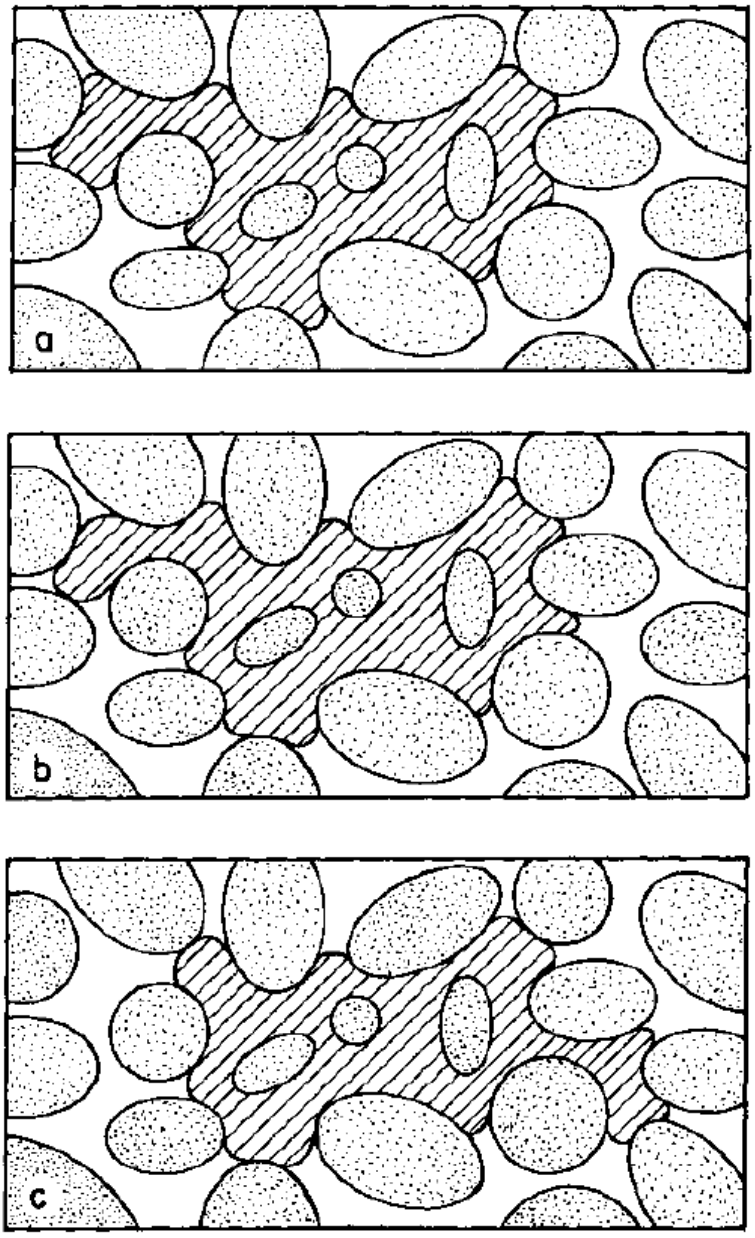

Figure 2.5 – Schematic with the different stages of the quasi-static mobilization of a ganglion: (a) in the absence of flow, (b) with some applied pressure below critical and (c) after mobilization occurs (Payatakes 1982).

Being a relatively orderly process, it is possible to identify the exact critical conditions for quasi-static mobilization in a given trapping geometry. The approach suggested by (Ng and Paytakes 1980) starts with evaluating the critical drainage curvatures for the downstream interfaces and the critical imbibition curvatures for the upstream ones. These critical interface configurations depend solely on the wettability and geometry of the porous medium. A sensitivity analysis is then conducted by comparing all possible pairs formed by an upstream and a downstream interface. Naturally, the pair that requires the lowest pressure gradient to reach its critical curvatures determines the critical conditions for mobilization.

2.3 MACROSCOPIC MODELS

So far this chapter has only described immiscible displacements taking place in an isolated pore or in some few pores located within a small distance from each other. Dealing with pore-scale models is advantageous because it allows applying the conservation laws and their associated equations directly. However, this kind of approach is not feasible for studying the flows in macroscopic volumes of porous media. Although the conservation laws remain the same, it would require excessive computational effort to solve boundary value problems delimited by intricate liquid and solid interfaces for a large number of pores. Moreover, the actual morphology of the pore spaces is rarely known.

Therefore, upscaling results obtained with pore-scale models to the macro-scale is not straightforward. In fact, macroscopic modeling of porous media involves some particular approaches, which can be classified as discrete or continuum (Sahimi 2011).

Continuum models are based on the concept of effective porous media properties, defined as the spatial averages of primary pore-scale properties. Strictly speaking, this definition applies for some continuous domain in which each point corresponds to a representative elementary volume (REV), i.e. the volume below which local fluctuations of some primary property become large (Bear 1972). Employing the continuum approach therefore demands the existence of REVs sufficiently small compared to the length scales of the problem.

Once effective properties are established, some macro-scale correlation is needed for relating these properties with measurable flow parameters. The empirically determined Darcy's law provides this correlation:

$$\vec{V}_{darcy} = \frac{K}{\eta_e}(\nabla P - \rho_e \vec{g}) \tag{2.10}$$

where $\vec{V}_{darcy}$ is the Darcy's velocity , η_e is the effective viscosity, ρ_e is the effective density and K is the permeability of an isotropic porous medium. The permeability, typically measured in darcy units ($d = 0.9869\ \mu m^2$), determines how easily a fluid flows through the porous medium under a given pressure gradient. The quantity between parenthesis is commonly as a potential gradient $\nabla\phi$.

The Darcy's law as written in Eq. (2.10) implies the existence of a single fluid. In the case of multiphase flows, the same expression can be applied to each of the phases

present in the porous medium by setting the fluid parameters to be the effective properties of the phase and replacing the absolute permeability K with the phase permeability. While K is an intrinsic property of a porous medium, the phase permeability refers to the behavior of a specific phase in the presence of other phases. For a phase α, the phase permeability K_α can be calculated as

$$K_\alpha = k_{r\alpha} K \tag{2.11}$$

where the dimensionless parameter $k_{r\alpha}$ is the relative permeability of phase α. Obtaining this parameter is crucial for reservoir simulations and is also usually difficult because of its dependence on several factors such as saturation, saturation histories of the fluids, wettability behavior, pore space morphology and capillary number (Sahimi 2011). In most cases, $k_{r\alpha}$ becomes zero for some non-zero saturation of phase α, which can be explained by percolation theory.

However, the continuum approach has little relevance to this work as it fails to predict trapping and releasing of residual oil without resorting to some pre-existing experimental data. The discrete approach provides an alternative way of modeling porous media that has become increasingly popular in the past decades (Sahimi 2011). It consists of treating the voids in the solid matrix of a porous medium as part of interpenetrating networks. The phenomena taking place in the voids are analyzed at pore-scale and then their effects are extended to large volumes by networks that interconnect the voids in a way that reflects the physics that govern these phenomena.

For studying problems related to residual oil in reservoirs, the networks must somehow emulate the heterogeneities associated to the snap-off and bypassing

mechanisms presented in Section 2.2.1. It means that the network must account for the topological distinctions between pore bodies and pore necks and for the possibility of pores connected to multiple flow paths. In the network model originally proposed by (Fatt 1956) for studying percolation problems, the nodes play the role of pore bodies while the bonds intersecting the nodes are the necks. The number of neighboring nodes to which each node is connected defines its coordination number. This simple yet far-reaching model provides means of upscaling the results discussed previously for single pores.

2.3.1 Capillary Curves

The immiscible displacement patterns at a macro-scale differ significantly from the ones obtained for a single pore scenario although being governed by the same physics. For a sufficiently large number of pores, the changes in phase saturation do not resemble intermittent rheons but rather a smooth function of the effective capillary pressure.

This kind of pattern is observed in the data obtained through mercury porosimetry experiments, in which mercury is injected into an evacuated rock sample at an arbitrary pressure and is then withdrawn from the sample by lowering the pressure to ambient. The procedure forms drainage and imbibition loops with mercury being the non-wetting phase. An example of these loops for a Berea Sandstone sample is given by Figure 2.6.

In the example, the capillary curves, each of which assigned to a number, form the loops (1-2), (3-4) and (5-6) ordered by increasing maximum capillary pressure.

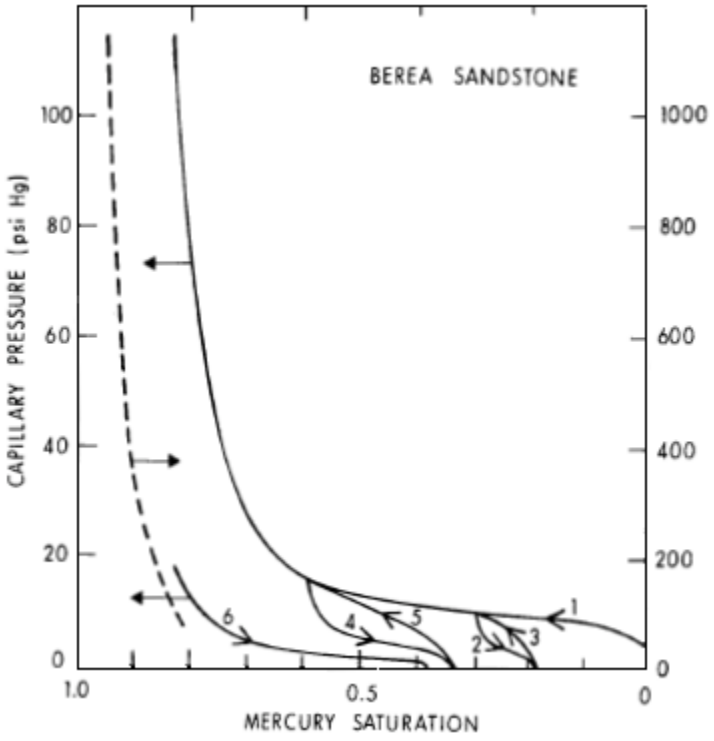

Figure 2.6 – Mercury porosimetry curves obtained for a Berea Sandstone sample with three complete drainage/imbibition loops (Stegemeier 1977).

Capillary curves present some interesting features that are better explained if the porous medium is seen as a pore network. Once the pressure applied exceeds the capillary pressure necessary for invading the largest pore necks of the sample (entry pressure), non-wetting saturation S_{nw} starts growing gradually. The greater is the

applied pressure, the smaller are the pore neck sizes that cannot be accessed by the non-wetting phase and fewer are the pore bodies not occupied by the non-wetting phase. This procedure produces smooth and continuous capillary curves that are reproducible for different sample volumes. From a pore network perspective, these curves are an evidence that the rock sample contains many parallel networks with different entry pressures and good accessibility within each network, which seems to be the case for typical sandstones (Stegemeier 1977).

It can be inferred from the discussion above that the pore neck size distribution controls the shape of the capillary drainage curve. When comparing curves obtained from different samples, there might cases in which the pore neck sizes are distributed around the average in a similar fashion although the pore neck size distribution itself is different for each rock. It suggests that different capillary curves can be derived from the same function with some proper normalization. By dividing the capillary curve $P_c(S_{nw})$ by the capillary pressure associated to a representative pore neck size according to a tube-flow permeability model:

$$j_{Le}(S_{nw}) = \frac{P_c(S_{nw})\sqrt{\frac{K}{\emptyset}}}{\sigma F(\theta)} \tag{2.12}$$

where the dimensionless parameter on the left-hand side is called Leverett number and $\emptyset$ is the porosity. The factor $F(\theta)$ is the same as the one appearing in Eq. (2.4) and it is usually taken as simply $F = \cos\theta$, which holds for a straight tube geometry. Substituting Eq. (2.4) into (2.12) yields an expression for the neck size being invaded at a given saturation:

$$r_n(S_{nw}) = \frac{2\sqrt{K/\emptyset}}{j_{Le}(S_{nw})} \tag{2.13}$$

Imbibition is slightly different because its displacement process is controlled by the size of the pore bodies instead of the pore necks. The wetting phase starts invading pores with small bodies and reach increasingly large ones as the applied pressure is decreased. Although the pore network reasoning described for drainage is still applicable, the resulting capillary curves are different, as shown in Figure 2.6. Part of the hysteresis is due to the trapping of ganglia, which is also responsible for the non-zero non-wetting saturations reached once imbibition is over. This should be distinguished from contact-angle hysteresis caused by the difference between advancing and receding contact angles and that further contributes to differentiating drainage and imbibition curves.

Another important observation drawn from capillary curves is that the residual non-wetting phase saturation depends on the maximum non-wetting phase saturation attained during the drainage/imbibition loop. The mercury porosimetry data can thus be used to construct an initial-residual (IR) curve, such as the ones shown in Figure 2.7 for different natural porous media. The IR curve is fundamental for the estimating the capillary desaturation curve presented in the subsequent section.

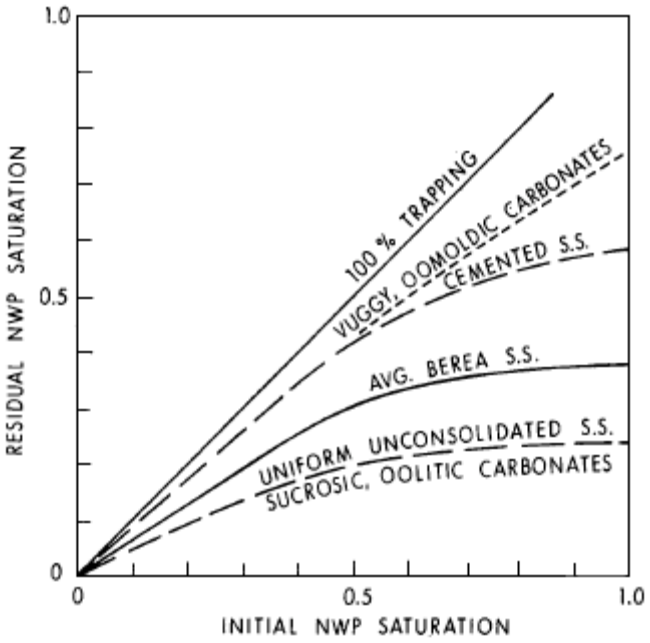

Figure 2.7 – Initial-Residual curves for different kinds of natural porous media (Stegemeier 1977).

2.3.2 Capillary Desaturation Curve Estimation

At a macroscopic level, the mobilization of a trapped phase is seen as a decrease in residual saturation for an increase of capillary pressure, which is graphically described by the Capillary Desaturation Curve (CDC). Figure 2.8 contains the schematic of typical CDCs for both wetting and non-wetting residual phases.

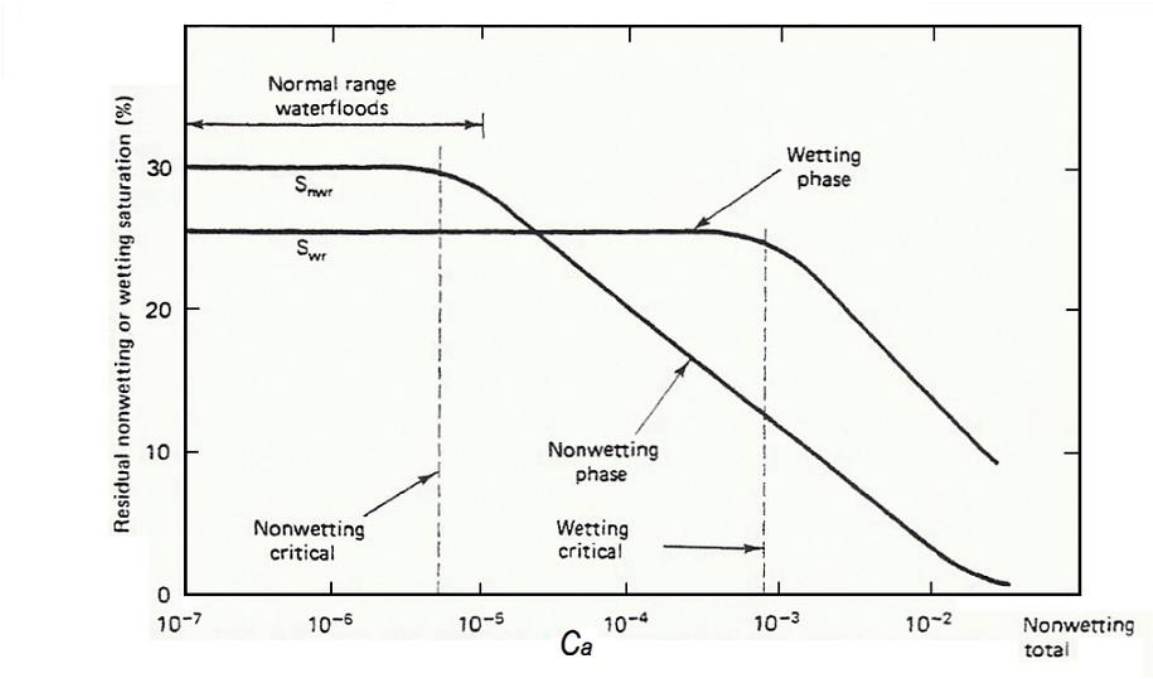

Figure 2.8 – Schematic of the capillary desaturation curves (CDC) of both the wetting and non-wetting phase showing the sharp residual saturation declined once a critical capillary number is reached (adapter from Lake 1988).

The pattern displayed by the curves in Figure 2.8 is in accordance with the discussion on pore-scale mobilization of oil ganglia presented previously: once some critical capillary number is achieved, the curve forms a knee and the residual saturation falls sharply from the initial plateau. However, the model described in Section 2.2.2 is inadequate for dealing with large populations of ganglia because it treats each ganglion individually and requires an accurate description of the porous media structure. Therefore, direct application of this model to a REV length scales is not possible.

A suitable method for CDC estimation needs to bridge the gap between pore-scale physics and effective properties of continuum porous media modeling, to which abundant experimental data exists. This was accomplished by the method proposed by (Stegemeier 1974, 1977) and described in the following.

As shown in Figure 2.9, a generic ganglion with length ΔL a characteristic pore neck radius r_n is subjected to potential gradient $\nabla\phi$.

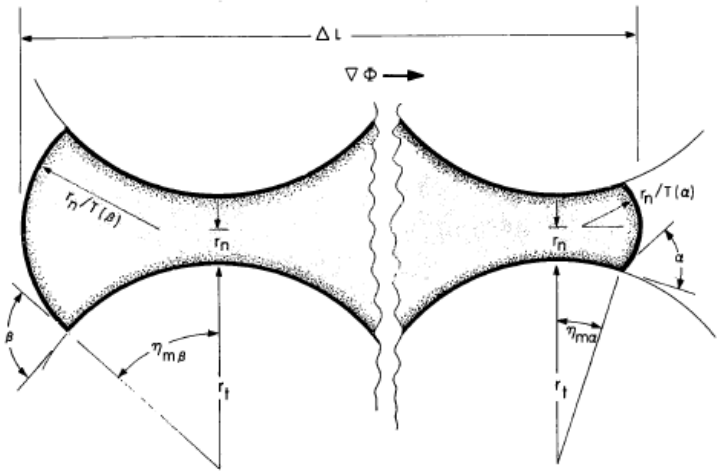

Figure 2.9 – Generic ganglion with length $\Delta \boldsymbol{L}$ and a characteristic pore neck radius $\boldsymbol{r_n}$ being subjected to potential gradient $\boldsymbol{\nabla\phi}$ (Stegemeier 1977).

The condition for mobilization is given by

$$\nabla\phi.\Delta L > \frac{2\sigma}{r_n}\psi \tag{2.14}$$

where the correction factor ψ accounts for the difference between the upstream and downstream interfaces of the ganglion:

$$\psi = F(\theta_A) - \frac{F(\theta_R)}{r_b/r_n} \tag{2.15}$$

where r_b is a characteristic pore body radius. As mentioned in Section 2.2.2, the interfaces of a ganglion being mobilized are at critical drainage curvature downstream and critical imbibition curvature upstream. Instead of an exact description of the pore bodies and necks, evaluating ψ requires some estimate of the neck-to-body ratio of the pore, possibly from a photomicrography of the sample, and an estimate of the dynamic contact angles. If the pore necks are assumed to resemble a toroidal geometry as suggested in Figure 2.9, the function $F(\theta)$ is given by Eq. (2.5).

In order to quantify ΔL, the dimensionless filament length is defined

$$f = \frac{\Delta L}{r_{ganglion}} \tag{2.16}$$

where $r_{ganglion}$ is the average radius of a ganglion. The advantage of dealing with f is that it does not depend on pore geometry or fluid property. It represents the maximum length a liquid filament can exist before breaking up into parts. Rayleigh instability limits the filament length to about $f \approx 0.9$.

The average radius of a trapped ganglion can be estimated from its length by a force balance:

$$r_{ganglion} = \frac{2\sigma}{\Delta L\, \nabla\phi} \tag{2.17}$$

Hence, by combining Eqs. (2.16) and (2.17):

$$\Delta L = \sqrt{\frac{2\sigma f}{\nabla\phi}} \tag{2.18}$$

A key feature of this model is obtaining the characteristic pore neck length of the ganglia at a given residual saturation S_{nwr} through the IR curve. Considering a point of the IR curve with some initial non-wetting saturation S_{nwI} and its respective residual non-wetting saturation $IR(S_{nwI})$. If the applied potential difference equals the drainage capillary pressure at this point $P_{c,drain}(S_{nwI})$, a pore-volume fraction of non-wetting phase corresponding to $IR(S_{nwI})$ would be mobilized, leaving a residual saturation $S_{nwr} = IR\big(S_{nwI,max}\big) - IR(S_{nwI})$, where $S_{nwI,max}$ is the non-wetting saturation at irreducible wetting phase. Therefore, from Eq. (2.13) and the IR curve:

$$r_n(S_{nwr}) = r_n\left(IR\big(S_{nwI,max}\big) - IR(S_{nwI})\right) = \frac{2\sqrt{K/\emptyset}}{j_{Le}(S_{nwI})} \tag{2.19}$$

Finally, Eqs. (2.18) and (2.19) can be substituted into Eq. (2.14) to yield a mobilization condition with parameters defined macroscopically:

$$\frac{K\nabla\phi}{\sigma} \geq \left[\emptyset {j_{Le}}^2\right] \cdot [\psi^2] \cdot \left[\frac{1}{2f}\right] \tag{2.20}$$

Each term between brackets on the right-hand side isolates the influence of the following, respectively: rock structure, pore geometry and fluid filament stability. The term on the left-hand side is equivalent to the capillary number. A more familiar representation of the capillary number is obtained by substituting the Darcy equation (2.10) written for the wetting phase flow:

$$Ca = \frac{V_{darcy}\eta_e}{\sigma} \geq \left[\emptyset {j_{Le}}^2\right] \cdot [k_{rw}\psi^2] \cdot \left[\frac{1}{2f}\right] \tag{2.21}$$

The expression above relates Ca and S_{nwr}, being thus sufficient for constructing the CDC.

CHAPTER 3: Fundamentals of Magnetism

The most prominent feature of a ferrofluid is its capacity to interact with magnetic fields. In order to describe the nature of this interaction and its consequences to the ferrofluid dynamics, which is the focus of the next chapter, we need to understand the concepts upon which magnetism is based. The goal of this chapter is to present a theoretical foundation for these concepts.

Strictly speaking, the laws governing electromagnetic phenomena can only be described at a microscopic level. Nonetheless it is usually preferred by engineers to work with a macroscopic electromagnetic theory in which the phenomena are mediated by macroscopic vector fields. It is possible to demonstrate with the aid of thermodynamics (Liu and Stierstadt 2009) that the micro- and the macroscopic formulations are equivalent and that the macroscopic vector fields can be interpreted as spatial averages of fields that exist at a microscopic level. The macroscopic approach suffices for the study of ferrohydrodynamics. In fact, the magnetic effects in the theory presented in the subsequent chapter rely solely on three macroscopic fields: the magnetic field $\vec{H}$, the induction field $\vec{B}$ and the magnetization vector $\vec{M}$.

There are two sources of magnetism: the motion of electric charges (electric current) and the spin of elementary particles in the atoms forming solid matter. While the

first refers to a condition that can be imposed experimentally, the latter characterizes an intrinsic property displayed by some materials.

The relation between the field $\vec{B}$ and an electric current is given by a volume integral known as the Biot-Savart law:

$$\vec{B}(\vec{r}) = \frac{\mu_o}{4\pi}\int_V \frac{(\vec{J}dV)\times\overrightarrow{r'}}{\left|\overrightarrow{r'}\right|^3} \tag{3.1}$$

where $\vec{J}$ is the current density vector (current per unit of area), $\mu_o = 4\pi \cdot 10^{-7}\, NA^{-2}$ is the magnetic permeability in free space, $\overrightarrow{r'}$ is the displacement vector from a point where the integrand is being evaluated to the position $\vec{r}$ where the field $\vec{B}$ is being evaluated. $\vec{B}$ has the unit of Tesla (*T*), although it is commonly measured in Gauss units ($G = 10^{-4}T$).

As $\vec{B}$ can be generated by an electric current, it can conversely induce a force that will affect electric currents. This force is called Lorentz force and, in the absence of an external electrostatic field, is given by

$$\vec{F}_{Lorentz} = \int_V \vec{J} \times \vec{B}\, dV \tag{3.2}$$

Lastly, electric currents and the distribution of $\vec{B}$ must also obey to Ampere's circuit law:

$$\oint_C \vec{B}.dl = \mu_o \int_S \vec{J} \cdot dS \tag{3.3}$$

In the expression above, the left-hand side consists of a line integral of $\vec{B}$ along a path *C* enclosing the surface *S* and the integral on the right-hand side represents the total

current flowing through S. Whenever the distribution of $\vec{B}$ is well-determined around a closed-curve, known in this context as Amperian loop, Eq. (3.3) provides a simple way of evaluating currents.

The Eqs. (3.1) to (3.3) provide a general framework for solving problems involving magnetic effects and electric currents in the free space. However, these expressions alone are not sufficient for describing magnetic effects arising from the intrinsic magnetism of materials. For the sake of ferrohydrodynamics, this second class of magnetism is far more important than the first, as ferrofluids, for being able to interact with magnetic fields even in the absence of electric currents, can be taken as magnetic materials.

Modeling at a macroscopic level the magnetic fields generated by a magnetic material is not an easy task. The two most relevant approaches differ by the concepts employed but yield the same results. The fist approach, known as Gilbert model, is based on an analogy with electrostatics in which a magnetic pole plays the role of the electric charge and generates a field $\vec{H}$ according to the Coulomb's law. The field induced by the magnetic pole translates as the spatial distribution of a force per unit of magnetic pole strength which attracts poles with the opposite polarity and repels the ones with the same polarity. Therefore, a small volume of magnetic material can be seen as two opposite point poles separated by a small distance, i.e. a magnetic dipole. More details about this approach can be found in Rosensweig (1997).

The concept of magnetic poles is useful for some magnetostatic calculations, but it lacks a rigorous physical meaning. For instance, the field generated by a magnetic

dipole consists of the superposition of the fields generated by the poles individually and thus its existence relies on the existence of a field associated to an isolated pole, although isolated magnetic poles were never found in nature.

An alternative way of modeling magnetic materials is the Amperian currents model, which postulates that magnetism emerges from the combined effect of electric charges moving in small loops contained by the material's volume. The currents forming these microscopic loops, known as Amperian currents or bound currents, face no resistance and hence cannot be considered currents in a conventional sense. Yet the magnetic effects they produce are completely analogous to the ones observed in macroscopic current loops. The advantage of this approach over the former lies on the intuitive connection it provides between the macroscopic fields and the microscopic processes that generate them, as the Amperian currents can be linked to the orbital motion of electrons.

Given an external field $\vec{B}$ that intersects a current loop sufficiently small so that $\vec{B}$ can be taken as uniform within its area, it can be shown (Whitmer 1962) that the Lorentz force that the loop undergoes due to the external field is

$$\vec{F}_{loop} = \nabla(\vec{m} \cdot \vec{B}) \tag{3.4}$$

Moreover, the torque associated to this force is

$$\vec{\tau}_{loop} = \vec{m} \times \vec{B} \tag{3.5}$$

The parameter $\vec{m}$ that appears on the two expressions above is called magnetic moment and is given by

$$\vec{m} = \int_S I_{loop}\hat{n}\, dS \tag{3.6}$$

where I_{loop} is the intensity of the current loop and *S* is its area. The magnetic moment can be interpreted as the quantity that determines the strength of torque experienced by the circuit loop under an external field. The torque acts in the orientation of aligning $\vec{m}$ to $\vec{B}$.

According to the Amperian current model, the current loop considered above is representative of an infinitesimal volume of magnetic matter if we take its current intensity as the intensity of the Amperian current. In order to generalize the analysis to finite volumes, the force and torque obtained for the loop should be written per unit of volume, which can be accomplished by defining the magnetization $\vec{M}$:

$$\vec{M} = \frac{d\vec{m}}{dV} \tag{3.7}$$

It can be shown (Whitmer 1962) from Eq. (3.6) and the definition of $\vec{M}$ that

$$\nabla \times \vec{M} = \vec{J}_{amp} \tag{3.8}$$

where $\vec{J}_{amp}$ is the Amperian current density. The relevance of the magnetization (or magnetic moment per unit volume) comes from being directly linked to the microscopic currents that generate magnetism. Therefore, it serves as a measure of the degree of magnetic polarization of a material.

Differentiating Eq. (3.4) with respect to volume leads to the density of the body force acting on a medium with magnetization $\vec{M}$ when subjected to a field $\vec{B}$, known as Kelvin force:

$$\vec{f}_{kelvin} = \nabla(\vec{M} \cdot \vec{B}) \tag{3.9}$$

By applying Eq. (3.3) in its differential form, $\nabla \times \vec{B} = \mu_o \vec{J}$, to a magnetic material with no moving electric charges other than the Amperian currents and substituting the current density by the magnetization through Eq. (3.8):

$$\nabla \times \left(\frac{\vec{B}}{\mu_o} + \vec{M}\right) = 0 \tag{3.10}$$

The curl-free field defined by the expression between parenthesis is the magnetic field $\vec{H}$. It follows from the equation above that

$$\vec{B} = \mu_o(\vec{M} + \vec{H}) \tag{3.11}$$

This demonstrates that the two fields that arise in macroscopic magnetism are related by the magnetization of the medium. In a free space, the fields are simply distinguished by a constant.

3.1 MAGNETIC SOLIDS

It was demonstrated earlier in this chapter that the magnetization vector $\vec{M}$ relates the capacity of a medium to produce a magnetic field of its own. The presence of this field is manifested by altering the relation between $\vec{B}$ and $\vec{H}$, as seen in Eq. (3.11). Ferrofluids display magnetization by a particular kind of process that will be described in

Chapter 4. Nonetheless, it is useful to discuss the different kinds of magnetization exhibited by natural magnetic solids to form a basis for studying ferrofluids.

In general, the magnetization of a natural material can be described in terms of the magnetic moments associated with the elementary particles in its atoms. The magnetic moments are often arranged in a way such that they cancel out and the material yields no magnetization. In other cases, some magnetization exists either permanently or by influence of external factors that disturb the arrangement of the magnetic moments, such as a change of temperature or an imposed magnetic field. The different propensities of magnetic moments alignment and reactions to external factors characterize different kinds of magnetism.

Paramagnetism is the behavior in which the magnetic moments of a medium are arranged in a way that produces no net magnetization when undisturbed, but are free to align towards an external field. Consequently, the magnetization of a paramagnetic material growths with the strength of the field applied. Diamagnetism consists of the opposite behavior, i.e. magnetic moments tend to align against an external field so that $\vec{M}$ and $\vec{H}$ are oriented in opposite directions. The magnetization resulting from Diamagnetic behavior tends to be weak.

Ferromagnetism is the magnetic behavior displayed by most permanent magnets. In a ferromagnetic material, magnetic moments align parallel to each other spontaneously and hence magnetization exists even in the absence of an external field. Permanent magnetization also occurs in ferrimagnetism. Ferrimagnetic materials, however, have atoms with magnetic moments in opposite directions and each direction has a different

moment magnitude. The imbalance between the magnitudes is responsible for the magnetization.

A rigorous analysis on how the subatomic structure of the medium relates to its magnetism is out of the scope of this text and it is only fully achievable by resorting to quantum mechanics. Fortunately, the magnetic behaviors described above can be represented mathematically at a macroscopic level through appropriate constitutive models.

3.2 MAGNETOSTATIC FORMULATION

All the governing relations for magnetism presented throughout this chapter implicitly assumed steady state conditions. In addition, effects of electric nature that can influence magnetic fields were disregarded. Given these assumptions, Eq. (3.10) determines that $\vec{H}$ is irrotational. Combining this assertion with the Gauss's law of magnetism yields the magnetostatic formulation:

$$\nabla \times \vec{H} = 0$$

$$\nabla \cdot \vec{B} = 0 \tag{3.12}$$

It is easily verifiable that the two equations above can be derived directly form the macroscopic Maxwell equations by taking the time-derivatives and the free currents as zero. The resulting formulation is ideal for modeling ferrohydrodynamics problems in which the magnetic effects arise entirely due to a permanent external field.

Applying Eqs. (3.12) to a magnetized ferrofluid surrounded by media that can be either non-magnetic or display a different kind of magnetic behavior creates important interface effects. In order to better understand these effects, the concept of magnetic permeability is introduced:

$$\mu = \mu_o \left(\left| \frac{M}{H} \right| + 1 \right) \tag{3.13}$$

It should be noticed that μ is defined such that $\vec{B} = \mu \vec{H}$ and thus it is a practical way of expressing magnetic behaviors in which $\vec{H}$ and $\vec{M}$ are parallel. In the non-magnetic media, the magnetic permeability is reduced to the permeability in free space $\mu = \mu_o$. Another case of constant μ occurs in materials that display linear magnetization, i.e. $\vec{M}$ varies linearly with $\vec{H}$ according to a constant χ known as magnetic susceptibility, which gives

$$\mu = \mu_o (1 + \chi) \tag{3.14}$$

An interface between the media (+) and (-) with different magnetic permeability is shown in Figure 3.1.

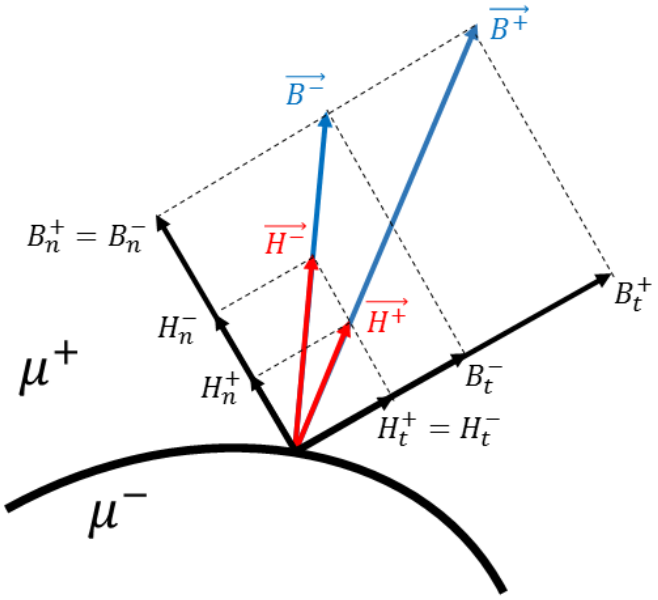

Figure 3.1 – Magnetic and induction field being disturbed by the presence of an interface of magnetic permeability discontinuity

Satisfying both magnetostatic equations (3.12) when applied at the interface vicinity requires the tangential component of $\vec{H}$ and the normal component of $\vec{B}$ to be the same on both sides. As the sketch shows, in order to accommodate these conditions, the two fields change in both direction and magnitude across the interface. The following relations must hold:

$$\frac{H_n^+}{H_n^-} = \frac{\mu^-}{\mu^+}$$

$$\frac{B_t^+}{B_t^-} = \frac{\mu^+}{\mu^-} \tag{3.15}$$

It is convenient to rewrite the magnetostatic formulation in a way that makes the influence of the magnetic permeability distribution explicit. This can be achieved by defining a potential function ψ such that $\vec{H} = -\nabla\psi$. Being described as the gradient of a scalar function guarantees $\vec{H}$ is irrotational and hence removes one of the equations in (3.12). By substituting the potential function into the remaining equation:

$$\nabla \cdot (-\mu\nabla\psi) = 0 \tag{3.16}$$

In the special case of a uniform magnetic behavior, the expression above is reduced to a Laplace equation. The interface relations (3.15) can also be written in terms of the potential:

$$\frac{\nabla\psi^{+}\cdot\hat{n}}{\nabla\psi^{-}\cdot\hat{n}} = \frac{\mu^{-}}{\mu^{+}} \tag{3.17}$$

According to this new formulation, Eq. (3.16) is solved for ψ with the boundary condition given by Eq. (3.17). The domain of the solution is a region with continuous μ and its boundaries reflect transitions to an adjacent domains with different magnetic behaviors. The set of all domains must be solved simultaneously because the boundary condition employed has a coupling effect.

CHAPTER 4: Ferrohydrodynamics

Ferrohydrodynamics (FHD) is the science that deals with the mechanics of fluid motion influenced by strong forces of magnetic polarization (Rosensweig 1997). The study of FHD implies the existence of a specific kind of liquid capable displaying sufficient magnetization so that the magnetic forces resulting from its exposure to an external field are strong enough to compete with other forces of fluid dynamics. Liquids of this kind are called ferrofluids.

A common way of producing fluids that are controllable by magnetic fields is by applying an electric current through some conductive fluid, such as a liquefied metal, and resorting to the Lorentz force of Eq. (3.2) that emerges when an external field intercepts an applied current at an angle. The fluids controlled by Lorentz forces are the subject of Magnetohydrodynamics (MHD), which should be distinguished from FHD. The limitations of MHD are the constant need for an electric current and the fact that the Lorentz force is typically small except for extremely strong currents. Ferrohydrodynamics' control of ferrofluids was meant to overcome these limitations by relying on the magnetic force that occurs when magnetic matter interacts with an external magnetic field that can be applied remotely.

Melting natural ferromagnetic solids is not a suitable procedure for obtaining ferrofluids because the Curie temperature of a material is always well below its melting point (Kittel 1996). It means that the ferromagnetic solids would lose their permanent magnetisms before becoming liquids. Another approach that could potentially lead to

ferrofluids is taking advantage of the paramagnetism displayed by several water-soluble salts. Unfortunately, paramagnetism tends to be a very weak kind of magnetic behavior and thus the dynamics of the salt solutions is not expected to be significantly affected by a magnetic force.

The desired ferrofluid properties can be achieved with ferri- or ferromagnetic nanoparticles coated with some surfactant or polymer for their dispersion stability when suspended in a liquid carrier. This concept emerged in the mid-sixties, when the first stable dispersions were obtained (Papell 1964). Nowadays, a wide-variety of techniques (Charles 2002) can be employed to produce spherical particles with diameters in the range of 3-15 nm and stabilizing coatings.

In most of the practical applications, the nanoparticles are made of ferrite compounds, usually a mix of magnetite and maghemite (Charles 2002). This kind of nanoparticle tends to be reliable and durable because the oxidation of magnetite to maghemite has a relatively small effect on the magnetic moment of the nanoparticle. Metal nanoparticles, such as the ones made of iron and cobalt, yield ferrofluids with higher saturation magnetizations, but also suffer greater loss of magnetic properties with oxidation.

4.1 STABILITY OF FERROFLUIDS

The theory presented in this chapter for the magnetization and motion of ferrofluids is built upon the assumption that the nanoparticles remain dispersed in the

liquid carrier under all conditions. In practice, ferrofluids have stability thresholds that, if surpassed, may lead aggregation of the constituent particles and their sedimentation. It is necessary to identify these thresholds and the variables controlling them in order to ensure the validity of the FHD approach.

Nanoparticles are subjected to gravity and magnetic field gradients, which can both affect stability. Thermal agitation must be strong enough to keep the nanoparticles in Brownian motion in spite of these other forces. Stability can be assessed by comparing the amount of energy associated to each of the mechanisms involved. In the case of thermal agitation:

$$E_T = k_b T \tag{4.1}$$

where $k_b = 1.38 \cdot 10^{-23}\ \mathrm{N.m.K^{-1}}$ is the Boltzmann's constant and T is the temperature.

For simplicity, it is assumed that the nanoparticles are perfectly spherical with diameter d_p and possess a uniform permanent magnetization M_o. The temperature is taken as ambient $T = 298\,K$ and magnetite is used as reference material for the nanoparticles properties: $M_o = 4.5 \cdot 10^5\ \mathrm{A/m}$ and $\rho_s = 5.2 \cdot 10^3\ \mathrm{kg/m^3}$.

Given the height of the ferrofluid column h and the density difference $\Delta\rho$ between the solid magnetic material and the liquid carrier, the nanoparticles resist settling under gravity if the following condition is fulfilled:

$$\frac{\Delta\rho g h \pi {d_p}^3/6}{k_b T} < 1 \tag{4.2}$$

Magnetic nanoparticles tend be attracted to the region in the liquid carrier where the magnetic field is the strongest. It can be shown (Rosensweig 1997) that the work done by the magnetic force displacing the nanoparticle against the field gradient is

$$W_{mag} = \mu_o M_o H \frac{\pi {d_p}^3}{6} \tag{4.3}$$

Imposing W_{mag} to be smaller than the thermal agitation energy of Eq. (4.1) leads to an expression for the maximum particle diameter:

$$d_p \leq \left(\frac{6k_bT}{\pi\mu_o M_o H}\right)^{\frac{1}{3}} \tag{4.4}$$

By setting the parameters in Eq. (4.2) to represent magnetite particles dispersed in water at ambient temperature, it can be verified that the resulting ratio is orders of magnitude smaller than one for reasonable values of h. Therefore, ferrofluid stability is generally not affected by gravity. Performing the same substitutions in Eq. (4.4) and assuming that the ferrofluid is subjected to a moderate field intensity of $H = 1.5 \cdot 10^4$ A/m yields the critical diameter $d_p \leq 10$ nm.

Although most nanoparticles in a ferrofluid are expected to be within the size range that satisfies the stability condition of Eq. (4.4), any agglomeration of nanoparticles into a cluster with greater effective diameter would necessarily compromise stability. Hence, thermal agitation must also overcome the magnetic dipole-dipole attraction that exists between particles.

The schematic in Figure 4.1 shows two nanoparticles with equal diameter and magnetization that came to proximity.

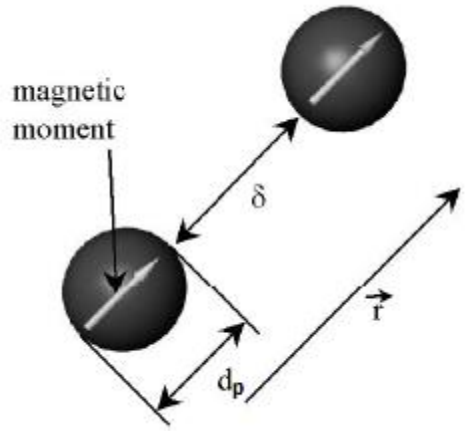

Figure 4.1 – Schematic of two nanoparticles with equal diameter and aligned magnetic moments approaching each other under the influence of dipole-dipole attraction (adapted from Odenbach 2002).

The strongest attraction occurs when the magnetic moments of each particle are both aligned towards the distance vector $\hat{r}$, as represented in Figure 4.1. Under this condition, it is possible to demonstrate (Rosensweig 1997) that the energy associated with the dipole-dipole attraction is given by

$$E_{dd} = \frac{\pi}{9}\frac{\mu_o {M_o}^2 {d_p}^3}{(l+2)^3} \tag{4.5}$$

where $l = 2\delta/d_p$ is the normalized surface-to-surface distance between particles . The magnitude of E_{dd} grows as the particles get closer to each other. In the limiting case of

$l = 0$, thermal agitation can only ensure stability when

$$d_p \leq \left(\frac{72\, k_b T}{\pi \mu_o {M_o}^2}\right)^{1/3} \tag{4.6}$$

Substituting the parameters with the data used in the previous cases indicates that roughly the same particle size-range obtained with Eq. (4.4) also satisfies Eq. (4.6).

Unfortunately, overcoming magnetic dipole-dipole attraction might not be sufficient to prevent the agglomeration of particles. In near-contact situations, the attraction between particles is controlled by van der Waals force, which arise from fluctuations in the electric dipole-dipole interaction. The Hamaker model for the van der Waals attraction energy between equal spheres yields

$$|E_{v.d.W.}| = \frac{A}{6}\left[\frac{2}{l^2+4l} + \frac{2}{(l+2)^2} + \ln\left(\frac{l^2+4l}{(l+2)^2}\right)\right] \tag{4.7}$$

where A is the Hamaker constant which can be determined for a particular combination of particles and medium. Except for the case in which the dielectric properties of the particles match those of the liquid carrier, A is non-zero and the magnitude of $|E_{v.d.W.}|$ diverges with $l \to 0$.

Thermal agitation alone cannot prevent the agglomeration of particles separated by arbitrarily small distances. This is the reason why the nanoparticles in ferrofluids are coated with long-chain surfactant molecules. Once the distance between the nanoparticles becomes comparable to twice the thickness of the surfactant layer δ_s, the mechanism of steric repulsion creates a barrier against further approximation. The steric repulsion

energy for a pair of equal neighboring spheres was calculated by (Rosensweig et al. 1965) and it is given by

$$E_{steric} = \frac{k_b T \pi {d_p}^2 \xi}{2}\left[2 - \frac{l+2}{t}\ln\left(\frac{1+t}{1+l/2}\right) - \frac{l}{t}\right] \tag{4.8}$$

where $t = 2\delta_s/d_p$ is the normalized surfactant layer thickness and ξ is the surface concentration of surfactant molecules.

If the nanoparticles are dispersed in water and the particles carry surface charges, the electrostatic repulsion is another mechanism that prevents the particle agglomeration. For the ferrofluids in oil reservoir applications, the carrier brine generally has a high salinity, in which case the electrostatic repulsion is usually insignificant and, therefore, is not considered here.

The net potential energy resulting from the superposition of the van der Waals and steric energies has a hump shape as illustrated by Figure 4.2. The maximum in this curve acts as an energy barrier that prevents the nanoparticles from reaching each other. It can also be observed in Figure 4.2 that the magnetic dipole-dipole attraction is considerably smaller than the other energy components, except for large distances.

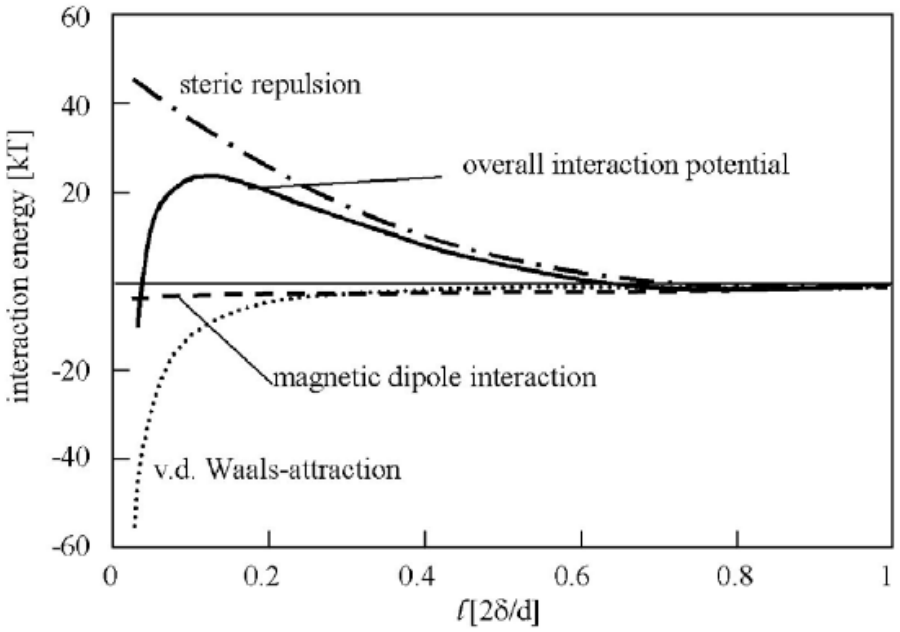

Figure 4.2 – Energy potentials associated to different attraction and repulsion mechanisms. Calculations assumed 10 nm for the nanoparticles diameter, 2 nm for the surfactant layer thickness and 1 n$\mathbf{m^{-2}}$ for the surfactant surface density. The net interaction potential prevents the contact between nanoparticles by forming a barrier of about 20 $\boldsymbol{k_b}$T (adapted from Odenbach 2002).

4.2 FERROFLUID MAGNETIZATION

Ferrofluids display a magnetic behavior very similar to that of paramagnetic materials, but with much stronger magnetizations than average paramagnetic salts. Hence, the magnetic behavior of ferrofluids is known as superparamagnetism.

Each nanoparticle in a ferrofluid has an embedded magnetic moment, which, in the absence of an external magnetic field, is randomly oriented due to the Brownian fluctuations. This configuration yields no ferrofluid magnetization. When an external field is applied, the field becomes a preferential direction of alignment for the magnetic moments and the ferrofluid becomes magnetized. As such shift is reversible, one important characteristic of supermagnetism is the reversibility of magnetization without any hysteresis. If the applied field is increased, the magnetic moments will further overcome thermal agitation to align towards the field causing greater ferrofluid magnetizations. In the limiting case of complete alignment, the ferrofluid achieves its saturation magnetization M_s. Once the field is removed, the magnetic moments revert to the original unaligned configuration.

If a ferrofluid is treated as consisting of monodispersed non-interacting nanoparticles each of which with an equal embedded magnetic moment $\vec{m}$, its magnetization can be modeled by

$$\frac{M}{M_s} = \coth \gamma H - \frac{1}{\gamma H} \tag{4.9}$$

with

$$\gamma = \frac{\mu_o |\vec{m}|}{k_b T} \tag{4.10}$$

The expression on the right-hand side of Eq. (4.9) is known as Langevin's function and is classically used in the study of paramagnetism. An improved model is obtained by considering that, under equilibrium, the ferrofluid magnetization is parallel to the magnetic field:

$$\vec{M} = M_s \left[\coth(\gamma H) - \frac{1}{\gamma H}\right] \frac{\vec{H}}{|\vec{H}|} \tag{4.11}$$

Moreover, it is useful to notice that for a ferrofluid with n particles per unit volume:

$$M_s = n|\vec{m}| \tag{4.12}$$

Under isothermal conditions, the superparamagnetic behavior described by Eq. (4.11) is a function solely of the magnetic field intensity. The magnetization grows in a Langevin's fashion from zero to asymptotically approaching M_s as $|\vec{H}|$ is increased. In the low range of values, the Langevin's function is nearly linear:

$$\coth x - \frac{1}{x} \approx \frac{x}{3} \qquad \text{for } x < 1 \tag{4.13}$$

It implies that a ferrofluid displays linear magnetization when being subjected to relatively weak fields. In this case, its magnetic behavior can be determined by a constant initial susceptibility χ_o given by

$$\frac{M}{H} \approx \chi_o = \frac{\gamma M_s}{3} \tag{4.14}$$

A fundamental feature of ferrofluids is their relatively high initial susceptibilities. Considering a magnetite nanoparticle with 10 nm diameter, a simple calculation (Odenbach 2002) shows its magnetic moment to be $|\vec{m}| = 2.0 \cdot 10^{-19}\,\mathrm{A.m^2}$. For a typical concentration of $n = 2.5 \cdot 10^{23}\,\mathrm{particles/m^3}$ and ambient temperature, a

ferrofluid would display $M_s = 5.0 \cdot 10^4$ A/m and $\chi_o = 1.0$ according to Eqs. (4.12) and (4.14), respectively.

In practice, susceptibilities much larger than the one calculated above are not unusual. Some commercial ferrofluids, for instance, with the same particle size can have $\chi_o = 12.6$ (https://ferrofluid.ferrotec.com/). Increasing particle concentration while preserving the dispersion stability can improve magnetization. It must be noted, however, that Langevin's theory is not adequate for particularly high particle concentrations because it assumes no interaction between the particles.

All the discussion presented on this subsection referred to equilibrium magnetization. Nonetheless, the transients between changes in magnetic field and the equilibrium magnetization being achieved are important for some ferrofluid applications. The process by which the magnetic moments of nanoparticles adjust to new magnetic fields is called relaxation.

Two relaxation mechanisms can be distinguished. In Neel relaxation, the magnetic moment shifts its direction in relation to the crystal structure of the particle, whereas in Brownian relaxation, the entire particle rotates to alter its magnetic moment orientation. To each of these mechanism there is a characteristic duration time: namely τ_B and τ_N for Brownian and Néel relaxations, respectively. Naturally, relaxation occurs by the mechanism with the smallest characteristic time.

While τ_N grows at an exponential rate with the particle size, τ_B only grows linearly. This suggests the existence of a diameter threshold after which Néel relaxation is replaced with Brownian relaxation as the dominant mechanism (Odenbach 2002). An

example of this threshold can be seen at the point where the τ_N and τ_b curves intercept each other in Figure 4.3.

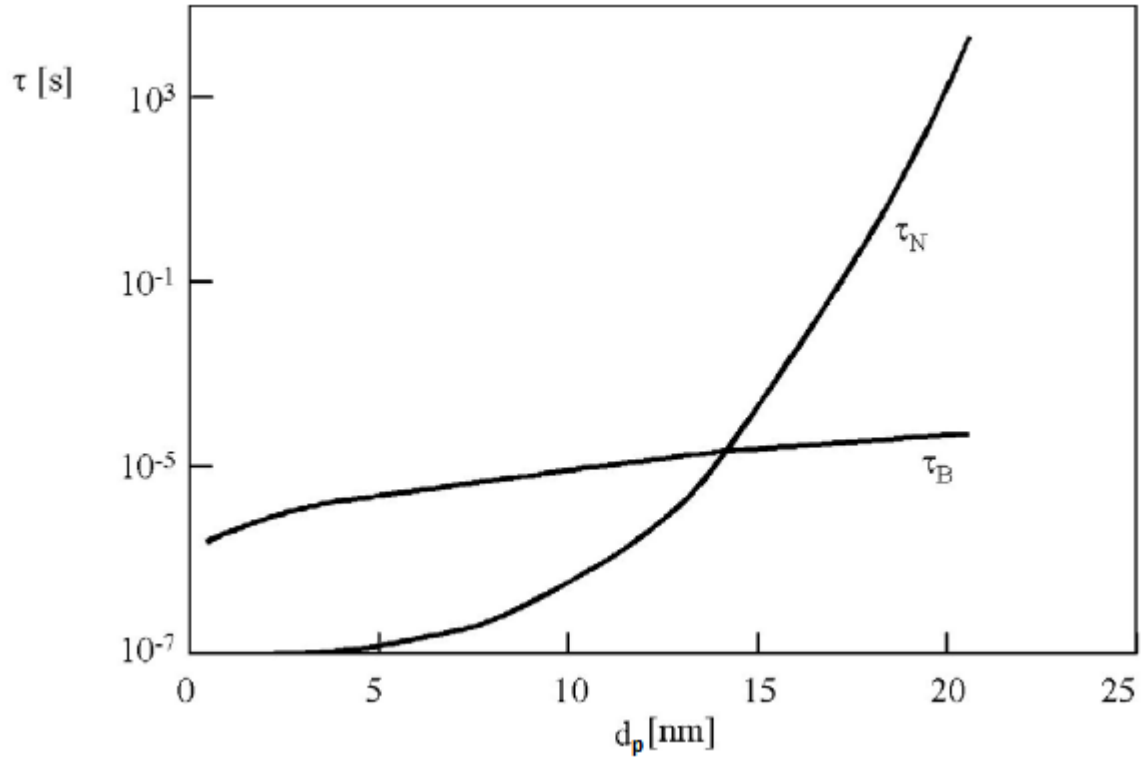

Figure 4.3 – Theoretical estimation of the characteristic Brownian τ_B and Néel τ_N relaxation times. Brownian mechanisms are expected to dominate relaxation for particles with $\mathbf{d_p > 15\ nm}$ (adapted from Odenbach 2002).

For particularly small nanoparticles with single magnetic domains, Néel relaxation can be taken as instantaneous for practical purposes and the ferrofluid is said to display soft magnetization. The assumption of soft magnetization will be implicit in the entire discussion that follows.

4.3 EQUATIONS OF MOTION

The mechanics of magnetized ferrofluids differs from traditional fluid mechanics because of the presence of stresses of magnetic nature. It is therefore necessary to quantify these stresses in order to write the ferrofluid equations of motion. In its most general form, the magnetic stress tensor of a ferrofluid is

$$\boldsymbol{T}_m = -\left\{\int_0^H \mu_o \left[\frac{\partial(\upsilon M)}{\partial \upsilon}\right]_{H,T} dH + \frac{1}{2}\mu_o H^2\right\}\boldsymbol{I} + \vec{B}\vec{H} \tag{4.15}$$

where υ is the specific volume. A complete derivation of this formula involves advanced thermodynamic treatment and can be found in (Rosensweig 1997).

The stress tensor of Eq. (4.15) contains all the information regarding the ferrofluid magnetic stresses. Given a plane surface element oriented according to a normal vector $\hat{n}$, the normal component of the magnetic traction acting on this surface is given by

$$t_n = \hat{n} \cdot \boldsymbol{T}_m \cdot \hat{n} = -\mu_o \int_0^H M dH + \frac{\mu_o}{2}(H_n^2 - H_t^2) + \mu_o M_n H_n \tag{4.16}$$

Moreover, the volumetric density of the magnetic body force acting on a ferrofluid $\vec{f}_m$ is obtained by taking the divergence of the tensor:

$$\overrightarrow{f_m} = \nabla \cdot \boldsymbol{T}_m = -\nabla\left[\mu_o \int_0^H \left(\frac{\partial M\upsilon}{\partial \upsilon}\right)_{H,T} dH\right] + \mu_o M \nabla H \tag{4.17}$$

It can be verified through some substitutions that the second term on the right-hand side is the Kelvin force of Eq. (3.9), which emerges when magnetized matter interacts with a magnetic field. The Kelvin force is added of a term representing the

influence of compressibility on the mass density of magnetic moment, known as magnetostrictive effect. Considering that ferrofluid compressibility is mostly due to the non-magnetic liquid carrier, this term can usually be ignored.

There are several arbitrary ways of grouping the terms that appear in Eq. (4.17). In this work, we choose a formulation that that exploits the mathematical similarity between the magnetic stresses and the fluid pressure:

$$\overrightarrow{f_m} = -\nabla(p_s + p_m) + \mu_o M \nabla H \tag{4.18}$$

where the magnetostrictive pressure p_s and the fluid-magnetic pressure p_m are defined as

$$p_s = \mu_o \int_0^H \upsilon \left(\frac{\partial M}{\partial \upsilon}\right)_{H,T} dH \tag{4.19}$$

$$p_m = \mu_o \int_0^H M dH \tag{4.20}$$

These pressure-like terms are referred to as magnetic pressures in spite of having a completely different physical nature than the thermodynamic pressure.

As usual in fluid mechanics, the conservation of momentum for a control volume containing a ferrofluid is given by the Navier-Stokes equation. In the case of the ferrofluid being magnetized by an external field, the equation must account for the force density of Eq. (4.18). Therefore, the modified incompressible Navier-Stokes equation for ferrofluids is given by

$$\rho \frac{\partial \vec{v}}{\partial t} + (\vec{v} \cdot \nabla)\vec{v} = -\nabla(p + p_s + p_m) + \mu_o M \nabla H + \eta \nabla^2 \vec{v} \tag{4.21}$$

This expression should be solved coupled with a statement of conservation of mass. For an incompressible ferrofluid:

$$\nabla \cdot \vec{v} = 0 \tag{4.22}$$

The formulation presented suggests ferrofluids are Newtonian liquids, which is generally true. The presence of dispersed nanoparticles creates additional dissipations and thus results in some apparent viscosity higher than the viscosity of the carrier liquid, but this apparent viscosity is not expected to change provided the particle concentration remains the same. Theoretical models for predicting the apparent viscosity are available (Rosensweig et al 1965).

However, a very particular kind of non-Newtonian behavior occurs in ferrofluids with $\tau_B > \tau_N$. It is caused by the large velocity gradients formed in the vicinity of particles prevented from rotating because their magnetic moments are locked in the field direction. The stronger is the applied field, the greater is the degree of particle alignment and hence the apparent viscosity of the ferrofluid. This magnetic-field dependence, known as magnetoviscous effect, is described in great detail by Odenbach (2002). For the purpose of ferrofluids displaying soft magnetization, such effect can be ignored.

CHAPTER 5: Pore Scale Model of Ferrofluid-Driven Displacements

The previous section showed how the magnetization of a ferrofluid can affect its motion by inducing stresses of magnetic nature. Although the influence of these additional stresses might be overshadowed by more dominant forces in several fluid mechanics problems, it cannot be ignored in the small velocity and small length scale scenarios typical of porous media displacements. Therefore, achieving our goal of creating a model to analyze the flow of a wetting ferrofluid in a pore geometry under the influence of an external magnetic field requires accounting not only for viscous and capillary stresses but also the magnetic stresses.

As shown in Eq. (4.21) the magnetic stresses can be incorporated into the conservation of momentum in ferrohydrodynamics problems. It should be noted, however, that the resulting formulation is very demanding from a computational point of view, especially in the case of two-phase flows. The magnetic stresses driving the fluid displacement depend on the magnetic field, which in turn depends on the motion of the interface between the fluids. As discussed in Section 3.2, the spatial distribution of the imposed field is affected by the presence of interfaces of magnetic permeability contrast, such as the liquid interface, because these interfaces are associated to discontinuities in $\vec{H}$ and $\vec{B}$ as expressed by Eq. (3.15). Hence, the time-evolutions of the magnetic, induction, pressure and velocity fields are completely interlocked.

For all cases considered in this work, transients are not as important as the equilibrium configurations and the fluid interface motion can be assumed to be quasi-

static because of the strong capillary pressures. It will be shown next that these assumptions lead to a model that enables solving the magnetic and fluid dynamics problems separately.

The magnetic permeability distribution depends on the spatial configuration of the ferrofluid phase. If the liquid interface is assumed to move in a quasi-static fashion, the magnetic permeability distribution can be taken as constant. Provided that both the imposed field and the magnetic permeability are constant, the magnetostatic formulation of Eq. (3.12) is appropriate for describing the magnetic problem. Moreover, by considering that in the characteristic size scale of the pore spaces both inertial force and gravity tend to be negligible, the conservation of momentum of Eq. (4.21) can be simplified to

$$\eta\nabla^2\vec{v} - \nabla(p + p_m + p_s) + \mu_o M\nabla H = 0 \tag{5.1}$$

The expression above corresponds to the equation of motion for a Stokes flow added of two magnetic terms. From the discussion in Section 4.3, the term corresponding to the magnetostrictive pressure (4.19) can be ignored because of the incompressibility of the fluids. Assuming isothermal conditions and that the ferrofluid magnetization is a function only of the magnetic field and temperature, the other magnetic term vanishes everywhere but on the interface between the fluids, because of the discontinuous magnetization. In order to avoid dealing with the interface directly and therefore remove

all magnetic effects from the fluid dynamics problem, we should define regions of homogenous properties.

Associating the subscript (+) to the ferrofluid, the region where $\mu = \mu^+$ is defined as Ω^+. If we assume that the ferrofluid displays linear magnetization, μ^+ becomes a constant. The region Ω^-, with a smaller magnetic permeability $\mu = \mu^- = \mu_o$, consists of the union of two regions: Ω_f^- comprising the non-magnetic fluid and Ω_w^- comprising the wall. The solid-fluid interface surrounding region Ω_w^- is defined as contour Γ_w. The fluid-fluid interface between Ω_f^- and Ω^+ is represented by Γ_f. A schematic illustration of these regions is shown in Figure 5.1.

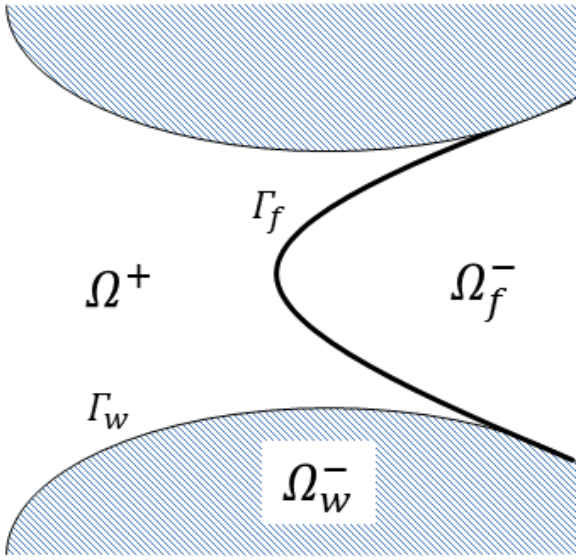

Figure 5.1 – Schematic labeling regions with homogeneous properties and their respective interfaces.

Aided by the above definitions, a new set of equations can be written for the model:

$$\begin{cases} \eta\nabla^2\vec{v} - \nabla p = 0 & \vec{x} \in \Omega^+ \\ \nabla\cdot\vec{v} = 0 & \vec{x} \in \Omega^+ \end{cases} \tag{5.2}$$

$$\vec{v}|_{\Gamma_w} = 0, \;\; \vec{v}|_{\Gamma_f} = 0 \tag{5.3}$$

$$\begin{cases} \nabla^2\psi = 0 & \vec{x} \in \Omega^+ \cup \Omega^- \\ \vec{H} = \nabla\psi & \vec{x} \in \Omega^+ \cup \Omega^- \end{cases} \tag{5.4}$$

$$\nabla\psi^+\cdot\hat{n} = \frac{\mu^-}{\mu^+}\nabla\psi^-\cdot\hat{n}, \quad \nabla\psi^+\cdot\hat{t} = \nabla\psi^-\cdot\hat{t} \quad \vec{x} \in \Gamma_f \cup \Gamma_w \tag{5.5}$$

The pressure and velocity field are obtained from the solution of Eqs. (5.2) with boundary conditions representing no-slip along the solid walls and the velocity of the liquid interface. Considering the assumption of quasi-static interface motion, the interface velocity can be neglected compared to the flow velocity justifying the boundary condition shown. The magnetic problem is solved for the potential function ψ, defined so that $\vec{H} = \nabla\psi$, with boundary conditions associated to magnetic permeability discontinuities (more details in Section 3.2).

Whereas Eqs. (5.2) are solved exclusively within the region Ω^+, Eqs. (5.4) are solved everywhere in the domain and thus (5.5) can be seen as "internal boundary conditions" that appear as a perturbation on the solution field. It will be shown in the next chapter that this kind of situation can be handled by a numerical method that turns these boundary conditions into source terms on the main equation.

Adopting this formulation avoids dealing with the coupling between magnetic and flow fields explicitly. The impact of the magnetic field distribution on the fluid motion is taken into account by enforcing the stress continuity across Γ_f. This remaining compatibility condition is needed because the surface stress due to ferrofluid magnetization acts only on one side of the interface and hence it adds up to the capillary pressure contributing to a greater pressure difference between the magnetic and non-magnetic phases. The net normal magnetic stress acting on Γ_f is given by the traction in Eq. (4.16) evaluated on the non-magnetic side ($\vec{M} = 0$) subtracted from that evaluated on the magnetic side:

$$t_{mag} = \left[-\mu_o \int_0^H M dH + \frac{\mu_o}{2}(H_n^2 - H_t^2) + \mu_o M_n H_n\right]_+ - \left[\frac{\mu_o}{2}(H_n^2 - H_t^2)\right]_- \tag{5.6}$$

Simplifying the expression above and adding it to the Young-Laplace Eq. (2.1) yields the thermodynamic pressure jump across the interface:

$$p^- = p^+ + \mu_o \int_0^{H_+} M dH + \frac{\mu_o}{2} M_n^2 + \sigma\kappa \tag{5.7}$$

It can be observed the appearance of the fluid-magnetic pressure p_m defined in Eq. (4.20) and a new magnetic stress term, which is called normal magnetic pressure:

$$p_n = \frac{\mu_o}{2} M_n^2 \tag{5.8}$$

We can further simplify Eq. (5.7) by considering the ferrofluid displays linear magnetization and dividing the whole equation by a reference capillary pressure, i.e. the capillary pressure of an interface with an uniform curvature κ_o representative of the problem geometry:

$$\frac{p^-}{\sigma\kappa_o} = \frac{p^+}{\sigma\kappa_o} + \frac{\mu_o H^2}{2\sigma\kappa_o}\left[\chi + \chi^2\left(\hat{n}\cdot\frac{\vec{H}}{H}\right)^2\right] + \frac{\kappa}{\kappa_o} \tag{5.9}$$

This dimensionless expression governs the equilibrium of interface Γ_f and serves as the basis of our model. The thermodynamic pressure p^+ corresponds to the pressure field obtained from Eqs. (5.2) evaluated at the vicinity of the interface; the influence of magnetic pressures is calculated through the magnetic field obtained from Eqs. (5.4) also evaluated on the interface. The thermodynamic pressure p^- is a constant, as the pressure inside phase Ω_f^- is uniform. The combination of these terms must be balanced by the capillary pressure, which, for being dependent on curvature, is related to the geometry of the interface. It means that the interface shape must adjust to the stress level locally to achieve equilibrium. The subsequent chapter will show that this formulation of interface equilibrium is very suitable for the implementation of a quasi-static version of the level set method.

The parameter containing the magnetic field intensity in Eq. (5.9) translates as a measure of the strength of magnetization-induced forces relative to the capillary pressure.

Being analogous to the Bond number (measure of the relative importance of the gravity force relative to the capillary pressure), this parameter is named Magnetic Bond number:

$$B_{oM} = \frac{\mu_o {H_{ref}}^2}{2\sigma\kappa_o} \tag{5.10}$$

where H_{ref} is the reference field intensity, which can be chosen as the magnitude of the unperturbed imposed external magnetic field H_{ext}.

It is usual to reference the Magnetic Bond number in the study of ferrofluid interface instabilities (Torres-Dias and Rinaldi 2014). These instabilities are expected to occur for $B_{oM} \gg 1$ and thus can be ignored at pore-space length scales. Given the typical pore size of Berea Sandstone $1/\kappa_o = 10.0\,\mu$m and a moderate magnetic field $H_{ext} = 2.5 \cdot 10^4$ A/m, achieving $B_{oM} \approx 1$ requires particularly small interface tensions, possibly in the range of $\sigma \approx 5$ dyn/cm.

Identifying the dimensionless quantities of the model can highlight the interplay of forces controlling the interface equilibrium. It is clear that the magnetic effects are completely controlled by B_{oM} and χ. The greater is the magnitude of the viscous stresses, the more p^+ varies along the interface. This suggests that the capillary number must compare the amplitude of p^+ with the capillary pressure. However, the fluid mechanics problem is determined by velocity boundary conditions and the pressures are not known a priori. Given that the amplitude of p^+ grows monotonically with $U_{ref}\eta\kappa_o$, where U_{ref} is a characteristic velocity of the problem, it is convenient to write the capillary number as

$$Ca = \frac{U_{ref}\eta}{\sigma} \tag{5.11}$$

For a given problem geometry, each solution can be entirely described by a combination of B_{oM}, χ and Ca.

5.1 Blob Detachment from Pore Surfaces

The first problem considered has $Ca = 0$ in order to focus solely on the balance between capillary and magnetic forces. Its results serve as basis for interpreting more sophisticated scenarios emerging with the presence of a flow field. As shown by the schematic in Figure 5.2, a non-magnetic blob with dimensionless volume $V' = V\kappa_o^2$ is in contact with both the ferrofluid phase and the solid walls. Two geometries are studied: the simple microchannel of Figure 5.2(a) and a sinusoidal pore with small aspect-ratio shown in Figure 5.2(b). For the special case of $V' = \pi$, the blob has point contact with the walls, larger volumes naturally lead to longer contact lengths.

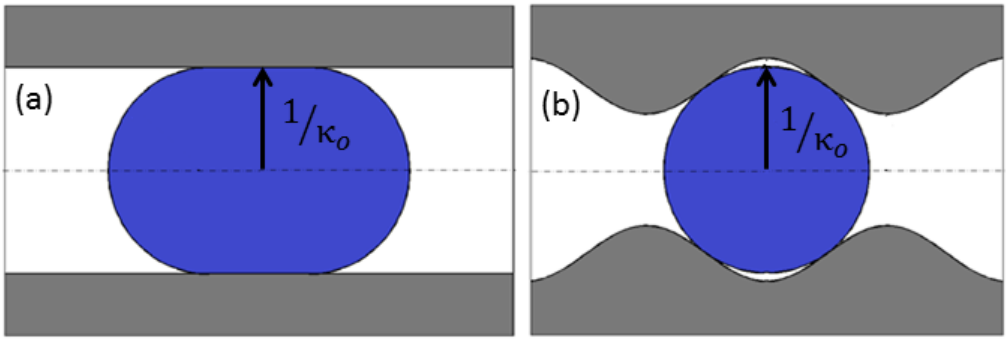

Figure 5.2 – Geometries for studying blob detachment: straight tube (a) and sinusoidal pore geometry with low aspect-ratio (b).

If the fluids are motionless except for the quasi-static interface displacement, viscous stresses are completely absent and the thermodynamic pressure is uniform on both sides of the interface. Hence, the difference $p^- - p^+$ is a constant and the interface equilibrium of Eq. (5.9) dictates that curvature is the greatest in the areas where the combined magnetic stresses are maximum.

Once the external field H_{ext} is applied, the interface moves quasi-statically from its original configuration, in which the capillary pressure is uniform, until achieving a new equilibrium. The goal of this problem is determining the conditions favorable for the detachment of the blob from the solid walls by the effect of magnetic stresses. Different B_{oM} values and magnetic field orientations are attempted.

5.2 STEADY-STATE DROPLET MOTION IN MICROCHANNEL

As a preliminary demonstration of the model capability of handling viscous stresses, a moving droplet inside a two-dimensional microchannel filled with ferrofluid is considered. As seen in Figure 5.3, the droplet moves at constant velocity U_b in a region distant from the microchannel ends. The droplet motion is driven by a force $\overrightarrow{F_b} = F_b \boldsymbol{e}_x$ acting on its volume uniformly. A moving coordinate system is defined such that the equilibrium droplet interface can be taken as stationary. According to this referential, the flow distant to the droplet and on the microchannel walls have velocity $-U_b\, \boldsymbol{e}_x$. The capillary number is written using U_b as reference velocity.

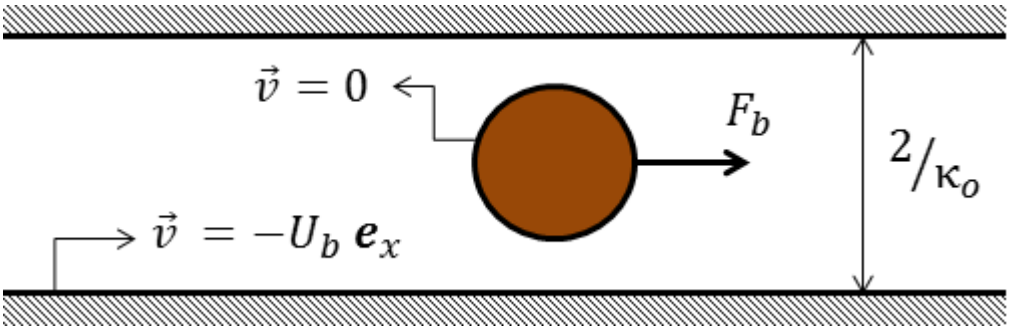

Figure 5.3 – Schematic of a droplet moving at constant speed inside a microchannel filled with magnetized ferrofluid. The velocities are written according to a referential defined so that the equilibrium droplet interface is stationary.

The simulation starts with a perfectly circular droplet at the center of the microchannel separated by small gaps from the solid walls. Subsequently, the liquid interface moves quasi-statically until all the stresses in Eq. (5.9) are balanced. The transient before equilibrium is achieved has no physical relevance, but the final interface configuration corresponds to the shape of the droplet moving in steady-state conditions.

This problem provides a simple but robust testbed for the numerical method presented. In the absence of the magnetic field and the magnetic pressures, the equilibrium droplet shape should resemble the shape attained by a droplet moving at terminal velocity by buoyancy effects, which, for a cylindrical tube geometry, is known experimentally (Borhan and Pallinti 1995). The results obtained with the two-

dimensional model must be qualitatively equivalent to these of an axisymmetric geometry.

Aside from validation purposes, the microchannel problem is also useful for shedding light on how ferrofluid magnetization can affect the flow field in a confined geometry. The intensity and orientation of the external magnetic field applied to the ferrofluid can be adjusted to produce different interface configurations and in turn change the pressure distribution around the droplet. Altering the pressure gradients can be useful to achieve specific goals; for instance, smaller gradients are associated to a smaller pressure drag and thus are desirable for applications involving the delivery of the droplet to a target location.

Two magnetic field configurations are attempted: horizontal and vertical. For each configuration and a given combination of the three dimensionless parameters, an interface equilibrium shape is obtained with its corresponding force F_b. The magnitude of F_b translates directly as a measure of the pressure drag.

In order to calculate F_b, its effect to the interface equilibrium must be taken into account. This is accomplished by the addition of term $F_b \mathrm{x}$ to Eq. (5.7), noticing that $\overrightarrow{F_b} = \nabla \cdot (F_b \mathrm{x} \boldsymbol{I})$. This new pressure jump is defined in a way to zero the average horizontal component of the net force acting on the interface:

$$\int_{\Gamma_f} (p_m + p_n + \sigma\kappa + F_b x)\hat{n} \cdot \boldsymbol{e}_x dA = 0 \tag{5.12}$$

The equation above can be solved for F_b. If F_b is interpreted as the result of buoyance, Eq. (5.12) can be used for calculating the density difference between the phases:

$$\Delta\rho = -\frac{\int_{\Gamma_f}(p_m + p_n + \sigma\kappa)\hat{n}\cdot\boldsymbol{e}_x dA = 0}{g\int_{\Gamma_f} x\hat{n}\cdot\boldsymbol{e}_x dA = 0} \tag{5.13}$$

5.3 GANGLION TRAPPED IN SNAP-OFF GEOMETRY

Unlike the microchannel in the previous problem, the geometry shown in Figure 5.3 provides an obstacle for trapping non-wetting phase analogous to the ones observed in the pore spaces of real permeable rocks. As presented in Section 2.2.1, geometries with variable flow cross-section, such as the one considered here, are associated to trapping by snap-off, which is the mechanism responsible for most of the residual oil in typical reservoirs.

It should be noted that, although actual trapping is invariably a three-dimensional phenomenon, its underlying physics can be modeled in two-dimensions. In fact, the flow geometry of Figure 5.4 resembles the micromodels traditionally used for studying residual oil. The work of (Lenormand et al. 1982) demonstrates that trapping and mobilization of ganglia in quasi-two-dimensional micromodels occur by the same mechanisms as in natural porous media. In our case, however, these mechanisms will be affected by the magnetic pressures in a way that cannot be predicted analytically.

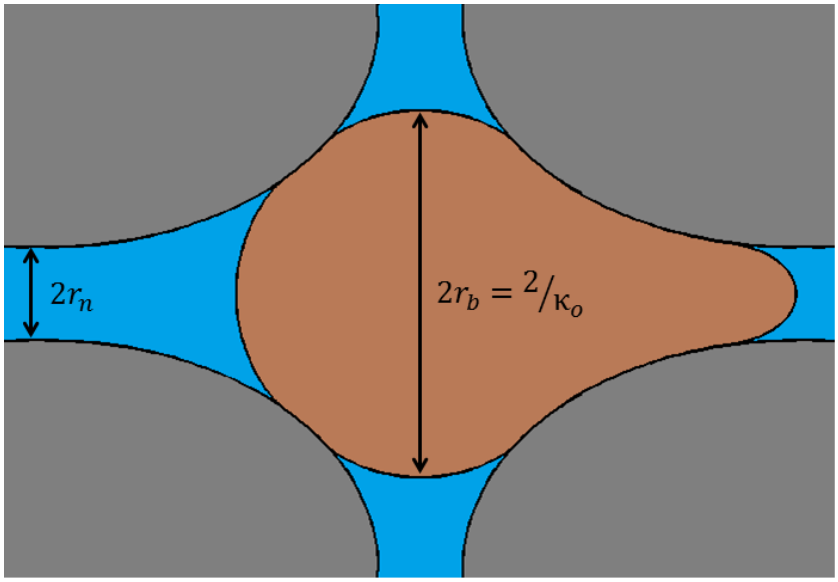

Figure 5.4 – Ganglion trapped in snap-off geometry. The ganglion interfaces are in the configuration corresponding to the imminence of mobilization.

A flow field bypassing the trapping geometry creates a pressure difference across the ganglion favoring its displacement towards the small gap. The ganglion is kept stationary by the counteracting capillary pressure acting on the interface formed by confining geometry. The capillary number is defined with reference to the bulk velocity of the external flow U_{ext}.

The goal of this problem is manipulating the ferrofluid magnetization in a way to assist the mobilization of the trapped ganglion. From the discussion in Section 2.2.2, the mobilization of ganglia occurs in different regimes depending on the applied pressure. For a pressure gradient slightly above the critical, mobilization is relatively orderly and

the assumption of quasi-static interface motion holds. The critical pressure gradient, associated to a critical capillary number Ca_c, yields an ganglion in the imminence of being mobilized. In this critical ganglion configuration, the upstream interface is in imbibition threshold and the downstream interface is in drainage threshold.

The shape of the ganglion in Figure 5.4 corresponds to the critical configuration for the case without magnetic stresses. Defining the widths of the pore body and the pore neck as r_b and r_n, respectively, and the length of the chamber as ΔL, the critical pressure gradient can be easily calculated:

$$\nabla P_c = \Delta L \, \sigma \left(\frac{1}{r_n} - \frac{1}{r_b} \right) \tag{5.14}$$

In the presence of magnetic stresses, ∇P_c and thus Ca_c must be calculated numerically. The algorithm consists of obtaining iteratively the configuration with the maximum values of p^- and U_{ext} under which the ganglion interfaces remain stable. It involves simulation cycles in which one of these parameters is increased while the other is kept constant. In the end of each iteration, the stability of the resulting ganglion is assessed. The iteration procedure stops when both parameters can no longer be increased.

The interface stability condition classically used, $d\kappa/dS_{nw}$, states that curvature must vary in accordance to the ganglion volume (more details in Section 2.2). Provided that the magnetic stresses and the capillary pressure are comparable in magnitude, this condition can be extended to non-uniform curvatures by replacing κ with a spatial average.

It is desirable to generate magnetic stresses in a way that reduces ∇P_c compared to the value given by Eq. (5.14). Similar to the previous problems, simulations are carrier out with magnetic fields in both horizontal and vertical configurations. The results obtained for a single-pore can be generalized to macroscopic levels. In fact, as demonstrated in Section 2.3.2, the Ca_c values can be used for estimations of the capillary desaturation curve.

CHAPTER 6: Numerical Methods

Obtaining results with the pore-scale model presented in the previous chapter presents some difficulties from a numerical standpoint. The fluid interface deforms under the applied magnetic field and pressure gradient while adjusting to the geometry of the pore space. Moreover, both the magnetostatic and fluid dynamics problems need to be solved in an irregular and time-dependent domain. The former issue can be handled by the level set method, which is described in Section 6.1. The latter is tackled with the explicit-jump immersed interface method, which is the focus of Section 6.2.

6.1 Level Set Method

The level set method (LSM), introduced by (Osher and Sethian 1988), deals with the time evolution of interfaces described by level set functions. Vast literature on the method is available (Osher and Fedkiw 2002; Sethian 1999) illustrating its application in areas ranging from combustion to microfabrication. It provides a way of tracking the interface position implicitly instead of tracking the path of selected interface points in a Lagrangean fashion. According to this approach, the interface is embedded as the zero level of a level set function, i.e. the interface consists of a set of points $\vec{x} \in \vec{X}$ such that

$$\phi\left(\vec{X}, \tau\right) = 0 \tag{6.1}$$

where ϕ is the level set function and τ is a time-like parameter. This formulation presents some clear advantages. First, it does not involve discretizing the interface and thus it avoids the need for repeatedly adjusting the grid point locations according to the changes in the interface shape. Secondly, it easily handles topological changes of the interface, such as splitting and coalescence of multiple interfaces. However, these advantages come at the expense of using the entire domain to store an interface.

A sign convention can be defined for determining whether a point lies inside or outside the fluid interface. In this work, the negative level set values $\phi < 0$ stand for the interface interior. If the sign convention is obeyed and the level set function value at a point corresponds to the distance from this point to the interface, the level set function is said to be a sign distance function. It can be shown that $|\nabla\phi| = 1$ in the entire domain for sign distance functions.

The LSM approach presented here is based on (Prodanović and Bryant 2006), and simulates the quasi-static fluid interface motion in capillary-driven flows through pore-scale geometries. An extended version of this approach by (Ryoo et al. 2012) adds spatially constant magnetic interfacial pressures to the capillary pressure aiming to represent the effects of the presence of a ferrofluid phase.

Considering the initial value problem:

$$\phi_\tau + V_n|\nabla\phi| = 0 \tag{6.2}$$

where V_n is the level set velocity in a normal outward direction. We define V_n such that represents the imbalance between the forces acting on the interface. Therefore, the interface should move in a way to reduce V_n as the pseudo-time progresses until an equilibrium configuration is achieved. Given the dimensionless pressure balance from Eq. (5.9), the velocity V_n can be substituted to give

$$\phi_\tau + \left(\frac{p^-}{\sigma \kappa_o} - \frac{p^+}{\sigma \kappa_o} - \frac{\mu_o H^2}{2\sigma \kappa_o} \left[\chi + \chi^2 \left(\hat{n} \cdot \frac{\vec{H}}{H} \right)^2 \right] \right) |\nabla \phi| - \frac{\kappa}{\kappa_o} |\nabla \phi| = 0 \qquad (6.3)$$

This evolution equation displays terms of different mathematical nature. Its solution involves a combination of numerical techniques for hyperbolic and parabolic problems most of which are available as functions in the Toolbox of Level Set Method (Mitchell and Templeton 2005). Since it is dependent on the curvature, the term associated with the capillary pressure is treated as a diffusive and evaluated by central differencing. The remaining pressures appear as part of an advective term and hence require special treatment.

It can be verified that Eq. (6.3) without the curvature-dependent term is a special case of the Hamilton-Jacobi equation. This implies that the advective term must be spatially discretized with the same kind of upwinding technique traditionally employed when dealing with hyperbolic conservation laws, in which the derivatives are approximated by biased finite difference stencils that favor the propagation direction of

the characteristic information. For high order approximations, proper upwind discretizations are provided by the essentially non-oscillatory (ENO) and weighted ENO (WENO) methods. Details on the derivation of these methods can be found in (Osher and Fedkiw 2002).

Although the terms in Eq. (6.3) only make physical sense along the fluid interface, implementing the LSM requires ascribing values to the pressure terms in every grid points of the domain. The diffusive term depends only on the curvature, which can be obtained numerically from the first and second derivatives of the level set function at any grid point, even at points that lie on levels of the level set function other than the interface. Unfortunately, similar approach is not available to the pressures associated to the advective term.

In case that these advective pressures are constant along the interface, such as in (Rahmani et al. 2012), it is natural to consider all grid points having the same value regardless of their specific location. In the current case, however, it is desirable that the value adopted by each point reflects the information on how the magnetic and thermodynamic pressures vary along the interface. This is achieved with the velocity extension method by (Adalsteinsson and Sethian 1999) in which a velocity at a given point of the interface is propagated orthogonally from the interface using a fast marching method. This method ensures that the level set function deforms homogeneously everywhere in the domain.

Once the spatial terms of Eq. (6.3) are discretized, a third-order total variation diminishing (TVD) Runge Kutta method is used for advancing the level set function with respect to the pseudo-time. This method can be distinguished from others of the Runge Kutta class for preventing spurious oscillations at high-order approximations (Osher and Fedkiw 2002).

As indicated by the flow chart in Figure 6.1, whenever the largest accumulated displacement of the fluid interface is on the order of the grid spacing, the magnetic and pressure fields must be updated for the new problem geometry yielding new values for the pressure terms. The procedure of interface displacement and recalculation of pressure terms is repeated until V_n vanishes and equilibrium is reached. At the end of every time step, the condition $\phi(\vec{x}) \leq \psi(\vec{x})$, where $\psi(\vec{x})$ is the level set function representing the pore geometry walls, must be enforced. Pore space is represented by the negative values of $\psi(\vec{x})$. This strategy for accounting the effects of the wall presence naturally leads to zero contact angles (Prodanović and Bryant 2006).

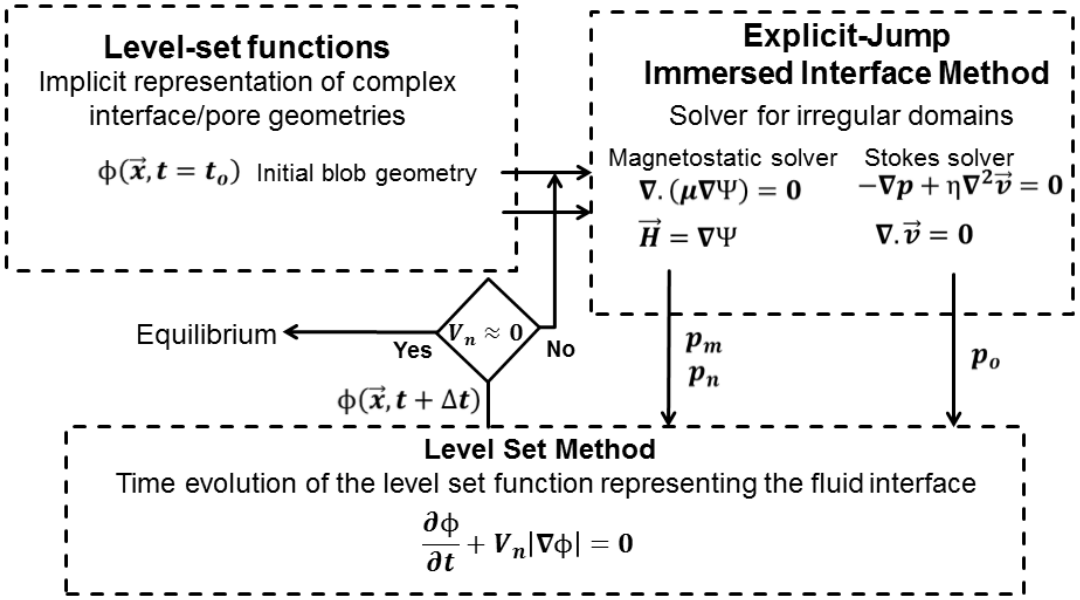

Figure 6.1 – Flow chart with the outline of the interface displacement algorithm.

Whenever the largest accumulated displacement of the fluid interface is on the order of the grid spacing, the magnetic and pressure fields must be updated. The procedure is repeated until equilibrium is achieved.

As the level set function is repeatedly subjected to the restriction of a wall with some potentially irregular shape, its propagation might not be completely homogenous. After some time steps, the level set function develops steep gradients in the regions where its zero level is close to the wall. The existence of these gradients is detrimental to the accuracy and stability of the method.

Reinitialization techniques aim to remove steep gradients by constructing a signed distance function from a given interface configuration. A popular reinitialization

approach involves using an equation with the form of Eq. (6.2) so that the same LSM solution framework can be applied:

$$\phi_\tau + sign(\phi_0)(|\nabla\phi| - 1) = 0 \tag{6.4}$$

when equilibrium is achieved and the time-derivate vanishes, the above expression is reduced to $|\nabla\phi| = 1$, which characterizes a signed distance function.

This approach has the downside of slightly displacing the zero level set from its original position. Considering that the method for solving the magnetostatic and fluid dynamics problems relies heavily on the information produced by the interface and its adjacent regions, even small undesirable displacements can affect the results substantially.

As noted by (Russo and Smereka 2000), the error was caused by the discretization near the interface not accounting for the information propagation direction correctly. The same work proposed a subcell fix in which the interface position is incorporated into the finite difference stencil. The fix was later generalized to higher-order discretization schemes by (Chéné et al. 2008). Combining WENO with the subcell fix tends to alleviate the noise introduced in the curvature field by the reinitialization procedure.

Another significant improvement of the LSM is achieved by restricting the solution domain to a narrow band around the interface (Peng et al. 1999). The localized LSM can be implemented by multiplying the velocity V_n by a cut-off function:

$$c(\phi) = \begin{cases} 1 & |\phi| \leq \beta \\ \frac{(|\phi|-\gamma)^2(2|\phi|+\gamma-3\beta)}{(\gamma-\beta)^3} & \beta < |\phi| \leq \gamma \\ 0 & |\phi| > \gamma \end{cases} \tag{6.5}$$

The width of the band is defined by the parameters $0 < \beta < \gamma$. This width should be large enough to accommodate the number of grid points necessary for the spatial discretization chosen. The interval between γ and β serves to smooth the cut-off function and thus prevent oscillations at the band boundary. In order to preserve numerical accuracy, the localized LSM must be combined with a reinitialization technique.

6.1.2 Conservation of Volume

Given the assumption of incompressibility, the equilibrium interface must enclose the same volume of non-wetting phase as the initial one for the problems described in Sections 5.1 and 5.2. However, conservation of volume is not guaranteed in the LSM if not properly enforced. In these two problems, the pressure inside the non-wetting phase p^- should be calculated so that the interface equilibrium is satisfied in an integral sense at every time step:

$$p^- = \frac{\sigma\kappa_o}{L_f}\int_{\Gamma_f}\left\{\frac{p^+}{\sigma\kappa_o} + \frac{\mu_o H^2}{2\sigma\kappa_o}\left[\chi + \chi^2\left(\hat{n}\cdot\frac{\vec{H}}{H}\right)^2\right] + \frac{\kappa}{\kappa_o}\right\} dS \tag{6.6}$$

where L_f is the length of the liquid interface (assuming a two-dimensional problem). In the case of the moving droplet in Section 5.2, the body force $\overrightarrow{F_b}$ has also to be added to the integral on the right-hand side.

This approach offers a relatively simple way to overcome the difficulties in imposing volume conservation with the level set method. Nevertheless, it should be noted that only the zero level set interior has its volume preserved. The pressure p^- calculated accounts for the effects of the capillary pressure on the interface and thus involves curvatures evaluated at the zero level set. The curvatures at grid points lying on positive and negative level sets are smaller and greater, respectively, than the curvatures of their orthogonal projections on the interface. Consequently, level set gradients decrease near the interface as the simulation progresses and the level set function tends to lose its distance function property if reinitialization is not used.

One alternative numerical formulation is including the capillary pressure as part of the advective term and propagating the values obtained on the interface to the entire computational domain using the velocity extension technique. Notwithstanding the advantage of ensuring constant distance between the level sets throughout the simulation, attempts of employing this approach indicate that purely advective motion is very prone to instabilities and shock solutions after few time steps (LeVeque 1992). The dissipation introduced by the diffusive term has a strong and indispensable stabilizing effect to the solution.

6.2 IMMERSED INTERFACE METHOD

As briefly discussed in the previous chapter, by defining the regions of uniform permeability Ω^+ and Ω^-, the magnetostatic formulation of Eq. (3.16) is reduced to the

Laplace Eq. (5.4). If ψ^+ and ψ^- are the magnetic potential functions inside and outside the ferrofluid, respectively, the equations $\nabla^2\psi^+ = 0$ and $\nabla^2\psi^- = 0$ could be solved separately on each of the domains, provided the solution fields and its derivatives at the interface satisfy the conditions dictated by Eq. (5.5). Hence, the interface of magnetic permeability contrast acts as an "internal boundary condition" to the solution of these equations.

Defining a different computational mesh on each domain is excessively complicated because the interface is irregular and dynamically changes thus requiring constant remeshing. Another possibility is using a regular mesh and a Heaviside function to smooth the interface discontinuity (e.g. Sussman et al 1994 for a discontinuous density). This approach is simple but yields low accuracy near the interface, which is the most important solution area for our application.

The immersed interface method (IIM) deals with the notion of "internal boundary conditions" directly. In addition to a mathematically rigorous treatment of the interface and second-order accuracy, the IIM presents good compatibility with the level set formulation. In fact, the same regular grid used for defining numerically the level set function can be used for the method.

Although there are different versions of the IIM, the method generally consists of using some finite-difference-based discretization and a non-conforming grid to solve problems in irregular domains. Its implementation involves dividing the computational grid points into two categories: regular and irregular. Regular points have all their neighboring points in the same magnetic medium. Irregular points have at least one of its

neighbors on the opposite site of the interface. Simple central finite difference can be used for the regular points as the Taylor expansion terms are continuous throughout the stencil. In the case of an irregular point, the discretized equation is obtained by a modified Taylor expansion that incorporates jump conditions, i.e. the magnitude of the discontinuities in the solution field and its derivatives across interface.

A particularly efficient class of IIM is the explicit-jump immersed interface method (EJIMM) introduced by (Wiegman and Bube 2000). The mathematical foundation of this method comes from a lemma for the Taylor expansion near a discontinuity. Considering a discontinuity at the position $x = 0$ between two grid points arbitrarily located at $x = h^-$ and $x = h^+$ in a one-dimensional space:

$$\left|\psi(h^+) - \sum_{k=0}^{l} \frac{h^k}{k!}\psi^{(k)}(h^-) - \sum_{k=0}^{l} \frac{(h^+)^k}{k!}\left[\psi^{(k)}\right]\right| \leq O(h^{l+1}) \tag{6.7}$$

where the grid spacing h satisfies $h^+ = h^- + h$ and the notation $[\psi]$ stands for $\psi^+ - \psi^-$. The discretized equations for irregular points can be derived from the lemma above. For instance, the discretized Laplace equation at the point x_j near a discontinuity with position $x = \alpha$, such that $x_j < \alpha < x_{j+1}$, is given by

$$\psi_{xx}(x_j) \approx \frac{\psi(x_{j+1}) - 2\psi(x_j) + \psi(x_{j-1})}{h^2} - \frac{1}{h^2}\sum_{m=0}^{2} \frac{(x_{j+1} - \alpha)^m}{m!}\left[\psi^{(m)}\right] \tag{6.8}$$

The great advantage of the EJIMM is that fact that it leads to an algebraic system with the exact same form as the Poisson problem in a regular domain, because all the

information regarding the interface discontinuities lies on the right-hand side of the system. It means that the EIJMM is compatible with fast Poisson solvers, such as the FFT solver (Swarztrauber 1977).

Considering a discontinuity interface $\boldsymbol{\Gamma}(s)$ parametrized by arc length $|\boldsymbol{\Gamma}'(s)| = 1$ with curvature given by $\kappa(s)$. For Laplace problems in general, the following jump conditions apply:

$$[\psi] = \omega$$

$$[\psi_{\hat{t}}] = \frac{d\omega}{ds}$$

$$[\psi_{\hat{n}}] = \nu$$

$$[\psi_{\hat{t}\hat{t}}] = \frac{d^2\omega}{ds^2} + \kappa\nu$$

$$[\psi_{\hat{t}\hat{n}}] = \frac{d\nu}{ds} - \kappa\frac{d\omega}{ds}$$

$$[\psi_{\hat{n}\hat{n}}] = -\frac{d^2\omega}{ds^2} - \kappa\nu \tag{6.9}$$

where $\hat{n}$ and $\hat{t}$ represent the normal and tangential directions of the interface, respectively. In the specific case of the magnetostatic problem, $\omega = 0$, $\nu = H_n^+(1 - \mu^+/\mu^-)$ and $\boldsymbol{\Gamma}$ corresponds to the interface of magnetic permeability contrast. Provided that a ν guess exist for all the points at which the interface of magnetic permeability contrast intercepts the grid lines, the jump conditions above can be substituted into the

discretized system. The system is then solved with a fast Poisson solver and the residue $H_n^+\mu^+ - H_n^-\mu^-$ is evaluated. Because of the linearity of the problem, the residue vector is a linear combination of the ν guesses. Therefore, the correct ν values can be obtained iteratively by a linear solver, such as the generalized minimal residual method (GMRES). In this case, each GMRES iteration corresponds to the solution of a Poisson problem.

An extension of the EJIMM for solving the Stokes flow of Eq. (5.2) was proposed by (LeVeque and Li 1997). This first version of the method employed a single grid for both pressure and velocity. Later versions adopted the staggered marker-and-cell (MAC) grid, which is better for ensuring that the pressure and the velocity fields are couple. The method presented in (Tan et al. 2009) is able to handle irregular interfaces with imposed velocities, such as the ones described by the boundary conditions of Eq. (5.3).

The jump conditions for the fluid dynamics problem are function of a force $\vec{f}$ defined at the points where the interfaces with imposed velocities intercept the grid lines

$$
\begin{aligned}
[\vec{u}] &= 0 & [p] &= \left(\vec{f}\cdot\hat{n}\right)\\
[\vec{u}_{\hat{t}}] &= 0 & [p_{\hat{t}}] &= \frac{d\left(\vec{f}\cdot\hat{n}\right)}{ds}\\
[\vec{u}_{\hat{n}}] &= -\frac{1}{\eta}\left(\vec{f}\cdot\hat{t}\right)\hat{t} & [p_{\hat{n}}] &= \frac{d\left(\vec{f}\cdot\hat{t}\right)}{ds}\\
[\vec{u}_{\hat{t}\hat{t}}] &= -\frac{1}{\eta}\kappa\left(\vec{f}\cdot\hat{t}\right)\hat{t} & & \\
[\vec{u}_{\hat{t}\hat{n}}] &= -\frac{1}{\eta}\frac{d\left(\vec{f}\cdot\hat{t}\right)}{ds}\hat{t} + \frac{\kappa\left(\vec{f}\cdot\hat{t}\right)}{\eta}\hat{n} & [p_{\hat{t}\hat{t}}] &= \frac{d^2\left(\vec{f}\cdot\hat{n}\right)}{ds^2} + \kappa[p_{\hat{n}}]\\
& & [p_{\hat{t}\hat{n}}] &= \frac{d^2\left(\vec{f}\cdot\hat{t}\right)}{ds^2} - \kappa[p_{\hat{t}}]
\end{aligned}
\tag{6.10}
$$

$$[\vec{u}_{\hat{n}\hat{n}}] = -[\vec{u}_{\hat{t}\hat{t}}] + \frac{[p_{\hat{n}}]}{\eta}\hat{n} + \frac{[p_{\hat{t}}]}{\eta}\hat{t} \qquad\qquad [p_{\hat{n}\hat{n}}] = -[p_{\hat{t}\hat{t}}]$$

where η is the viscosity. The solution principle is completely analogous to one of the magnetostatic problem: a GMRES solver is used to iteratively calculate the set of $\vec{f}$ values that yields the desired velocities.

The iterations involve greater computational effort in this case than in the previous because there are two velocity components and a pressure field must be calculated. Given the operators Δ_h, ∇_h and div_h corresponding to the finite difference discretization of the Laplacian, gradient and divergence, respectively, the algebraic system representing the Stokes flow discretization is

$$\begin{bmatrix} \Delta_h & \nabla_h \\ div_h & 0 \end{bmatrix} \begin{bmatrix} U \\ P \end{bmatrix} = \begin{bmatrix} C_1 \\ C_2 \end{bmatrix} \tag{6.11}$$

where U and P are the velocity and pressure values, respectively, at the MAC grid points. The correction terms C_1 and C_2 on the right-hand side contains the information regarding the jump conditions.

For improving speed, the system (6.11) can be reduced by its Schur complement and turned into two Poisson problems to be solved sequentially:

$$(div_h \Delta_h^{-1} \nabla_h) P = \eta C_2 + div_h \Delta_h^{-1} C_1 \tag{6.12}$$

$$\eta \Delta_h U = C_1 - \nabla_h P \tag{6.13}$$

Each of the above systems can be solved with a fast Poisson solver.

CHAPTER 7: Results and Discussion

7.1 BLOB DETACHMENT FROM PORE SURFACES

The blob detachment study presented here was first published in (Soares et al. 2014) and represents a special case of a more general simulation approach presented in the current work. For this problem, the quasi-static immiscible displacements is completely controlled by the capillary and magnetic forces, meaning that the capillary number is very small and the magnetic Bond number has some appreciable value.

The situations portrayed in Figures 7.1(a) and (b) involve the same initial blob dimensionless volume $V' = \pi$ and straight tube geometry, but the magnetic field is oriented horizontally in Figure 7.1(a) and vertically in Figure 7.1(b) (two extreme orientation possibilities). The images depict completely different behaviors: whereas the horizontal field stimulates blob stretching and detachment from the walls, the vertical field induces small interface displacements and tends to increase the contact length slightly.

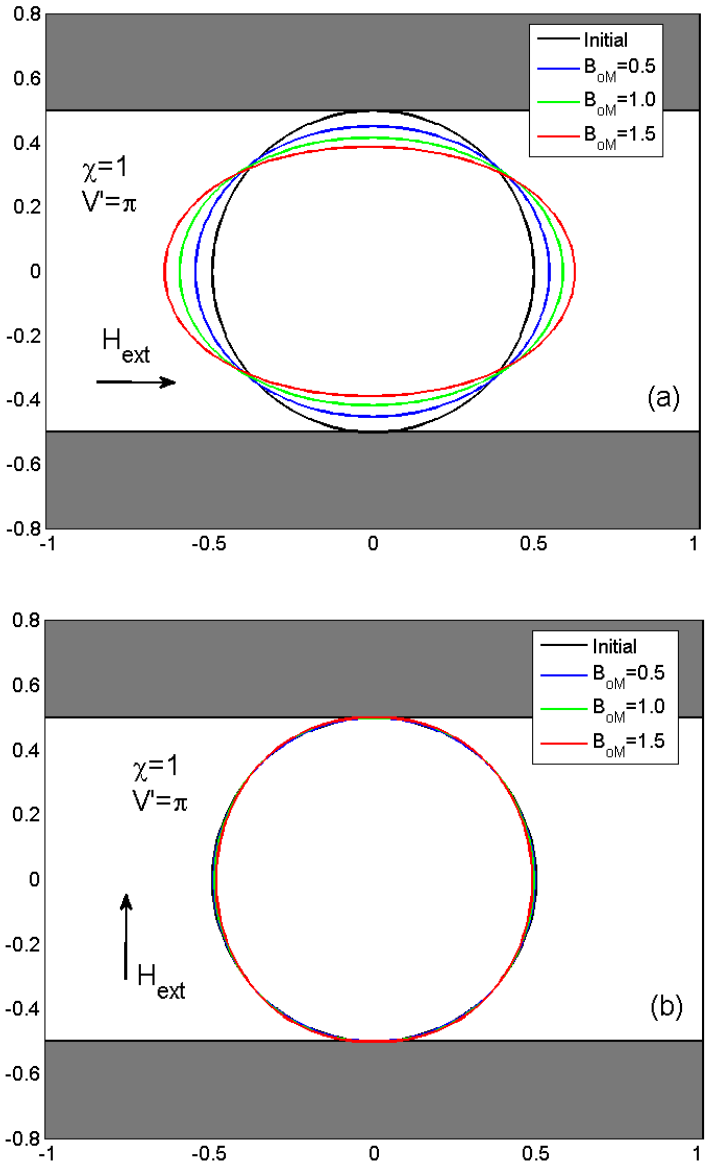

Figure 7.1 - Effect of magnetic field relative orientation. The horizontal field in (a) causes blob detachment and large interface displacements. The vertical field in (b) has very little effect on the interface configuration and slightly increases the contacts between the blob and the pore wall. The blob has the same initial shape in both cases.

Analyzing the stress distribution along the interface in each case helps to explain the reasons for such contrasting results. The initial distribution under a horizontal field is shown in Figure 7.2(a). In this plot, the constant capillary pressure reflects the constant curvature of the initial circular blob. The pressure sum, defined as the summation of all stresses displayed, is equivalent to the normalized thermodynamic pressure difference $(p^- - p^+)/\sigma\kappa_o$ according to the Eq. (5.9). Considering that $Ca \approx 0$, the pressure difference must be uniform along the fluid interface. This condition is achieved by the equilibrium configuration shown in Figure 7.2(b), in which the interface flattens out in the regions where the pressure sum was originally high and it expands in the other regions.

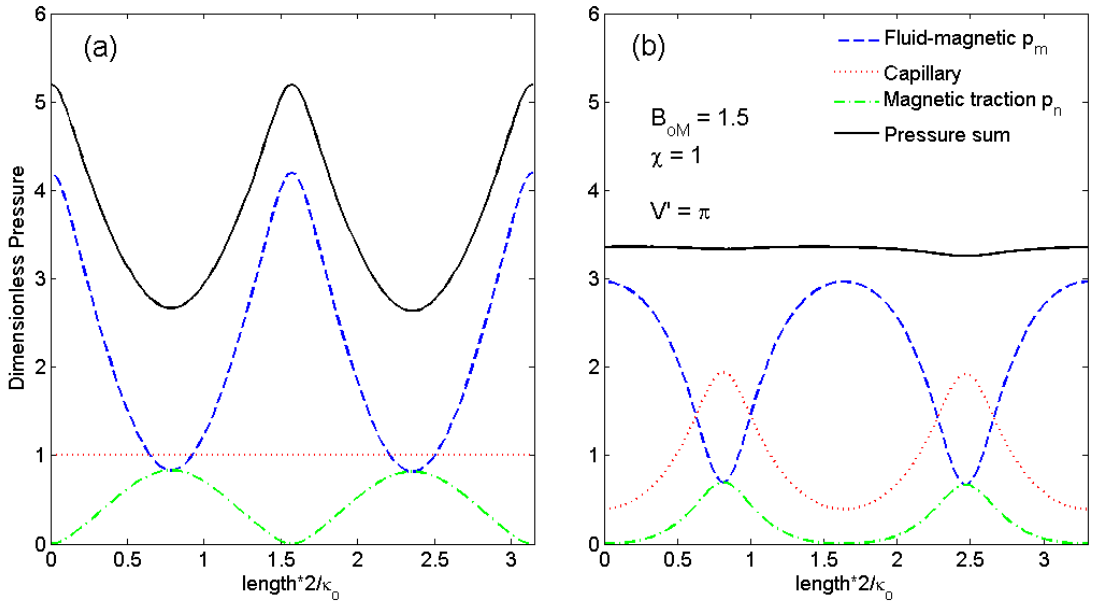

Figure 7.2–Pressure distribution along the interface under a horizontal field (corresponding to Figure 7.1(a). Length is measured from highest interface point counterclockwise. In the initial configuration (a), the pressure sum peaks at the pore wall contact point because of the high fluid-magnetic pressure. In the equilibrium (b), interface flattens out in the wall region and expands at the tube center.

For the vertical field case, the initial magnetic pressures shown in Figure 7.3(a) are both much lesser than the capillary pressure. Hence, interface displacements are expected to be small. It is observed in Figure 7.3(b) that, once again, the equilibrium interface flattens and expands in order to accommodate regions of high and small magnetic pressures, respectively. However, in this case, the interface expansion occurs

near the wall, increasing the contact length. The interface segments attached to the pore wall appear as regions of zero pressure sum because of the zero curvature of the wall and the absence of the magnetic pressures produced by the ferrofluid, i.e. fluid/ferrofluid interface is locally disconnected.

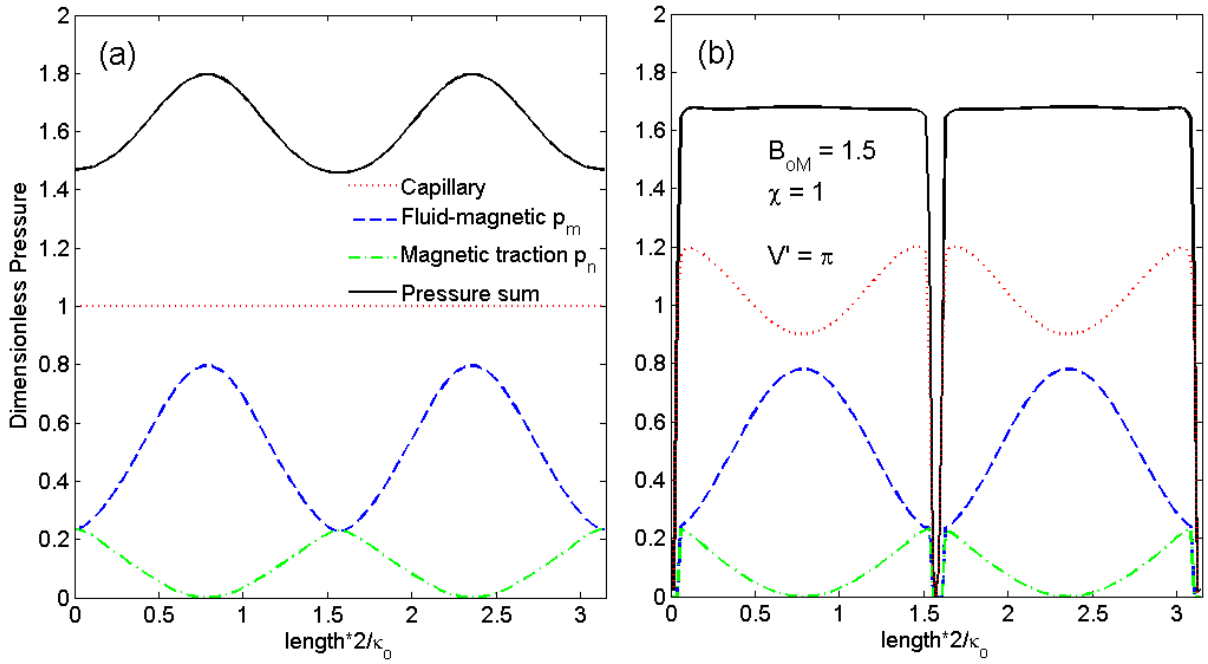

Figure 7.3 - Pressure distribution along the interface under a vertical field (corresponding to Figure 7.1(b). Length is measured from highest interface point counterclockwise. In the initial configuration (a), capillary pressure exceeds both magnetic components and the pressure sum is nearly constant. The equilibrium configuration (b) has the interface flattening slightly at the tube center and the appearance of regions of zero pressure where the blob touches the pore wall.

The cause of p_m being the predominant magnetic pressure in both cases is linked to magnetic field intensity distribution. It can be observed in Figure 7.4(a), for the horizontal external field case, that the initial magnetic field has a moderate strength at the tube center and it increases sharply in the pore wall contact region. As the blob detaches to reach equilibrium, the field strength in the wall region decreases slightly but remains a maximum, as shown in Figure 7.4(b).

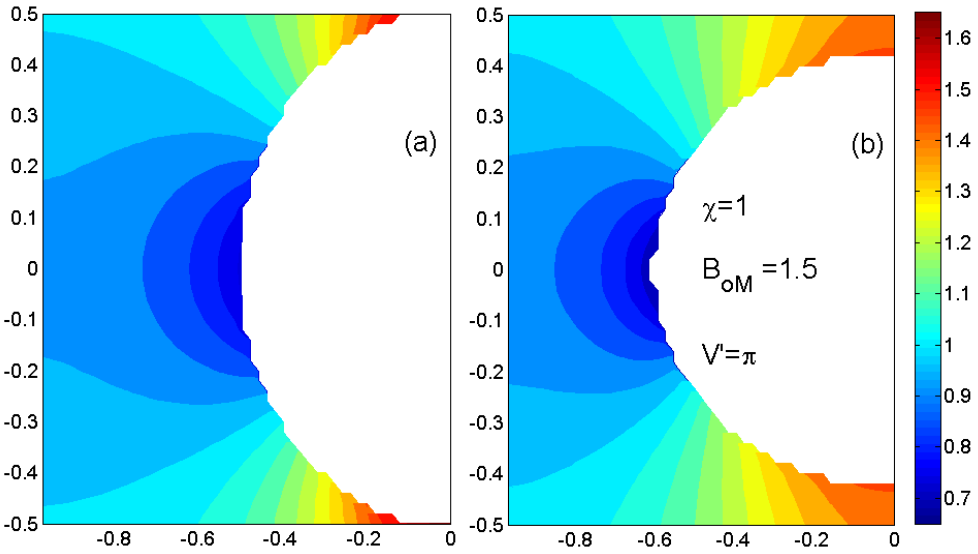

Figure 7.4 - Magnetic field strength distribution under a horizontal field. The field with the initial interface configuration (a) increases sharply from the tube center to the contact points. With the equilibrium configuration (b), the regions where the detached interface is close to the pore wall are near the field strength maximum, but field strength decreases slightly.

The initial magnetic field distribution when the external field is vertical presents the opposite behavior: Figure 7.5(a) shows that the strength in the vicinity of the interface at the tube center is similar to that of the horizontal external field case, but it decreases towards the wall. From the definition of the magnetic pressures in Eqs. (4.20) and (5.8), p_m is directly related to magnetic field intensity, while p_n depends also on the alignment of the field with the interface normal direction. In both cases considered, the greatest alignment occurs in the region with the smallest intensity, thus p_n is always smaller than p_m for the tube geometry.

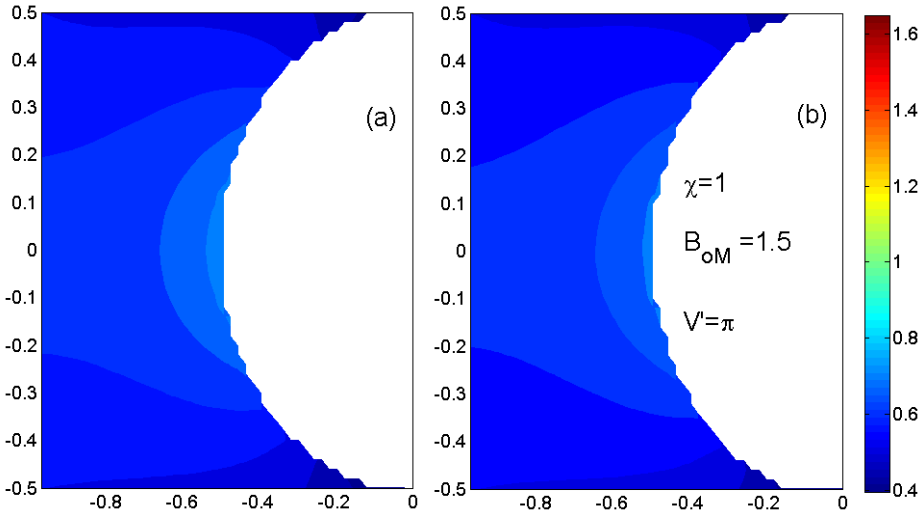

Figure 7.5 - Magnetic field strength distribution under a vertical field. The field with the initial interface configuration (a) has a moderate strength at the tube center and decreases slightly near the contact points. As the equilibrium configuration (b) is very similar, the field distribution does not present significant qualitative differences.

In more complex geometries, blob detachment is also likely to occur under horizontal fields, as exemplified by the low aspect ratio sinusoidal pore space shown in Figure 7.6.

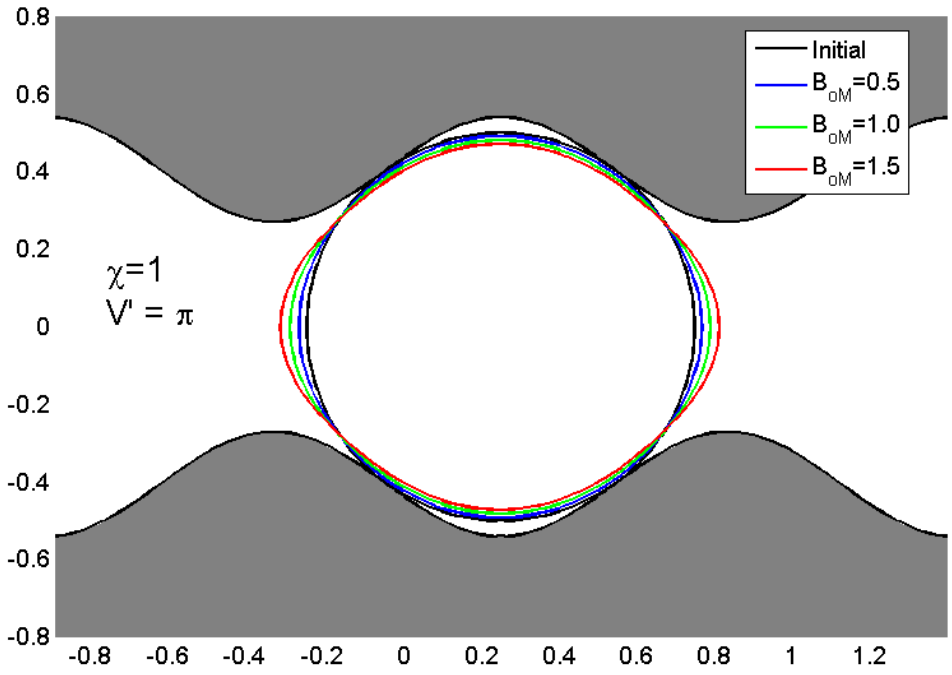

Figure 7.6 - Detachment of a blob trapped in a pore space with low aspect ratio under a horizontal field. Increasing $\boldsymbol{B_{oM}}$ leads to greater distances between the blob interface and the pore wall.

The interface stress distribution suggests the same mechanism is acting to cause blob detachment. The horizontally-oriented external field induces amplified field strengths near the pore wall contact region, represented by the four p_m peaks in Figure 7.7(a). The

equilibrium capillary pressure in Figure 7.7(b) is mostly influenced by the p_m amplitude. Once again, increasing magnetic stresses and thus B_{oM} leads to greater distances between the blob interface and the wall.

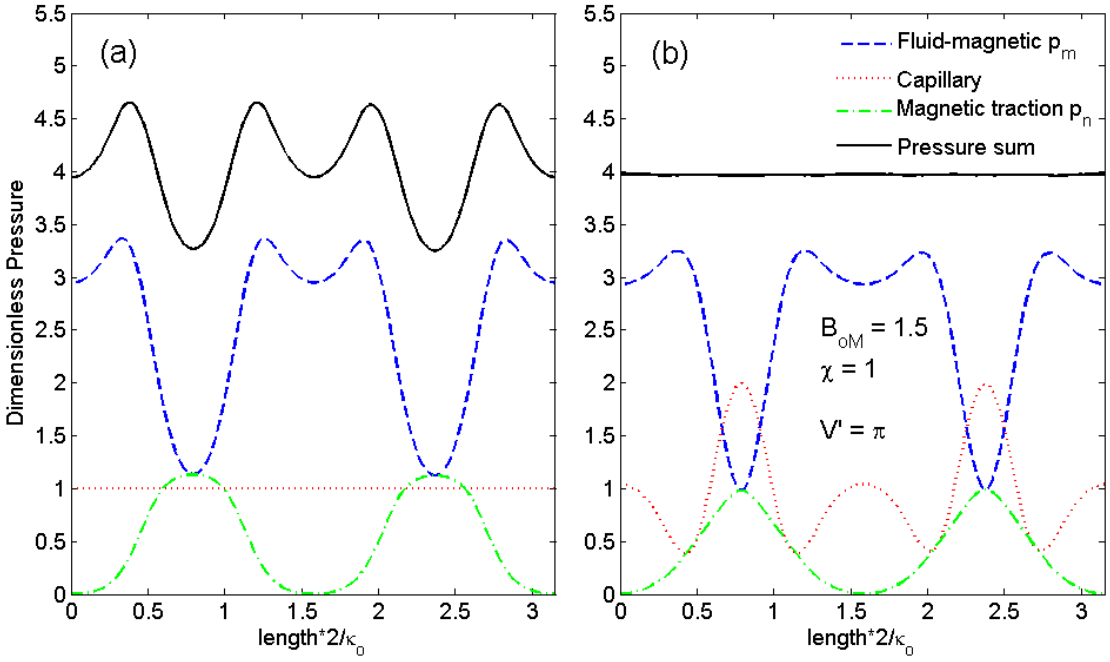

Figure 7.7 — Pressure distribution along the interface under a horizontal field in a low-aspect ratio pore geometry. Length is measured from highest interface point counterclockwise. In the initial configuration (a), the fluid-magnetic pressure peaks correspond to the contact points between the pore wall and the blob interface. The equilibrium configuration (b) presents small changes in the magnetic pressures, but the interface flattens in the contact regions and expands through the pore throats.

Variable pore cross-section seems not to be necessarily detrimental to the detachment of a nonwetting phase because this process depends more on the specific configuration of the interface/wall contact region than the pore geometry as a whole. As discussed above, most of the interface displacement is due to the p_m distribution amplitude, which is enhanced by the presence of regions where the magnetic field intensity is amplified. The field intensity amplification (or reduction) is consequence of a perturbation of the magnetic field produced by the proximity of two interfaces of magnetic permeability contrast. It can be deduced that the local configuration of these interfaces and their orientations in relation to the magnetic field define the amplification magnitude. Considering that in both pore geometries, with zero contact angle, the blob interface at the contact line is parallel (or nearly-parallel in the sinusoidal geometry) to the field, the resulting amplifications must be at least comparable.

This assertion can be confirmed by simulating the detachment of large blobs in these two geometries. Considering a blob with dimensionless volume $V' = \pi + 2$, critical detachment conditions can be obtained by a sequence of simulations with B_{oM} increasing stepwise. Some relevant simulation steps are shown by the plots by Figure 7.8. In fact, detachment occurs under similar B_{oM} values in the two geometries.

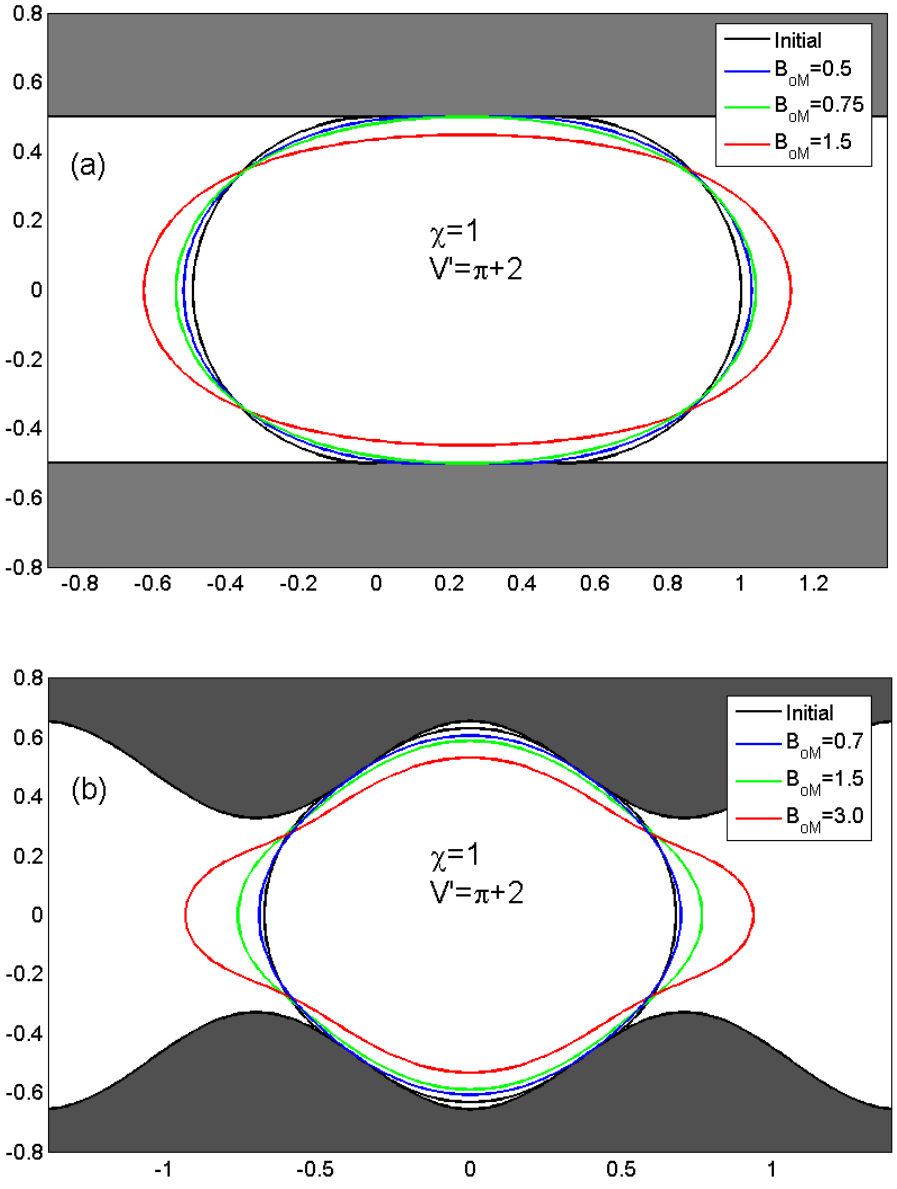

Figure 7.8 - Displacement of an oil blob with dimensionless volume $\boldsymbol{V' = \pi + 2}$ in different pore geometries. Detachment occurs approximately at $\boldsymbol{B_{oM} = 0.75}$ in the straight tube (a) and at $\boldsymbol{B_{oM} = 0.7}$ in the low-aspect ratio pore geometry (b).

It is interesting to notice that the post-detachment patterns obtained in Figure 7.8(a) resemble the classic elongated shape of ferrofluid droplets discussed by Berkovsky et al. (1993), even though the nature of the interface displacement is different when the ferrofluid is the wetting phase. As demonstrated by Rahmani et al. (2012) with an analytical model for the non-wetting ferrofluid case, the magnetic field is uniform in the nearly-ellipsoidal droplet and thus p_m is uniform along the interface. According to this analysis, the higher p_n at the droplet axis is responsible for its elongation towards the magnetic field direction. In the current case, elongation of the non-magnetic oil blob is produced by the contrast between the amplified p_m in the region between the blob and the tube wall and its smaller value at the blob axis. The p_n distribution plays a secondary role.

7.2 STEADY-STATE DROPLET MOTION IN MICROCHANNEL

In the previous problem, the equilibrium interface configuration reflects a balance between capillary and magnetic pressures solely. If the non-wetting phase is being driven by a body force $\overrightarrow{F_b} = F_b \boldsymbol{e}_x$ such that the velocity of the ferrofluid flow relative to the interface is considerable, viscous stresses emerge and affect the thermodynamic pressure distribution. Hence, the interface equilibrium is also influenced by and the non-uniform thermodynamic pressure distribution and the normal traction $F_b x$ associated to the

driving force. In this subsection, the combined effects of the magnetic, capillary and viscous forces on the liquid interface deformation are examined.

First, as a means of verifying the numerical approach developed for solving the Stokes flow, the equilibrium shape in the absence of magnetic pressures is calculated and compared with experimental data. In the experimental setup shown in Figure 7.9(a), a bubble ascends under the effect of buoyancy at steady-state configuration and with a low Reynolds number (Borhan and Pallinti 1995). This constitutes a scenario analogous to the simulation shown in Figure 7.9(b). A quantitative comparison of the results is not possible because the numerical model is two-dimensional. However, the magnetic and flow field distributions in a straight two-dimensional geometry display similar pattern to these in an axisymmetric tube, suggesting the results are qualitatively comparable. In fact, the figures show that the liquid interface behaves similarly in both cases, with a characteristic narrowing towards the advancing front.

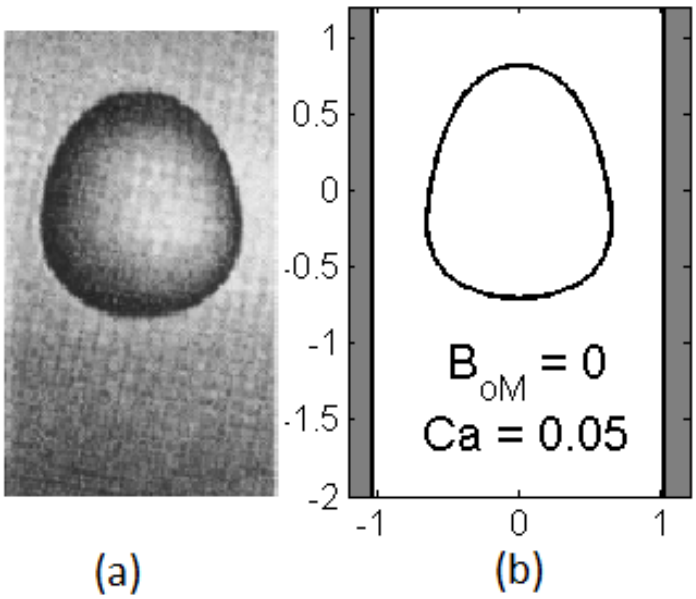

Figure 7.9 – Comparison between the experiment from Borhan and Pallinti 1995 involving a bubble ascending under the effect of buoyancy at steady-state configuration (a) and an equilibrium interface shape obtained with the numerical model simulated without magnetic pressures (b).

The shape of the moving droplet is explained by the equilibrium stress profile along the interface obtained with the numerical simulation. As observed in Figure 7.10, the thermodynamic pressure in the wetting ferrofluid varies sharply in the regions corresponding to the gaps between the droplet and the walls while it is relatively uniform in the other segments of the interface. This result is expected considering that large velocity gradients develop near the gaps and thus these areas have the highest viscous stresses of the flow domain. The force F_b is determined so that its associated normal

traction acting on the interface counteracts the overall effect of the thermodynamic pressure. Locally, however, there are imbalances between p^+ and $F_b x$ that need to be adjusted by the capillary force, justifying the prominent curvature variations observed in the equilibrium droplet interface. The pressure sum, which should be uniform for equilibrium, is numerically equivalent to the dimensionless non-wetting phase pressure $p^-/\sigma\kappa_o$.

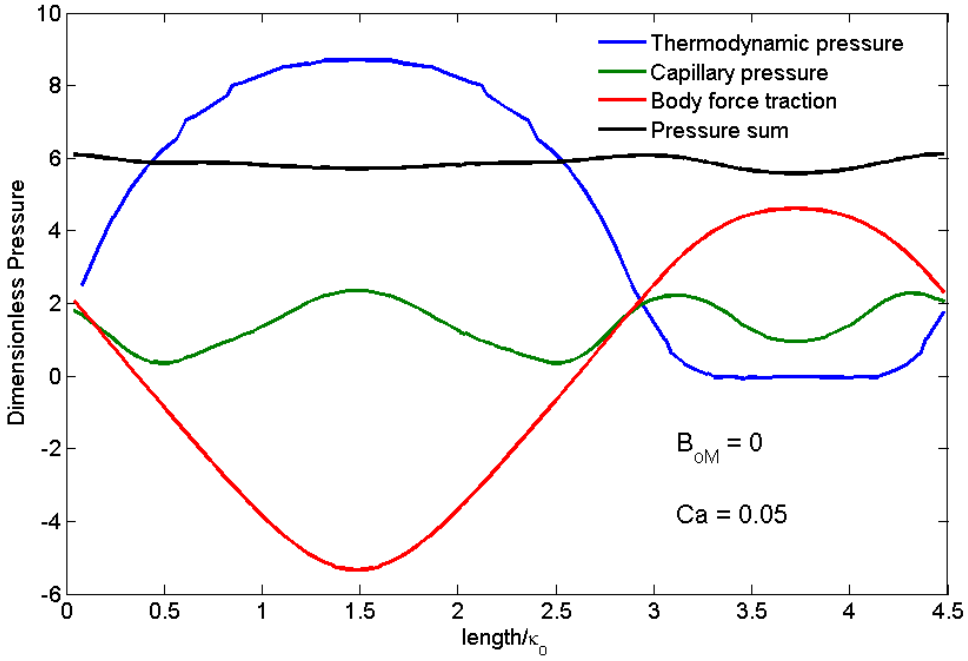

Figure 7.10 – Pressure distribution in the absence of a magnetic field. The interface normal traction associated to the force $\boldsymbol{F_b}$ counteracts the overall effect of the thermodynamic pressure while the capillary pressure adjusts to local imbalances.

Notwithstanding the droplet having its shape altered by the fluid flow, the conclusions drawn from the previous problem for the straight tube case regarding the magnetic field distribution are also valid for the current problem because the geometry remains essentially the same. The Figures 7.11(a) and (b) show equilibrium interfaces with different B_{oM} values and a constant Ca for horizontal and vertical magnetic field orientations, respectively.

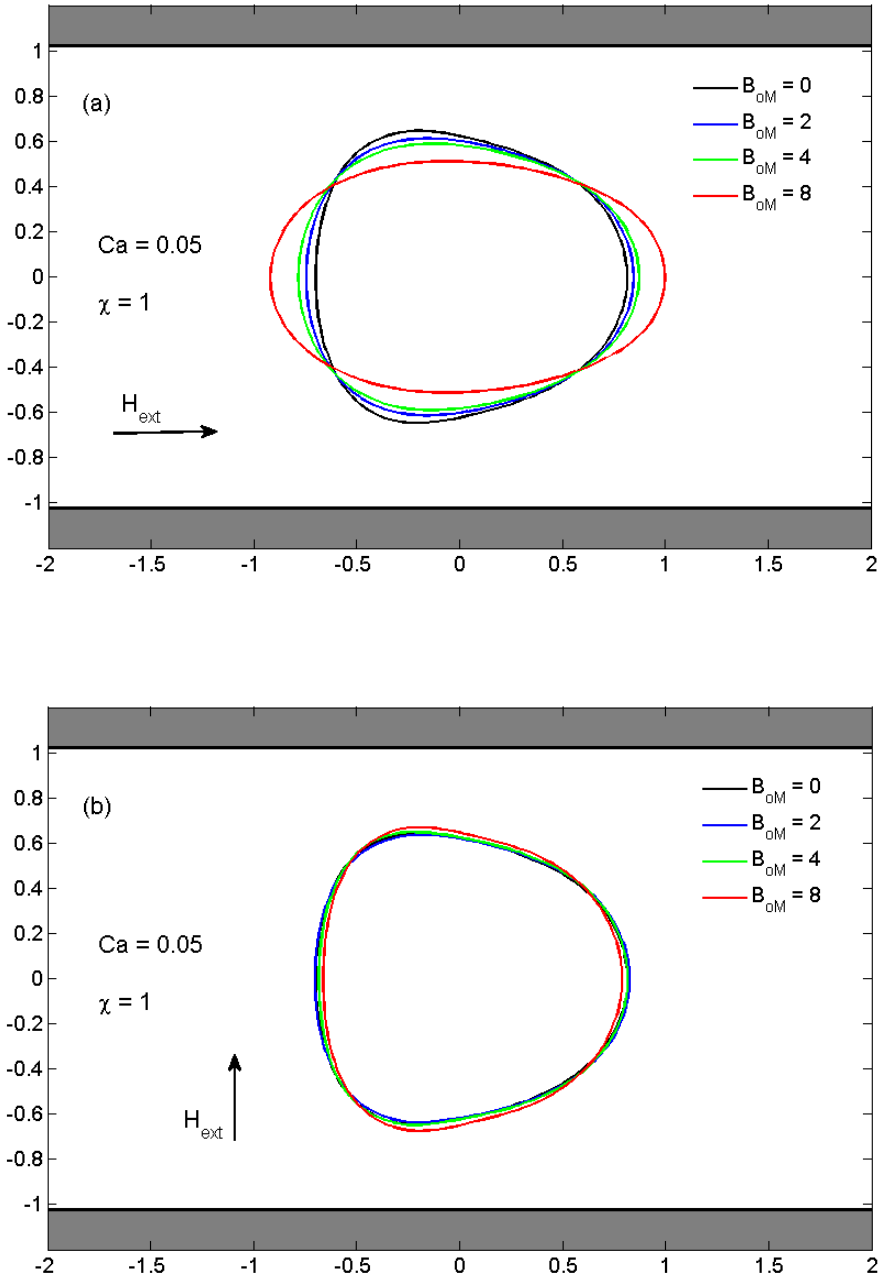

Figure 7.11—Effect of magnetic field relative orientation. The horizontal field in (a) causes a large droplet elongation towards the flow direction. The vertical field in (b) produces a subtle elongation perpendicular to the flow.

Not surprisingly, the horizontal field causes large elongations parallel to the flow direction while the vertical one causes insignificant elongations in the perpendicular direction. By the argument developed on the previous section, most of the interface displacement observed is driven by the p_m distribution and in turn by the local disturbances of the magnetic field intensity in the regions of proximity between interfaces of magnetic permeability contrast, (the liquid interface and the solid wall).

If the ferrofluid initial susceptibility χ is increased, these magnetic field disturbances become stronger. Consequently, the amplitude of p_m under a horizontal field is sufficient for inducing considerable interface displacements even for small B_{oM} values, as indicated by Figure 7.12(a). This result suggests that increasing the nanoparticles concentration in a ferrofluid can help compensate for small field intensities or large capillary pressures. On the other hand, increasing χ under a vertical field, as shown in Figure 7.12(b), seems to affect the interface displacement only slightly.

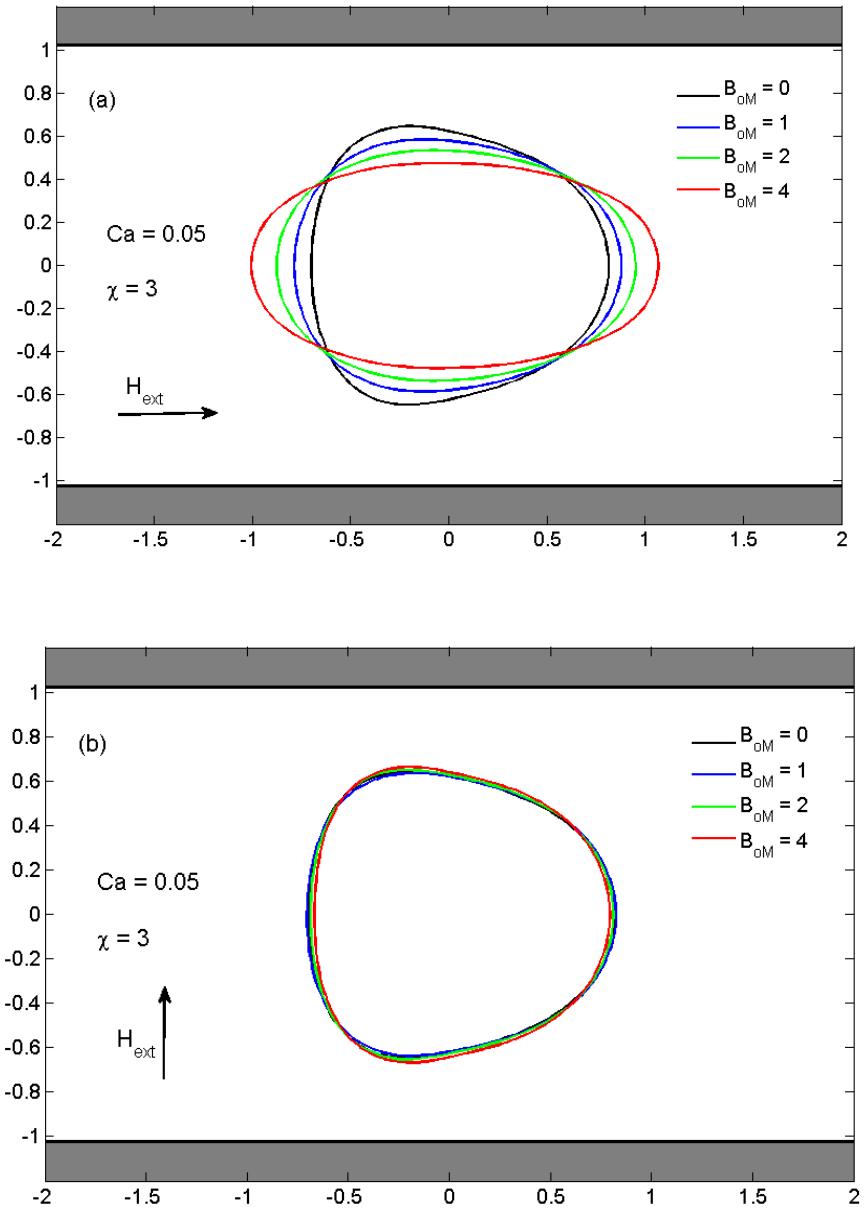

Figure 7.12-Effect of high ferrofluid susceptibility. The droplet presents large elongations under a horizontal field (a) for relatively small B_{oM} values. The vertical field remains not altering the equilibrium interface shape considerably (b).

The numerical results obtained for this problem have great significance for demonstrating how magnetic fields can be manipulated to improve the transport of some non-wetting liquid through a microchannel filled with ferrofluid. Provided that the field is oriented in parallel to the flow path, the distance between the liquid interface and the microchannel walls is increased and thus the velocity gradients and the associated viscous stresses are reduced. Ultimately, the droplet shaped under magnetic stresses is subjected to a smaller pressure drag. In fact, a comparison between Figures 7.13(a) and (b) demonstrates that the pressure decays less sharply across the elongated shape resulting from the horizontal field than it does for the droplet in the absence of a magnetic field.

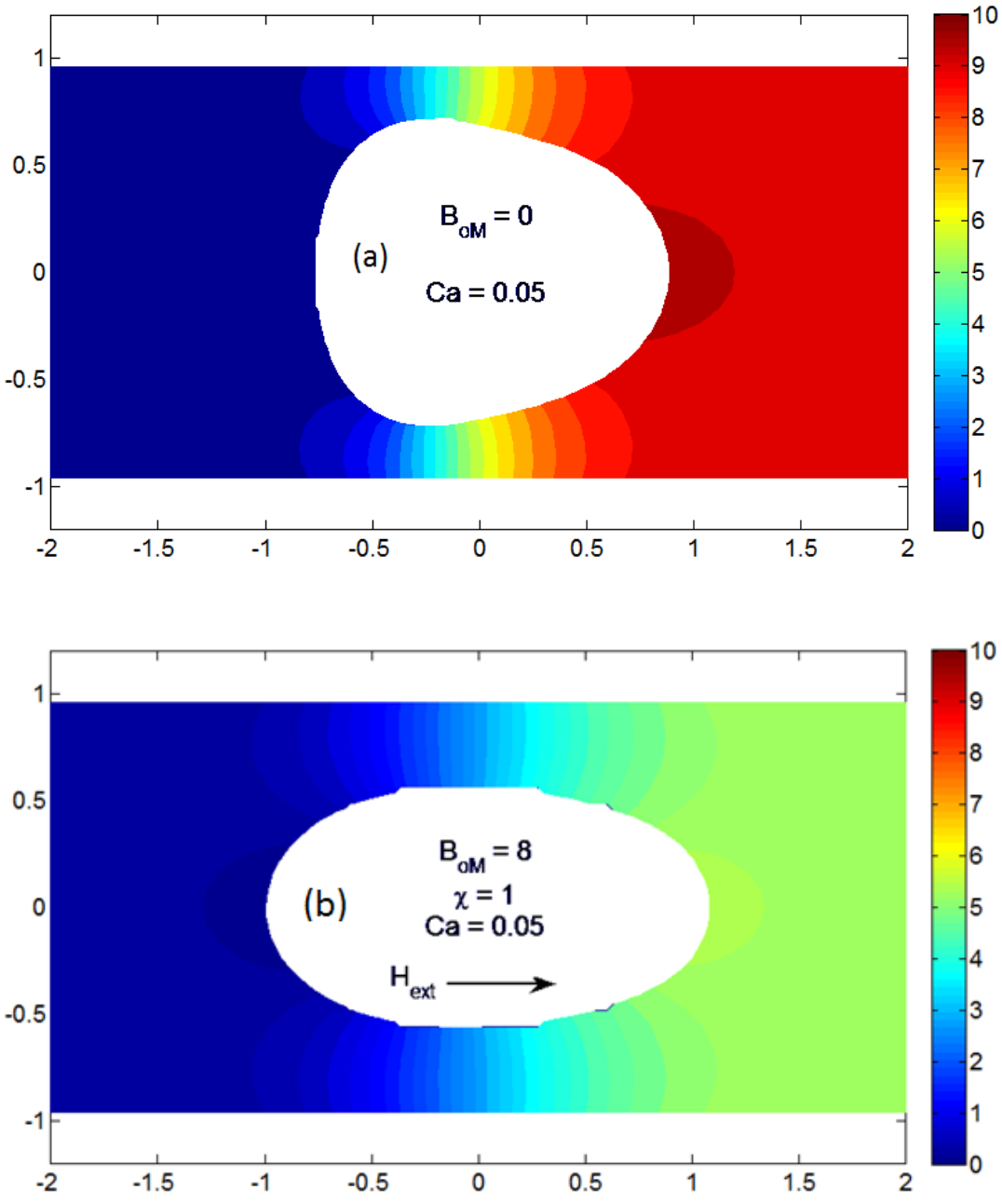

Figure 7.13—Effect of droplet elongation to the pressure distribution. In the absence of an external magnetic field (a), the pressure drop across the droplet is much greater than in the case of an applied horizontal field (b).

As argued in Section 5.2, the magnitude of the driving force $\overrightarrow{F_b}$ is a direct measure of the pressure drag acting on the droplet. It is desirable for delivery applications to reduce the $\left|\overrightarrow{F_b}\right|$ necessary for achieving a given Ca value. A series of simulations involving a constant Ca and a horizontal magnetic field exemplifies how increasing either B_{oM} or χ improves the droplet transportation. The results are summarized in Figure 7.14.

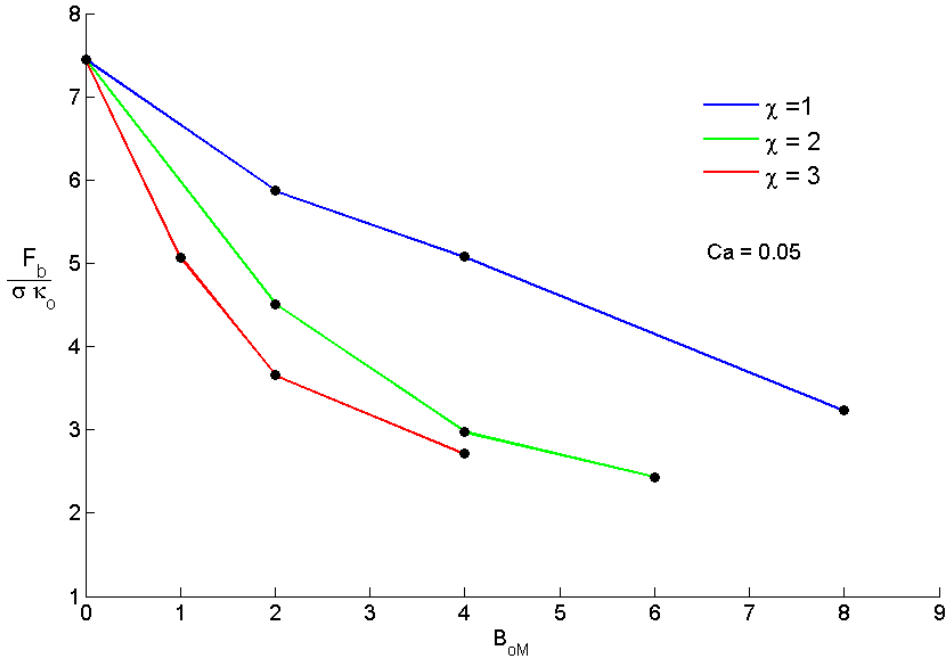

Figure 7.14 - Enhanced transport of non-wetting phase in a ferrofluid-filled microchannel. The driving force necessary for a droplet achieving a given velocity decays with both $\boldsymbol{B_{oM}}$ and $\boldsymbol{\chi}$ provided the magnetic field is parallel to the flow path.

7.3 GANGLION TRAPPED IN A PORE BODY

The goal of this problem is to evaluate the Ca value that leads to a ganglion at the imminence of mobilization (the critical capillary number Ca_c) for different magnetic field orientations in a pore body with a typical snap-off geometry. Achieving this goal involves running several simulations in incremental steps of non-wetting phase pressure p^- and flow bulk velocity U_{ext} while ensuring the resulting ganglion shape remains stable. The ganglion is said to be in its critical mobilization configuration when both p^- and U_{ext} can no longer be increased without a loss of stability (Section 5.3 for details). Results with good precision require small incremental steps and hence this is a time-consuming methodology.

In order to reduce the simulation times, it is advantageous to choose the initial guesses as the values corresponding to the case obtained in the absence of a magnetic field: p^-_o and $U_{ext,o}$. Naturally, both these values increase in the presence of magnetic pressures. The simulations were carried out with incremental steps of $0.1\,p^-_o$ and $0.02\,U_{ext,o}$.

As shown in Figure 7.15, the critical ganglion shape obtained varies considerably according to the magnetic field orientation. Although the geometry considered is more complex than the ones studied in Section 7.1, the displacement of the three-phase contact point follows the same pattern as in the blob detachment in a channel: the contact point advances towards the wetting phase for vertical field and recedes for the horizontal one.

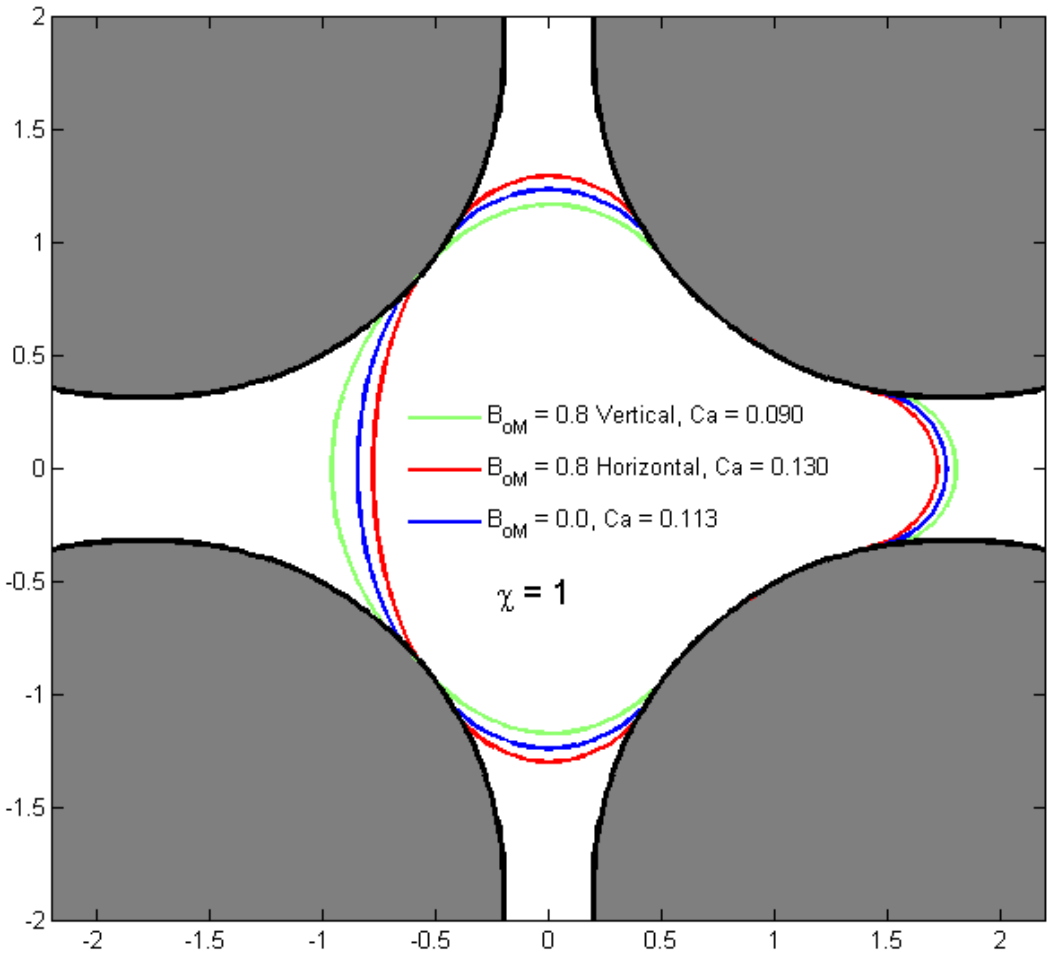

Figure 7.15— Critical ganglion interface shapes for different magnetic fields. The critical capillary numbers obtained indicate that the vertical field favors mobilization while the horizontal has a detrimental effect.

This result further confirms the assertion made in Section 7.1 that the magnetic stresses at the three-phase contact region are determined by the orientation of the solid and liquid interfaces relative to the external field rather than by the pore geometry as a whole. This has an important implication since the trapped ganglion mobilization requires the

movement of the contact line, which could be significantly influenced by the locally focused effect of the magnetic field.

Far more important than altering the ganglion equilibrium shape, the magnetic pressures have a strong impact on the Ca_c value. The results displayed in Figure 7.15 indicate that the vertical field favors mobilization while the horizontal has a detrimental effect. Such disparity is not caused by the flow field being affected by changes in the critical shape of the interfaces, as the pressure is essentially uniform on each interface in both magnetic field orientations.

The reason for the differences in Ca_c is related to the magnetic pressure profiles, shown in Figure 7.16 for the upstream and downstream interfaces. The pore neck, where the downstream interface is located, is geometrically similar to the straight tube in this example. This explains why the magnetic pressure profiles in this region obey the same pattern as in Figures 7.2 and 7.3: high p_m and low $p_n$at the interface center for the vertical field and the inverse for the horizontal.

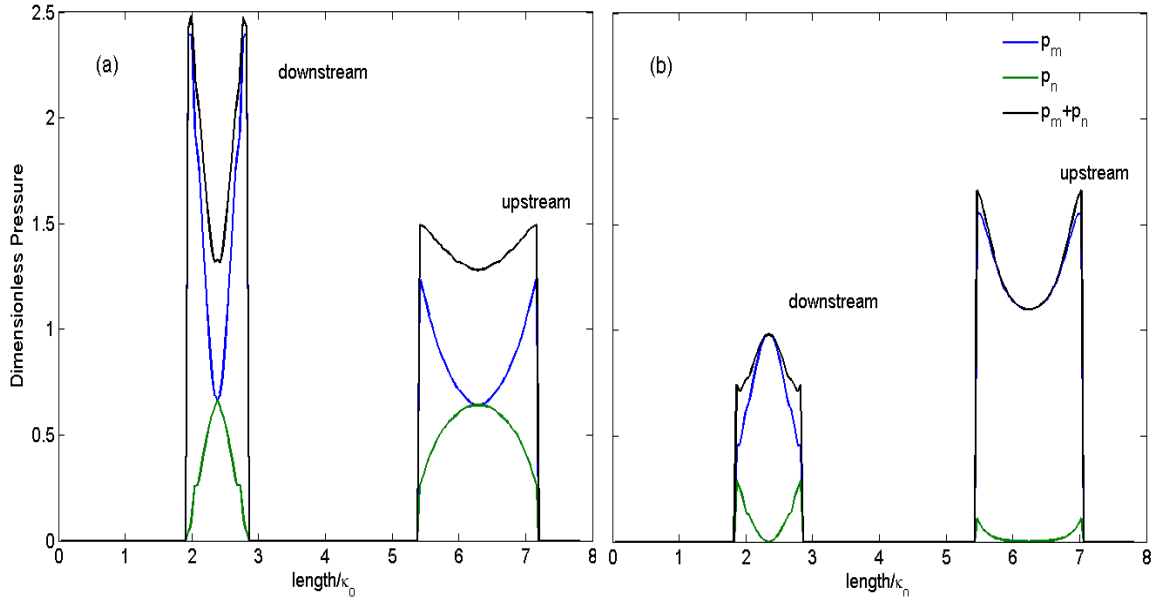

Figure 7.16— Magnetic pressure profile on the downstream and upstream interfaces (other interface segments are not shown). For the horizontal field (a), the magnetic pressures acting downstream are in average higher than the ones upstream. The inverse occurs for the vertical field (b) and thus the magnetic pressures contribute to the ganglion mobilization.

The magnetic pressure profiles on the upstream interface are not trivial because the external magnetic field intercepts the contact region at an intermediate angle (between the completely parallel and perpendicular configurations studied in the straight tube). Nonetheless, the average magnitude of the combined magnetic pressures obtained on this interface is similar in the two field orientations. Whereas this magnitude is far surpassed by the magnetic stresses on the downstream interface in the case of an applied horizontal

field, the inverse happens in the case of a vertical field. Therefore, the overall effect of applying a vertical magnetic field to this pore geometry contributes to the pressure gradient in mobilizing the ganglion.

Under a conservative choice of parameters a significant reduction in Ca_c was observed: from 0.13 to 0.09. This reduction should be interpreted in relative terms, because the typical absolute values of the capillary numbers defined with reference to Darcy velocity, as it is usual in porous media studies, are in a different order of magnitude.

Although the result was obtained for a very particular geometry, the fact that the mobilization mechanism seems to be controlled specifically by the magnitude of the magnetic pressures on the downstream interface in the imminence of being mobilized suggests that the conclusions might also apply to pores with complex three-dimensional network connections.

CHAPTER 8: Conclusions

Dispersions of magnetic nanoparticles in a liquid carrier, known as ferrofluids, have great potential for subsurface applications. Although extensive experimental and numerical research has been conducted in the mechanics of ferrofluids, the topic is never analyzed under the conditions that are likely to occur in the subsurface environments. In particular, very little attention is given to two-phase systems in which the ferrofluid is wetting.

The most relevant problems involving ferrofluids in porous media must be addressed at a pore-scale level before macroscopic continuum models can be developed. For instance, investigating the trapping and releasing of ganglia, such as residual oil in water-wet reservoirs, in the presence of a magnetized ferrofluid requires resorting to the pore models used for describing the mechanisms that control the ganglia dynamics. Once the effects of ferrofluids magnetization are properly incorporated into these mechanisms, generalizations based on pore scale parameters can be made to macroscopic volumes of porous media.

Modeling immiscible displacements involving a magnetized wetting ferrofluid at pore-scale level poses some interesting challenges. The magnetic stresses that drive the ferrofluid motion depend on the sharp magnetic field gradients formed near the regions where the liquid interface approaches the solid surface. The magnitude of these gradients is in turn influenced by the magnetic-stresses driven motion of the liquid interface. Hence, the coupling between the magnetic effects and the fluid dynamics aspects of the problem deserve special care.

This work presents an approach for modeling the ferrofluid displacement that captures the complexity of the underlying physics of the problem and yet provides a

mathematical formulation that is feasible for computational simulations. As a starting point, the model assumes that the liquid interface moves quasi-statically in all the situations of interest. This assumption leads to two separate problems: a magnetostatic problem involving a domain with regions of different magnetic permeability and a low-Reynolds-number flow problem in which the velocity at the interface is taken as negligible. The magnetic and flow field solutions are then coupled by an equation that governs that interface equilibrium under the combined effects of thermodynamic, magnetic and capillary pressures.

A level set method is employed for tracking the quasi-static motion of the liquid interface in a reliable and accurate way. This method is particularly suitable for handling interface displacements constrained by surfaces with arbitrary shapes, as it commonly occurs in pore spaces. Different versions of the immersed interface method are used for obtaining the magnetic field and the flow fields. The advantage of this method is using non-conforming grids for dealing with domains defined by irregular boundaries. Therefore, it provides a mathematically rigorous treatment of the solution in the vicinity of the boundaries while avoiding the need for remeshing as the liquid interface moves.

Solutions were obtained for three scenarios with distinct features. The first one involves a non-wetting ganglion touching adjacent solid surfaces in the absence of flow. It has a focus on the balance between capillary and magnetic pressures acting on the interface. The results indicate two different behaviors according to the orientation of the external magnetic field: the field perpendicular to the flow path causes the three-phase contact to move towards the wetting phase whereas, for the field parallel to the flow, the contact moves in the opposite direction and the ganglion detaches from the wall. An analysis of the magnetic field distribution shows that the different displacement patterns

are related to the kind of perturbation the field undergoes in near the three-phase contact zones.

In the second scenario, a droplet moves under steady-state conditions driven by a force uniformly applied on its volume inside a microchannel filled with ferrofluid. Naturally, the droplet equilibrium shape is influenced by the magnetic field in a similar way as in the previous problem. The fact that the droplet elongates towards the flow direction and distances itself from the walls under a field parallel to the flow path implies in a reduction of pressure gradients. Consequently, the magnitude of the driving force necessary for the droplet achieving a given velocity becomes smaller. This suggests that the ferrofluid magnetization can be used for improving the transport of a non-wetting liquid to some target location.

The third scenario evaluates the potential use of ferrofluids for EOR purposes. It consists in obtaining the equilibrium shape of the largest possible ganglion trapped inside a snap-off geometry in the imminence of being mobilized. The simulation results show that a magnetic field perpendicular to the flow path causes a significant reduction in the pressure drop necessary for achieving critical mobilization conditions. This magnetic field orientation favors mobilization for producing stronger magnetic stresses on the upstream interface of the ganglion than on the downstream one. Provided a sufficiently strong magnetic field can be generated, a synergy of ferrofluid magnetization and existing EOR techniques may help reducing residual oil saturations.

It must be emphasized that the results obtained have great significance in spite of the assumption of quasi-static interface displacement. As discussed in Section 2.22, for the limiting case in which a ganglion is subjected to a pressure gradient just enough to cause its mobilization, the interfaces are indeed expected to move quasi-statically. Hence, the quasi-static model is adequate for detecting critical mobilization conditions.

However, displacements in which the quasi-static assumption does not hold are also relevant to the study of ferrofluid-driven mobilization of ganglia. For instance, it is important to evaluate the potential benefit of applying an oscillating magnetic field instead of a permanent one. For dealing with this case, the model would need to account for the time-dependent terms in both the Maxwell and the Navier-Stokes equations.

Some other limitations of the current model must be addressed by future work. While the 2-D simulations capture the fundamental physics of the problem, some specific issues, such as the effect of wetting phase pendular rings to the ganglion, need adequate 3-D modeling. Another possible extension of the model is to account for nonlinear ferrofluid magnetization according to Langevin function. The immersed interface method can be extended to deal with magnetic permeability varying continuously in space, although in real applications the induction field most likely is insufficient to reach the ferrofluid saturation magnetization. Lastly, it is important to extend the level set method capabilities to handle non-zero contact angles (Jettestuen et al. 2013), as the regions where the oil blob touches the wall have key importance to the magnetic field distribution.

References

Adalsteinsson, D., and Sethian, J.. (1999). The Fast Construction of Extension Velocities in Level Set Methods. J. Comput. Phys. 148, 2–22.

Afkhami, S., Renardy, Y., Renardy, M., Riffle, J.S., and St PIERRE, T. (2008). Field-induced motion of ferrofluid droplets through immiscible viscous media. Journal of Fluid Mechanics 610, 363–380.

Bear, J. (1972). Dynamics of Fluids in Porous Media (Courier Corporation).

Berkovsky, B.M., Medvedev, V.F., and Krakov, M.S. (1993). Magnetic Fluids: Engineering Applications (Oxford ; New York: Oxford University Press).

Borglin, M., and Oldenburg, C. (1998). On magnetic fluid emplacement: Laboratory Experiments of Ferrofluid Flow. Water Resources Research.

Borhan, A., and Pallinti, J. (1995). Buoyancy-Driven Motion of Viscous Drops through Cylindrical Capillaries at Small Reynolds Numbers. Industrial & Engineering Chemistry Research 34.

Charles, S.W. (2002). The Preparation of Magnetic Fluids. In Ferrofluids, S. Odenbach, ed. (Springer Berlin Heidelberg), pp. 3–18.

Chatzis, I., Morrow, N.R., and Lim, H.T. (1983). Magnitude and Detailed Structure of Residual Oil Saturation. Society of Petroleum Engineers Journal 23, 311–326.

Chéné, A. du, Min, C., and Gibou, F. (2007). Second-Order Accurate Computation of Curvatures in a Level Set Framework Using Novel High-Order Reinitialization Schemes. J Sci Comput 35, 114–131.

Davidson, A., Huh, C., and Bryant, S.L. (2012). Focused Magnetic Heating Utilizing Superparamagnetic Nanoparticles for Improved Oil Production Applications. (Society of Petroleum Engineers),.

Fatt, I. (1956). The network model of porous media I. Capillary pressure characteristics. Petroleum Transactions, AIME 207, 144–159.

Jettestuen, E., Helland, J.O., and Prodanović, M. (2013). A level set method for simulating capillary-controlled displacements at the pore scale with nonzero contact angles. Water Resour. Res. 49, 4645–4661.

Ko, S., Mogensen, K., Bennetzen, M.V., Prigiobbe, V., Bryant, S.L., and Huh, C. (2014). Accelerated Oil Droplet Separation from Produced Water Using Magnetic Nanoparticles. (Society of Petroleum Engineers),.

Lake, L. (1996). Enhanced Oil Recovery (Englewood Cliffs, N.J: Prentice Hall).

Lavrova, O., Matthies, G., Polevikov, V., and Tobiska, L. (2004). Numerical modeling of the equilibrium shapes of a ferrofluid drop in an external magnetic field. Proc. Appl. Math. Mech. 4, 704–705.

Lavrova, O., Matthies, G., Mitkova, T., Polevikov, V., and Tobiska, L. (2006). Numerical treatment of free surface problems in ferrohydrodynamics. Journal of Physics Condensed Matter 18, 2657–2669.

Lenormand, R., Zarcone, C., and Sarr, A. (1983). Mechanisms of the displacement of one fluid by another in a network of capillary ducts. Journal of Fluid Mechanics 135, 337–353.

LeVeque, R.J., and Li, Z. (1994). The Immersed Interface Method for Elliptic Equations with Discontinuous Coefficients and Singular Sources. SIAM Journal on Numerical Analysis 31, 1019–1044.

LeVeque, R.J., and Li, Z. (1997). Immersed Interface Methods for Stokes Flow with Elastic Boundaries or Surface Tension. SIAM Journal on Scientific Computing 18, 709–735.

Li, Z., and Ito, K. (2006). The Immersed Interface Method: Numerical Solutions of PDEs Involving Interfaces and Irregular Domains (Philadelphia: Society for Industrial and Applied Mathematics).

Liu, M., and Stierstadt, K. (2009). Thermodynamics, Electrodynamics, and Ferrofluid Dynamics. In Colloidal Magnetic Fluids, S. Odenbach, ed. (Berlin, Heidelberg: Springer Berlin Heidelberg), pp. 1–74.

Melrose, J.C. (1974). Role of Capillary Forces In Detennining Microscopic Displacement Efficiency For Oil Recovery By Waterflooding. Journal of Canadian Petroleum Technology 13.

Mitchell, I.M., and Templeton, J.A. (2005). A Toolbox of Hamilton-Jacobi Solvers for Analysis of Nondeterministic Continuous and Hybrid Systems. In Hybrid Systems: Computation and Control, M. Morari, and L. Thiele, eds. (Springer Berlin Heidelberg), pp. 480–494.

Moridis, G.J., Borglin, S.E., Oldenburg, C.M., and Becker, A. (1998). Theoretical and Experimental Investigations of Ferrofluids for Guiding and Detecting Liquids in the Subsurface (Annual report, Berkeley, California, USA: Lawrence Berkeley National Laboratory).

Morrow, N.R. (1976). Capillary Pressure Correlations For Uniformly Wetted Porous Media. Journal of Canadian Petroleum Technology - J CAN PETROL TECHNOL 15.

Ng, K. M. and A.C.Payatakes (1980). Stochastic simulation of the motion, breakup and stranding of oil ganglia in water- wet granular porous media during immiscible displacement. AIChE Journal 26, 419–429.

Nguyen, T., Pollert, E., and Zaveta, K. (2012). Magnetic Nanoparticles: From Fabrication to Clinical Applications.

Ochonski, W. (2005). The attraction of ferrofluid bearings. Mach. Des. 77, 96–102.

Odenbach, S. (2002). Magnetoviscous Effects in Ferrofluids (Berlin, Heidelberg: Springer Berlin Heidelberg).

Oh, J., Feldman, M.D., Kim, J., Condit, C., Emelianov, S., and Milner, T.E. (2006). Detection of magnetic nanoparticles in tissue using magneto-motive ultrasound. Nanotechnology 17, 4183.

Oldenburg, C.M., Borglin, S.E., and Moridis, G.J. (2000). Numerical Simulation of Ferrofluid Flow for Subsurface Environmental Engineering Applications. Transport in Porous Media 38, 319–344.

Osher, S., and Fedkiw, R. (2003). Level Set Methods and Dynamic Implicit Surfaces (New York, NY: Springer New York).

Osher, S., and Sethian, J.A. (1988). Fronts propagating with curvature-dependent speed: Algorithms based on Hamilton-Jacobi formulations. Journal of Computational Physics 79, 12–49.

Pankhurst, Q.A., Thanh, N.T.K., Jones, S.K., and Dobson, J. (2009). Progress in applications of magnetic nanoparticles in biomedicine. Journal of Physics D: Applied Physics 42, 224001.

Papell Solomon, S. (1965). Low viscosity magnetic fluid obtained by the colloidal suspension of magnetic particles.

Payatakes, A.C. (1982). Dynamics of Oil Ganglia During Immiscible Displacement in Water-Wet Porous Media. Annual Review of Fluid Mechanics 14, 365–393.

Peng, D., Merriman, B., Osher, S., Zhao, H., and Kang, M. (1999). A PDE-Based Fast Local Level Set Method. Journal of Computational Physics 155, 410–438.

Prodanović, M., and Bryant, S.L. (2006). A level set method for determining critical curvatures for drainage and imbibition. Journal of Colloid and Interface Science 304, 442–458.

Rahmani, A.R., Prodanović, M., Bryant, S.L., and Huh, C. (2012). Quasi-static analysis of a ferrofluid blob in a capillary tube. Journal of Applied Physics 111, 074901.

Rodriguez Pin, E., Roberts, M., Yu, H., Huh, C., and Bryant, S.L. (2009). Enhanced Migration of Surface-Treated Nanoparticles in Sedimentary Rocks. (Society of Petroleum Engineers).

Roof, J.G. (1970). Snap-Off of Oil Droplets in Water-Wet Pores. Society of Petroleum Engineers Journal 10, 85–90.

Rosensweig, R.E. (1997). Ferrohydrodynamics (Courier Corporation).

Rosensweig, R.E., Nestor, J.W., and Timmins, R.S. (1965). Ferrohydrodynamic fluids for direct conversion of heat energy.

Russo, G., and Smereka, P. (2000). A Remark on Computing Distance Functions. Journal of Computational Physics 163, 51–67.

Ryoo, S., Rahmani, A.R., Yoon, K.Y., Prodanović, M., Kotsmar, C., Milner, T.E., Johnston, K.P., Bryant, S.L., and Huh, C. (2012). Theoretical and experimental investigation of the motion of multiphase fluids containing paramagnetic nanoparticles in porous media. Journal of Petroleum Science and Engineering 81, 129–144.

Sahimi, M. (2011). Flow and Transport in Porous Media and Fractured Rock: From Classical Methods to Modern Approaches (Weinheim, Germany: Wiley-VCH Verlag GmbH & Co. KGaA).

Sethian, J.A. (1999). Level Set Methods and Fast Marching Methods: Evolving Interfaces in Computational Geometry, Fluid Mechanics, Computer Vision, and Materials Science (Cambridge University Press).

Shah, D.O. (2012). Improved Oil Recovery by Surfactant and Polymer Flooding (Elsevier).

Soares, F.S.-M. de A., Prodanovic, M., and Huh, C. (2014). Excitable Nanoparticles for Trapped Oil Mobilization. In SPE Improved Oil Recovery Conference Proceedings, (Society of Petroleum Engineers),.

Stegemeier, G.L. (1974). Relationship of Trapped Oil Saturation to Petrophysical Properties of Porous Media. (Society of Petroleum Engineers),.

Stegemeier, G.L. (1977). MECHANISMS OF ENTRAPMENT AND MOBILIZATION OF OIL IN POROUS MEDIA. In Improved Oil Recovery by Surfactant and Polymer Flooding, D.O.S.S. SCHECHTER, ed. (Academic Press), pp. 55–91.

Stokes, J.P., Higgins, M.J., Kushnick, A.P., Bhattacharya, S., and Robbins, M.O. (1990). Harmonic generation as a probe of dissipation at a moving contact line. Phys. Rev. Lett. 65, 1885–1888.

Sussman, M., Smereka, P., and Osher, S. (1994). A Level Set Approach for Computing Solutions to Incompressible Two-Phase Flow. Journal of Computational Physics 114, 146–159.

Swarztrauber, P.N. (1977). The Method of cyclic reduction, Fourier analysis and the FACR algorithm for the discrete solution of Poisson's equation on a rectangle. SIAM Rev. 19, 490–501.

Tarapov, I.E. (1974). Flow of magnetizable fluid through long pipes. Soviet Applied Mechanics 10, 1240–1244.

Torres-Díaz, I., and Rinaldi, C. (2014). Recent progress in ferrofluids research: novel applications of magnetically controllable and tunable fluids. Soft Matter 10, 8584–8602.

Whitmer, R.M. (1962). Electromagnetics (Prentice Hall).

Wiegmann, A., and Bube, K.P. (2000). The Explicit-Jump Immersed Interface Method: Finite Difference Methods for PDEs with Piecewise Smooth Solutions. SIAM Journal on Numerical Analysis 37, 827–862.

Yu, H., Kotsmar, C., Yoon, K.Y., Ingram, D.R., Johnston, K.P., Bryant, S.L., and Huh, C. (2010). Transport and Retention of Aqueous Dispersions of Paramagnetic Nanoparticles in Reservoir Rocks. (Society of Petroleum Engineers),.

Zhijun Tan, K.M.L. (2009). A fast immersed interface method for solving Stokes flows on irregular domains. Computers & Fluids 1973–1983.

Zhu, G.-P., Nguyen, N.-T., Ramanujan, R.V., and Huang, X.-Y. (2011). Nonlinear Deformation of a Ferrofluid Droplet in a Uniform Magnetic Field. Langmuir 27, 14834–14841.